

**MODELING AND VALIDATION OF A SYNTACTIC FOAM  
LINING FOR NOISE CONTROL DEVICES FOR FLUID POWER  
SYSTEMS**

A Dissertation  
Presented to  
The Academic Faculty

by

Nicholas Edmond Earnhart

In Partial Fulfillment  
Of the Requirements for the Degree  
Doctor of Philosophy in Mechanical Engineering

Georgia Institute of Technology

December 2012

Copyright 2012 by Nicholas E. Earnhart

**MODELING AND VALIDATION OF A SYNTACTIC FOAM  
LINING FOR NOISE CONTROL DEVICES FOR FLUID POWER  
SYSTEMS**

Approved by:

Dr. Kenneth A. Cunefare, Advisor  
School of Mechanical Engineering  
*Georgia Institute of Technology*

Dr. Haskell Beckham  
School of Materials Science and  
Engineering  
*Georgia Institute of Technology*

Dr. Wayne J. Book  
School of Mechanical Engineering  
*Georgia Institute of Technology*

Dr. Kim Stelson  
School of Mechanical Engineering  
*University of Minnesota*

Dr. Mardi C. Hastings  
School of Mechanical Engineering  
*Georgia Institute of Technology*

Date Approved: November 9, 2012

To my wife, Maria.

## ACKNOWLEDGEMENTS

I wish to first thank my wife, Maria, for her enduring love and support of my academic pursuits. I must also thank my parents, Edgar and Marjory Earnhart, for their faultless upbringing and support of my education in all phases, and my in-laws, Antonino and Pietra Allegra. In particular, I thank my father for my love of machinery and my mother for my vocabulary. I need to especially thank my advisor, Dr. Ken Cunefare, for his influence, expectations, criticism, teaching, and insight, and for my development as an academic, researcher, and engineer. I must thank my dissertation reading committee, especially Dr. Book for letting me use his laboratory for my experiments. Innumerable thanks go to Dr. Ben Beck, my officemate for the past five years, for having all the answers when my brain fails to function properly, and for generally keeping me sane, especially during late night study sessions and client testing work that seemed to carry on forever. I wish to express my appreciation for my colleagues for their help and influence, including but not limited to Dr. Robert Amaro, Jamie Wilson, Man Prakash Gupta, Elliott Gruber, and Ellen Skow. This work would have been far more difficult without J.D. Huggins, whose assistance cannot be understated. I am especially grateful to the Josh Hernandez at Goodrich Corp. for casting each of the urethane liners used in this work, and to all my fellow students and undergraduates who contributed in meaningful ways.

I must also thank the Center for Compact and Efficient Fluid Power, a National Science Foundation Engineering Research Center, for financial support. Additional personal support was granted by the Georgia Institute of Technology President's Fellowship and the Achievement Rewards for College Scientists (ARCS) Foundation.

# TABLE OF CONTENTS

|                                      |     |
|--------------------------------------|-----|
| Acknowledgements.....                | iv  |
| List of Tables .....                 | x   |
| List of Figures .....                | xi  |
| Nomenclature .....                   | xvi |
| Summary .....                        | iv  |
| Chapter 1 Introduction .....         | 1   |
| 1.1    Research Motivation.....      | 1   |
| 1.2    Research Objectives .....     | 3   |
| 1.3    Research Approach.....        | 3   |
| 1.4    Overview of Dissertation..... | 4   |
| Chapter 2 Literature Review .....    | 6   |
| 2.1    Helmholtz Resonator .....     | 6   |
| 2.2    Tuning Coil.....              | 10  |
| 2.3    Herschel-Quincke Tube.....    | 13  |
| 2.4    Research Opportunity.....     | 15  |
| Chapter 3 Syntactic Foam.....        | 16  |
| Chapter 4 Compliance.....            | 21  |
| 4.1    General equations .....       | 21  |
| 4.1.1    Dimensions.....             | 22  |
| 4.2    Hydrostatic deformation.....  | 23  |
| 4.3    Cavity Compliance .....       | 24  |

|           |  |    |
|-----------|--|----|
| 4.3.1     | Empty cavity .....                                 | 25 |
| 4.3.2     | Solid cylinder .....                               | 27 |
| 4.3.3     | Annular cylinder.....                              | 28 |
| 4.4       | Waveguide compliance .....                         | 29 |
| 4.4.1     | Solid/Annular Cylinder .....                       | 29 |
| 4.4.2     | Internal pressure and a fixed outer boundary ..... | 30 |
| 4.4.3     | External pressure and a fixed inner boundary ..... | 31 |
| 4.4.4     | Comparison .....                                   | 31 |
| 4.5       | Sources of Compliance.....                         | 36 |
| 4.5.1     | Fluid .....  | 37 |
| 4.5.2     | Entrained air .....                                | 39 |
| 4.5.3     | Structural compliance.....                         | 41 |
| 4.5.4     | Net effect.....                                    | 42 |
| Chapter 5 | Experiment .....                                   | 44 |
| 5.1       | Liner Materials .....                              | 44 |
| 5.2       | Devices .....                                      | 48 |
| 5.2.1     | Helmholtz Resonator.....                           | 48 |
| 5.2.2     | Tuning Coil .....                                  | 50 |
| 5.3       | Liner Deformation .....                            | 51 |
| 5.4       | Measurement and analysis of transmission loss..... | 54 |
| 5.5       | Test Rig .....                                     | 59 |
| 5.5.1     | Calibration.....                                   | 60 |
| 5.5.2     | Coherence.....                                     | 61 |

|   |     |
|---|-----|
| Chapter 6 Helmholtz Resonator .....                   | 64  |
| 6.1 Modeling .....                                    | 64  |
| 6.2 Parameter Study .....                             | 72  |
| 6.3 Discussion of Experiment .....                    | 75  |
| 6.3.1 Method .....                                    | 75  |
| 6.3.2 Entrained Air .....                             | 76  |
| 6.3.3 Model Fit .....                                 | 78  |
| 6.4 Experimental Results.....                         | 79  |
| 6.4.1 General Behavior.....                           | 79  |
| 6.4.2 Stiffness Comparison .....                      | 82  |
| 6.4.3 Voided vs. Neat .....                           | 84  |
| 6.4.4 Pressure Effects .....                          | 85  |
| 6.4.5 Second-Generation Syntactic Foam .....          | 88  |
| 6.4.6 Tan Delta and Quality Factor .....              | 90  |
| 6.4.7 Speed of Sound.....                             | 94  |
| Chapter 7 Tuning Coil and Herschel-Quincke Tube ..... | 96  |
| 7.1 Modeling – Tuning Coil .....                      | 96  |
| 7.1.1 Parameter Study .....                           | 101 |
| 7.2 Modeling – Herschel-Quincke Tube .....            | 106 |
| 7.2.1 Parameter Study .....                           | 108 |
| 7.3 Experimental Results.....                         | 111 |
| 7.3.1 Comparison to Model.....                        | 112 |
| 7.3.2 Resonator Model .....                           | 117 |

|   |                                       |     |
|---|---------------------------------------|-----|
| 7.4   | Comparison to Commercial Devices..... | 119 |
| Chapter 8 Conclusions and Future Work.....  |                                       | 124 |
| 8.1   | Conclusions .....                     | 124 |
| 8.2   | Recommendations for Future Work.....  | 127 |
| 8.2.1                                       | Material properties .....             | 127 |
| 8.2.2                                       | Manufacturing and Development.....    | 128 |
| 8.2.3                                       | Mechanical properties .....           | 129 |
| 8.2.4                                       | Smart/Active Materials .....          | 129 |
| Appendix A Liner Deformation Equations..... |                                       | 130 |
| A.1   | Liner Deformation.....                | 130 |
| Appendix B Computer Code.....               |                                       | 133 |
| B.1   | Speed of Sound.....                   | 133 |
| B.2   | Transmission Loss .....               | 135 |
| B.3   | Calibration .....                     | 144 |
| B.4   | Helmholtz Resonator.....              | 146 |
| B.4.1                                       | Modeling Function .....               | 146 |
| B.4.2                                       | Least-Squares Code.....               | 149 |
| B.5   | Tuning coil .....                     | 152 |
| B.5.1                                       | Modeling Function .....               | 152 |
| B.5.2                                       | Modulus Interpolation.....            | 156 |
| B.6   | Herschel-Quincke Tube.....            | 157 |
| B.6.1                                       | Modeling Code.....                    | 157 |
| References.....                             |                                       | 161 |

Vita.....166

## LIST OF TABLES

|   |     |
|---|-----|
| Table 1: List of dimensions and their description.....  | 23  |
| Table 2: Dimensions of two construction cases for an elastic waveguide liner. ....                | 33  |
| Table 3: Liner properties.....  | 45  |
| Table 4: Liner dimensions. ....   | 45  |
| Table 5: Microsphere properties. ....   | 46  |
| Table 6: Helmholtz resonator dimensions. ....   | 49  |
| Table 7: Tuning coil dimensions.....  | 51  |
| Table 8: Inner radius of each liner as a function of pressure (in mm). ....                       | 53  |
| Table 9: Dimensions of theoretical Helmholtz resonator. ....                                      | 75  |
| Table 10: Bulk modulus of GR9-625 at 22.8 C for assumed fractions of entrained air. ..            | 77  |
| Table 11: Liner GR23 461-663 calculated bulk modulus and tan delta values at three pressures..... | 79  |
| Table 12: Properties of a tuning coil using liner GR23 461-633 at 23.3 C. ....                    | 102 |

## LIST OF FIGURES

|  |    |
|--|----|
| Figure 2-1: Schematic of a Helmholtz resonator. ....   | 7  |
| Figure 2-2: ¼-wave resonator configurations: a) T-branch b) Concentric. ....   | 11 |
| Figure 2-3: Hose tuner. ....   | 12 |
| Figure 2-4: Kojima and Ichiyanagi’s “variable resonance-mode type side-branch resonator.” .....  | 12 |
| Figure 2-5: A schematic of the bladder-style tuning coil from a patent assigned to Knapp [30]......  | 13 |
| Figure 2-6: Herschel-Quincke tube configuration: a) Traditional b) Concentric. ....  | 14 |
| Figure 3-1: a) Bulk modulus and b) tangent delta for a urethane-host syntactic foam at: — 20 C, — 35 C, — 45 C.....  | 19 |
| Figure 3-2: a) Expancel microspheres at atmospheric pressure and b) post-buckling [49].<br>.....   | 19 |
| Figure 4-1: Schematic of device cross-section with labeled components and radii. ....  | 23 |
| Figure 4-2: Non-dimensional compliance of an empty shell with internal hydrostatic pressure as a function of the ratio of the wall thickness to mean radius... 27          | 27 |
| Figure 4-3: Schematic of a tuning coil with a waveguide formed between the liner and annulus. ....   | 30 |
| Figure 4-4: Schematic of a tuning coil with a waveguide formed between the liner and shell. ....   | 31 |
| Figure 4-5: Ratio of waveguide stiffness where the waveguide is between the liner and shell. ....  | 34 |
| Figure 4-6: Ratio of waveguide stiffness for two cases: a waveguide formed between an unconstrained liner and a rigid shell, and between a rigid annulus and a liner. .... | 35 |
| Figure 4-7: Ratio of waveguide stiffness formed at the outer or inner boundary of a compliant liner in a rigid shell. ....   | 36 |
| Figure 4-8: Isothermal tangent bulk modulus of hydraulic oil at temperatures from 20 C to 100 C.....   | 39 |
| Figure 4-9: Bulk modulus of hydraulic oil at 20 C with volumetric fractions of entrained air from 0.0% to 10%.....   | 41 |

|  |    |
|--|----|
| Figure 4-10: Stiffness of hydraulic oil-filled cylindrical cavity: — — shell — — fluid — — total system. ....  | 43 |
| Figure 5-1: Bulk modulus of liners at 35 C and atmospheric pressure, — HRP15(12)-545, — GR23-633, — GR9-625.....   | 47 |
| Figure 5-2: Tan delta of liners at 35 C and atmospheric pressure, — HRP15(12)-545, — GR23-633, — GR9-625.....  | 48 |
| Figure 5-3: Schematic of Helmholtz resonator with dimensions.....  | 49 |
| Figure 5-4: Photograph of the Helmholtz resonator prototype with the end cap removed. ....   | 49 |
| Figure 5-5: Schematic of tuning coil with dimensions .....   | 50 |
| Figure 5-6: Photograph of tuning coil prototype with one end cap removed and the liner and annulus partially extracted. ....   | 51 |
| Figure 5-7: Test fixture for measuring liner compression. ....   | 53 |
| Figure 5-8: Inner radius of liner as a function of static pressure for three liners: ◆ GR23 (unvoided), ■ GR23-633 (voided), ▲ GR23 461-663 (voided).....  | 54 |
| Figure 5-9: Schematic of a noise control device under test. ....   | 55 |
| Figure 5-10: Schematic of the hydraulic test rig.....  | 60 |
| Figure 5-11: Picture of calibration block with three sensors installed.....  | 61 |
| Figure 6-1: Helmholtz resonator with compliant lining. ....  | 65 |
| Figure 6-2a): Transmission line analogy with Helmholtz resonator and load impedance b) Circuit analogy of Helmholtz resonator.....   | 65 |
| Figure 6-3: Theoretical model for Helmholtz resonator with a neck 37.34 mm long and a radius of 2.97 mm, with a cavity volume of 0.31 L: — No liner, — Liner with $K' = 656$ MPa, — Liner with $K' = 53.8$ MPa. .... | 74 |
| Figure 6-4: Theoretical model for lined Helmholtz resonator with a neck 37.34 mm long and a radius of 2.97 mm, with a cavity volume of 0.31 L: — Liner tan $\delta$ 0.0, — 0.2, — 0.4, — 0.6.....                    | 74 |
| Figure 6-5: Bulk modulus of GR9-625 assuming fraction of entrained air: ◆ 0%, ■ 0.1%, ▲ 1.0%, and × 10%.....   | 77 |
| Figure 6-6 Fit of experiment to model for GR9-625 at 2.1 MPa and 22.8 C assuming a) 1.0% entrained air b) 10% entrained air: ◆ Experiment — Model. ....  | 78 |

|   |    |
|---|----|
| Figure 6-7: Measured transmission loss of liner GR23 461-663, model: — 2.1 MPa, — 6.9 MPa, — 21 MPa; experiment: ◆ 2.1 MPa, ■ 6.9 MPa, ▲ 21 MPa. ....                     | 79 |
| Figure 6-8: Bulk modulus of liner GR23-633 at ◆ 23 C, ■ 26 C, and ▲ 33 C. ....  | 80 |
| Figure 6-9: Bulk modulus of liner GR23 at ◆ 23 C, ■ 26 C, and ▲ 33 C. ....  | 81 |
| Figure 6-10: Bulk modulus of liner HRP15(12) at ◆ 23 C, ■ 25 C, and ▲ 32 C. ....  | 82 |
| Figure 6-11: Bulk modulus of liner GR9 at ◆ 23 C, ■ 25 C, and ▲ 32 C. ....  | 82 |
| Figure 6-12: Constituent stiffness terms for a Helmholtz resonator with liner GR9-625 at 2.1 MPa and 22.8 C: ▲ shell, ◆ fluid, ■ liner, ● total. ....                     | 83 |
| Figure 6-13: Constituent stiffness terms for a Helmholtz resonator with liner GR9 at 2.1 MPa and 20.0 C: ▲ shell, ◆ fluid, ■ liner, ● total. ....                         | 84 |
| Figure 6-14: Bulk modulus of ◆ GR23, neat urethane, at 26 C, ■ GR23-633, syntactic foam, at 29 C. ....  | 85 |
| Figure 6-15: Bulk modulus of GR9-625 at ◆ 29.2 C, ■ 37.7 C, ▲ 47.1 C. ....  | 86 |
| Figure 6-16: Bulk modulus of GR23-633 at ◆ 29.2 C, ■ 37.7 C, ▲ 47.1 C. ....   | 87 |
| Figure 6-17: Bulk modulus of HRP15(12)-545 at ◆ 29.2 C, ▲ 47.1 C. ....  | 87 |
| Figure 6-18: Bulk modulus of GR23 461-663, ◆ 24.3 C, ■ 27.7 C, ▲ 32.6 C. ....   | 89 |
| Figure 6-19: Bulk modulus at 23 C, ◆ GR23-633, ■ GR23 461-663. ....   | 90 |
| Figure 6-20: Bulk modulus at 33 C, ◆ GR23-633, ■ GR23 461-663. ....   | 90 |
| Figure 6-21: Tan delta of liners at 32 C, ◆ GR23-633, ■ GR23-633, ▲ GR9-625. ....   | 91 |
| Figure 6-22: The tan $\delta$ of liner HRP15(12) at ◆ 22.9 C, ■ 32.6 C, and of liner HRP15(12)-545 at ◆ 24.1 C, □ 32.7 C. ....  | 92 |
| Figure 6-23: The tan $\delta$ of liner GR23-633 at ◆ 23.3 C, ■ 25.8 C, ▲ 33.0 C. ....   | 93 |
| Figure 6-24: Tan Delta and Quality Factor at 23 C for ■ GR23 ▲ GR23-633. ....   | 94 |
| Figure 6-25: The bulk modulus and effective speed of sound in the Helmholtz resonator with liner GR9-625 at 22.8 C: ■ bulk modulus, ◆ effective speed of sound. ....      | 95 |
| Figure 6-26: The bulk modulus and effective speed of sound in the Helmholtz resonator with liner GR23 461-663 at 32.6 C: ■ bulk modulus, ◆ effective speed of sound. .... | 95 |

|   |     |
|---|-----|
| Figure 7-1: Port numbering of tuning coil. ....   | 97  |
| Figure 7-2: Predicted transmission loss of a tuning coil with GR23 461-633 at 23.3 C at<br>— 2.1 MPa, — 6.9 MPa, and — 20.7 MPa. ....   | 103 |
| Figure 7-3: Predicted transmission loss of a tuning coil with GR23 461-633 at 23.3 C at<br>6.9 MPa, a $\tan \delta$ of zero, a fixed inner radius of the shell, and an annular<br>gap width of — 0.5 mm, — 1 mm, and — 2 mm. .... | 105 |
| Figure 7-4: Predicted transmission loss of a tuning coil with GR23 461-633 at 23.3 C at<br>6.9 MPa, a gap width of 1 mm, and a $\tan \delta$ of — 0.0, — 0.2, and — 0.4.<br>.....   | 106 |
| Figure 7-5: Schematic of a Herschel-Quincke tube with a compliant liner.....  | 107 |
| Figure 7-6: Predicted transmission loss of a Herschel-Quincke tube with a GR23 461-663<br>liner at pressures of — 2.1 MPa, — 3.4 MPa, — 5.5 MPa, — 6.9 MPa,<br>and — 21 MPa. ....   | 110 |
| Figure 7-7: Predicted transmission loss of a Herschel-Quincke tube with a GR23 461-663<br>liner at gap thickness of — 1 mm, — 1.5 mm, — 2 mm, and — 3 mm. ....  | 110 |
| Figure 7-8: Predicted transmission loss of a Herschel-Quincke tube with a GR23 461-663<br>liner at $\tan \delta$ of — 0.0, — 0.1, — 0.2, and — 0.4. ....  | 111 |
| Figure 7-9: Measured transmission loss of tuning coil with GR9-625 at 2.1 MPa and 22.5<br>C, — model, ● experiment, ○ frequencies of possible artifacts. ....   | 114 |
| Figure 7-10: Plot of the phase condition, Equation (6.31), where points near 0 may<br>indicate frequencies of artifacts in experimental data.....   | 114 |
| Figure 7-11: Measured transmission loss of tuning coil with GR9-625 at 4.8 MPa and<br>22.8 C, — model, ● experiment, ○ frequencies of possible artifacts. ....  | 115 |
| Figure 7-12: Measured transmission loss of tuning coil with GR9-625 at 6.9 MPa and<br>23.1 C, — model, ● experiment, ○ frequencies of possible artifacts. ....  | 115 |
| Figure 7-13: Measured transmission loss of tuning coil with GR9-625 at 4.8 MPa and<br>23.1 C with a modified waveguide compliance, — model, ● experiment, ○<br>frequencies of possible artifacts.....                             | 116 |
| Figure 7-14: Measured transmission loss of tuning coil with GR9-625 at 2.1 MPa and<br>22.5 C, — Helmholtz resonator model, ● experiment, ○ frequencies of<br>possible artifacts.....  | 118 |
| Figure 7-15: Measured transmission loss of tuning coil with GR9-625 at 4.8 MPa and<br>22.8 C, — Helmholtz resonator model, ● experiment, ○ frequencies of<br>possible artifacts.....  | 118 |

|  |     |
|--|-----|
| Figure 7-16: Measured transmission loss of tuning coil with GR9-625 at 6.9 MPa and 23.1 C, — Helmholtz resonator model, ● experiment, ○ frequencies of possible artifacts..... | 119 |
| Figure 7-17: Schematic of modified test rig using a piezoelectric stack to excite the system. ....   | 121 |
| Figure 7-18: Measured transmission loss of hydraulic hose at ◆ 1.4 MPa, ■ 2.1 MPa, and ▲ 3.4 MPa, ○ frequencies of possible artifacts.....                                     | 122 |
| Figure 7-19: Measured transmission loss of commercially-available tuning coil at ◆ 1.4 MPa, ■ 2.1 MPa, and ▲ 3.4 MPa, ○ frequencies of possible artifacts...                   | 123 |
| Figure 7-20: Measured transmission loss at 3.4 MPa of ◆ tuning coil, ■ hydraulic hose, ● prototype tuning coil. ....   | 123 |
| Figure 8-1: Differential element in the cross-section of a thick shell.....  | 131 |

## NOMENCLATURE

|              |   |               |                              |
|--------------|---|---------------|------------------------------|
| $a$          | Constant                                      | $L$           | Inertance                    |
| $A$          | Constant                                      | $L$           | Length                       |
| $A, B, D, E$ | Wave amplitudes                               | $m$           | Mass                         |
| $b$          | Constant                                      | $m$           | Ratio of radii               |
| $b$          | Vector of transfer functions                  | $n$           | Polytropic constant          |
| $c$          | Speed of sound                                | $p$           | Static pressure              |
| $C$          | Compliance                                    | $P$           | Acoustic pressure            |
| $C$          | Constant                                      | $Q$           | Acoustic velocity            |
| $C_{xy}$     | Coherence                                     | $QF$          | Quality factor               |
| $E$          | Young's modulus                               | $r$           | Radius                       |
| $f$          | Frequency                                     | $R$           | Resistance                   |
| $G$          | Matrix  | $s$           | Laplacian                    |
| $G_{xy}$     | Cross-spectral density                        | $s$           | Stiffness                    |
| $G_{xx}$     | Autospectral density                          | $S$           | Cross-sectional area         |
| $H_{ij}$     | Transfer function                             | $t$           | Thickness                    |
| $I$          | Current                                       | $t_{ij}$      | Transfer matrix element      |
| $j$          | $\sqrt{-1}$                                   | $\tan \delta$ | Viscoelastic loss factor     |
| $J$          | Bessel's function of the 1 <sup>st</sup> kind | $\mathbf{T}$  | Transfer matrix              |
| $k$          | Wavenumber                                    | $T$           | Temperature                  |
| $K^*$        | Complex bulk modulus                          | $T_g$         | Glass transition temperature |
| $K'$         | Bulk storage modulus                          | $TL$          | Transmission loss            |
| $K''$        | Bulk loss modulus                             | $u$           | Displacement                 |

|            |   |                    |                          |
|------------|---|--------------------|--------------------------|
| $V$        | Voltage                                 | $\omega$           | Angular frequency        |
| $V$        | Volume                                  | <b>Subscripts:</b> |                          |
| $W$        | Acoustic power                          | 0                  | Atmospheric conditions   |
| $x$        | Position                                | 0                  | Acoustic                 |
| $X$        | Fraction of air                         | $a$                | Air                      |
| $X$        | Vector of pressures                     | $a$                | Annulus                  |
| $y$        | Position                                | $A$                | Adiabatic                |
| $Y$        | Bessel's Function, 2 <sup>nd</sup> kind | $b$                | Branch                   |
| $z$        | Axial position                          | $c$                | Cavity                   |
| $Z$        | Impedance                               | $c$                | Characteristic impedance |
| $\alpha_w$ | Loss factor                             | $cr$               | Critical                 |
| $\beta$    | Bulk stiffness                          | $d$                | Downstream               |
| $\gamma$   | Complex wavenumber                      | $e$                | Effective                |
| $\Gamma$   | Wavenumber                              | $f$                | Fluid                    |
| $\lambda$  | Wavelength                              | $free$             | Unconstrained            |
| $\nu$      | Poisson's ratio                         | $g$                | Gas                      |
| $\xi$      | Viscous loss factor                     | $H$                | Helmholtz resonator      |
| $\phi$     | Particle concentration                  | $i$                | Incident                 |
| $\phi$     | Phase                                   | $inner$            | Inward orientation       |
| $\rho$     | Density                                 | $l$                | Liquid                   |
| $\sigma$   | Stress                                  | $L$                | Liner                    |
| $\nu$      | Kinematic viscosity                     | $n$                | Resonator neck           |
| $\chi$     | Ratio                                   | $o$                | Oil                      |

|              |                       |
|--------------|-----------------------|
| <i>outer</i> | Outward orientation   |
| <i>p</i>     | Pipe                  |
| <i>P</i>     | Pressure              |
| <i>r</i>     | Radial direction      |
| <i>r</i>     | Resistance            |
| <i>r</i>     | Resonance             |
| <i>S</i>     | Shell                 |
| <i>t</i>     | Termination           |
| <i>t</i>     | Transmitted           |
| <i>t</i>     | Transverse direction  |
| <i>tr</i>    | Throat of tuning coil |
| <i>T</i>     | Isothermal            |
| <i>T</i>     | Total                 |
| <i>u</i>     | Upstream              |
| <i>w</i>     | Waveguide             |
| <i>w</i>     | Radiation resistance  |
| <i>z</i>     | Axial direction       |
| $\delta$     | Displaced             |

**Superscripts:**

|   |                  |
|---|------------------|
| * | Complex quantity |
|---|------------------|

## SUMMARY

Excessive fluid-borne noise in hydraulic systems is a problem the fluid power industry has long struggled to address. Traditional noise control devices such as Helmholtz resonators, tuning coils, and Herschel-Quincke tubes are generally too large for fluid power systems unless the speed of sound in the device can be reduced. A compliant lining can achieve this effect, but compliance (and lossy compliance) has had little attention in noise control in general, and in fluid power in particular. One means to achieve compliance in these devices, especially at elevated pressures, is through a liner made of syntactic foam, which in this case is a urethane host matrix with embedded hollow, polymer microspheres.

The material properties at elevated pressure are unknown by the liner manufacturer, but are known to be pressure- and temperature-dependent. Therefore, the effect of hydrostatic pressures from 2.1-21 MPa and temperatures from 20-45 C on the liner properties, thus the device performance, are studied. For a Helmholtz resonator, a theoretical model is fit to experimentally-measured transmission loss of the device using a least-squares routine, which solves the inverse problem for the complex bulk modulus of the liner.

These material properties are used to compare a theoretical model of a tuning coil to experimental data, and in a parameter study of a Herschel-Quincke tube. The compliance of the liner is found to lower the effective sound speed by an order of magnitude and decrease the volume of the cavity of a Helmholtz resonator by up to two orders of magnitude. This work is expected to result in more compact noise control devices for fluid power systems.

# **CHAPTER 1**

## **INTRODUCTION**

Excessive levels of fluid-borne noise in hydraulic systems can have detrimental effects not limited to unwanted air-borne sound. Noise control devices such as Helmholtz resonators, tuning coils, and Herschel-Quincke tubes that are common for systems with air are normally unsuitable for fluid power systems, as they scale with the wavelength of sound which is four times higher in hydraulic oil than in air. Thus, they tend to be too large without some means to reduce the speed of sound, which can be achieved through the use of a compliant lining. This dissertation explores the effect of a syntactic foam lining for noise control devices for fluid power systems, as a means of raising the compliance and lowering the speed of sound. This enables more compact devices for the same performance as an unlined device. The properties of the liner are unknown above atmospheric pressure from the manufacturer; therefore, the effect of pressure and temperature on the properties of the liner, and thus the performance of the devices, is investigated. The following sections of this chapter present more detail on the motivation for the work, the research objectives, the approach taken to achieve those objectives, and an overview of the dissertation which includes a brief statement on the content of each chapter.

### **1.1 Research Motivation**

The fluid power industry has long struggled with reducing the high levels of flow ripple produced by positive-displacement pumps. The acoustic pressure and velocity in the fluid may induce such deleterious effects as cavitation and leakage. Fluid-borne noise

may also couple with structural vibrations, which can not only increase component fatigue and reduce life, but also produce air-borne sound. This sound is at best an annoyance, and at worst may be hazardous to human hearing. These effects are a factor in existing fluid power products and technologies, but are exacerbated with the push to expand the reach of fluid power into non-traditional and noise-sensitive applications such as hydraulic hybrid vehicles and devices for the home. New hydraulic system architectures such as “digital” pumps and valves and displacement control introduce new challenges as well; the former for sharp pressure pulsations and both for varying fundamental frequencies. The high energy density of fluid power is attractive to system designers, but the noise levels are often a deterrent.

A major challenge to reducing fluid-borne noise is the long wavelengths of sound in the fluid. The speed of sound in hydraulic fluid, approximately 1400 m/s, is much higher than in air. In addition, the fundamental frequency of a typical axial piston pump, commonly used in the fluid power industry, is approximately 270 Hz. At this frequency the wavelength of sound in the fluid is over 5 meters long. Furthermore, traditional noise control devices scale in size with the wavelength – therefore, to be effective at these frequencies, they would be far too large to implement without some means of lowering the speed of sound within the device. A typical means to lowering the speed of sound within a device is the use of a pressurized bladder. This is the technology found in commercially-available in-line hydraulic silencers, also known as suppressors. It is proposed that a solid, compliant liner may have the same physical effect, albeit with fewer maintenance requirements and potentially lower manufacturing cost. The material proposed for the liner is syntactic foam, which in this case is a urethane host matrix filled

with hollow, plastic microspheres. This material has the property of changing compliance based on the hydrostatic pressure it is exposed to – at what is called the critical pressure, the microspheres undergo a reversible buckling process, at which point the stiffness of the material drops sharply. At pressures higher than the critical pressure, the microspheres have collapsed and leave air pockets in the host material that continue to shrink as hydrostatic pressure is applied. Post-buckling, the material stiffness increases with increasing pressure. Thus, there is a range of hydrostatic pressures in which the syntactic foam is much more compliant relative to a pure urethane, and more importantly much more compliant than hydraulic fluid, and therefore has a much lower speed of sound.

## **1.2 Research Objectives**

The objective of this research is to characterize the performance of a syntactic foam lining in the context of traditional noise control components in a hydraulic system. The noise control devices considered are Helmholtz resonators, tuning coils, and Herschel-Quincke tubes. The material properties of the liner materials are provided by the manufacturer at atmospheric pressure, but the behavior of the material at elevated hydrostatic pressures and temperatures is unknown. Thus, this research aims to quantify the material properties, notably the bulk modulus, and their effect on the performance of the device, at elevated pressures and temperatures for two different sizes of microspheres.

## **1.3 Research Approach**

A prototype Helmholtz resonator and tuning coil were constructed for the purpose of evaluating the effect of the syntactic foam liner on the transmission loss at various temperatures and pressures. Six prototype liners – three unvoided, and three voided, were

produced by Goodrich Corporation. The microspheres of the voided liners are plastic and have a mean diameter of 80 microns. The voided liners have densities that vary from 540-633 kg/m<sup>3</sup>. The unvoided, or “neat,” liners have the same host material as the voided liners, but are cast without microspheres. The first set of liners were tested at static pressures up to 6.9 MPa. One of the host matrix materials was selected and manufactured with microspheres with a mean diameter of 20 microns (combined with thicker walls, a higher buckling pressure) and tested at pressures up to 20.7 MPa. All liners were tested from pressures of 2.1 to 6.8 MPa at three temperatures varying from 25 to 45 C. The transmission loss was measured to characterize the acoustic performance using the multi-point method [1-3]. Analytical models were developed that capture the relevant physics and facilitate an inverse solution of the material properties at elevated pressures. The models illuminate the effect of the bulk modulus on the speed of sound, and therefore the performance of the devices. Knowledge of these properties at elevated hydrostatic pressures may then be applied to predictive models to tailor the performance of a given device to a specific application. The understanding of the material behavior may then inform future design decisions regarding the use of syntactic foam linings in noise control devices for fluid power systems.

#### **1.4 Overview of Dissertation**

Chapter 2 presents a literature review of three devices considered in this work, a Helmholtz resonator, tuning coil, and Herschel-Quincke tube, particularly in the context of noise control in hydraulic systems. Chapter 3 discusses syntactic foam, its composition, the physical mechanism by which syntactic foam is compliant at elevated pressure, and its material properties at atmospheric pressure. Chapter 4 presents equations

that describe the deformation of a liner as a function of hydrostatic pressure, equations that show the compliance of a cavity or waveguide with respect to the elastic modulus of a liner in different geometric configurations, and summarizes the role of compliance in hydraulic noise control devices. Chapter 5 discusses the theory behind the measurement of transmission loss for hydraulic components and experimental test rig used in this research. The Helmholtz resonator is discussed in Chapter 6, including a presentation of the theoretical model, a brief parameter study to consider the impact of the liner, and the results of the material property estimate. The effect of pressure and temperature on material modulus, loss factor, and effective speed of sound are described, among others. Chapter 7 discusses the theoretical model, and a parameter study of, both the tuning coil and Herschel-Quincke tube. Experimental results for the prototype tuning coil are presented and discussed in the context of the model and the effect of the syntactic foam liner. The effect of a compliant liner on a tuning coil is expected to also hold for the Herschel-Quincke tube, thus additional experimental evaluation of the Herschel-Quincke tube is not expected to yield unique results. Finally, Chapter 8 presents the conclusions and recommendations for future work.

## **CHAPTER 2**

### **LITERATURE REVIEW**

This chapter presents a literature review for the three devices studied in this research, the Helmholtz resonator, tuning coil, and Herschel-Quincke tube. Both published research and issued patents are considered, with the focus being noise control devices for fluid power systems and devices where the compliance of a lining or use of a filling in a cavity or waveguide is exploited. To conclude, a discussion of the research opportunity available from gaps in the literature is presented.

#### **2.1 Helmholtz Resonator**

The theory of the cavity resonator was first presented by Helmholtz in 1860, and is now referred to as a Helmholtz resonator [4]. Schematically depicted in Figure 2-1, it is the acoustic analog of a mechanical spring-mass-damper, and acts as a notch filter in acoustic noise control applications. The acoustic equivalent of the mass is the mass of fluid in the neck, the spring is the bulk modulus of fluid in the cavity, and damping is associated with the viscous motion of the fluid in the neck, acoustic radiation into the cavity from the neck opening, and any losses associated with bulk motion in the cavity.

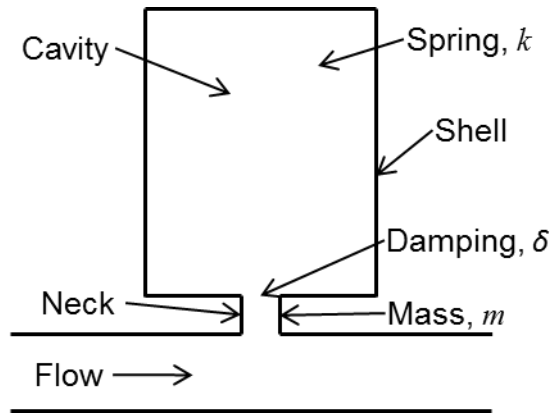


**Figure 2-1: Schematic of a Helmholtz resonator.**

Helmholtz resonators have been studied extensively for fluid power systems in the past few decades. Kojima and Edge [5] and Lau, et al. [6] studied the transmission loss of metallic-bellows style Helmholtz resonators. They reported resonance frequencies of 300 – 500 Hz, and the devices were quite small, with the volume of the bellows as low as 5.03 cm<sup>3</sup>, with neck lengths from 23.0 – 48.2 mm. The gas-filled bellows act as compliant elements within the cavity; an increased compliance results in lower resonance frequencies for the same size device. Unfortunately, no other information on these devices can be found. Kojima and Ichiyanagi [7] studied a Helmholtz resonator filter network to generate multiple resonances. Ijas and Virvalo [8] also studied the Helmholtz resonator for use in a hydraulic system, in addition to ¼-wave resonators and accumulators. Their design demonstrated optimal performance with a 40 cm long neck and a cavity that was 80 mm wide and 50 cm long; the authors wrote that “It is difficult to install this kind of damper in mobile machines,” referring to its size. Vael, et al. [9] designed a Helmholtz resonator to attenuate a resonance within their pump design; the device had a resonance frequency of 3490 Hz. This frequency is far higher than typical fundamental frequencies of hydraulic pumps, and would thus have little effect on the overall noise level. Bügener, et al. [10] studied the use of Helmholtz resonators for

cavitation reduction. The fundamental concept is the zero-impedance condition at the entrance of the resonator results in phase cancellation – this would reduce the negative-going pressure pulse at the suction port when the resonator is mounted close to the port. However, their device was both large (2 L volume) and its resonance frequency did not appear to correlate with the fundamental pumping frequency of the system. As with Vael, et al., the authors expressed the sentiment that “...it is too space-consuming and not suitable for industrial applications. A significant downsizing is necessary.” Kela [11, 12] and Kela and Vähöja [13] studied the controllability of variable-volume Helmholtz resonators. None of the devices found in the literature for hydraulic systems apply a compliant lining, and thus are either impractically large or have high resonance frequencies.

Photiadis [14] studied, theoretically, the effect of wall compliance on the resonance frequency of a spherical Helmholtz resonator underwater, and concluded that the compliance would lower the resonance frequency. A report by the Naval Underwater Systems Center, and several related papers, detailed oil-filled Helmholtz resonators for underwater sound sources packed with compliant tubes to raise the cavity compliance [15-18]; other variations included an air bladder within the cavity. The report by Woollett [15] states that for increasing pressure, the tubes must be increasingly thick and thus less compliant, and for depths of more than 1000 m (pressures of approximately 10.2 MPa) the tubes should be omitted entirely. The relevance to this work is both the high-pressure environment and the effort to raise the cavity compliance through a compliant element. With the exception of the gas bellows-style devices, for which no theoretical development is found in the literature, the physical causes and effects of raising cavity

compliance has not been exploited in Helmholtz resonators for hydraulic systems and is thus a major thrust of this work.

For resonators designed for use with air, the use of a fibrous lining has been studied to lower the resonance frequency and increase the damping. Selamet, et al. [19] studied such a device and found that the resonance frequency shifted down up to 20% from the unlined case with increased lining thickness. The frequency shift is attributed to the flow resistivity of the lining; increasing its thickness lowered the resonance frequency. Resistance, however, impacts only the damping and does not change the resonance frequency. An isothermal model for the sound propagation through the fibrous material could also account for a lower sound speed in the lining material, as found in Pierce [20], thus making the resonator acoustically larger and shift the resonance frequency down. However, this phenomenon is not addressed by the authors. Yu, et al. [21] also performed a study on resonators with absorbing material in the cavity but with T-shaped devices, where similar changes in the resonant frequency and damping were observed.

Lastly, Helmholtz resonators have been used to measure the bulk modulus and viscosity of liquids. In a paper by Ehler [22], the authors constructed a resonator that was pressurized by nitrogen and used a transducer to excite the resonances of the cavity. The bulk modulus was calculated by the frequencies of the resonances and the viscosity was calculated by the quality factor of the resonances. The authors report agreement within 2.5% of the bulk modulus with other techniques available at the time, for liquids such as ethanol, benzene, and acetone.

## 2.2 Tuning Coil

The basic operation of a tuning coil is that of a  $\frac{1}{4}$ - or  $\frac{1}{2}$ -wave resonator, depending on the specifics of the construction. For this work, the tuning coil will be treated as a concentric  $\frac{1}{4}$ -wave resonator, as the  $\frac{1}{2}$ -wave case will be considered a Herschel-Quincke tube.  $\frac{1}{4}$ -wave resonators have been traditionally studied as T-branches, shown in Figure 2-2a, such as in the recent work for hydraulic systems by Kojima and Ichiyangi [7, 23]. Kojima and Ichiyangi addressed two versions of their “variable resonance-mode type side-branch” device, one with a section of rigid pipe and one with the same section made of hose. The device that used hose takes advantage of the slower speed of sound through the hose (1090 m/s as opposed to 1410 m/s) to both make the device slightly smaller and lower the resonance frequencies. A schematic of their device is shown in Figure 2-4. A tuning coil, as originally patented by Klees in 1967 [24], is constructed as a concentric resonator instead of a branch, shown in Figure 2-2b. Tuning coils were studied in the mid-1990s for automotive power steering systems by a number of researchers. Strunk [25] studied a “cross-loop attenuator” that functions as a side-branch quarter-wave resonator. Hastings and Chen [26], Drew, et al. [27], and Dodson, et al. [28] studied concentric-type tuning coils which use small, flexible hose within a larger pressure-bearing hose section. The study by Drew included many factors in practical tuning coils that are not a factor in this work; for example, the tuner was composed of a flexible inner annulus in which leakage must be accounted for. An example of this inner annulus, commonly referred to as a hose tuner, is shown in Figure 2-3. The device presented in this research has a rigid inner annulus with no leakage. The study by Hastings and Chen used a sound speed that was modified due to the compliant wall of the

tuning coil, although its value was not stated. The paper by Dodson measured the insertion loss of side-branch and concentric resonators. In addition, the authors performed a time-of-flight measurement on the speed of sound in hydraulic hose, and found that it varied with pressure from “795 m/s at ambient pressure to 1085 m/s at 5 MPa to 1115 m/s at 10 MPa.” Their 1-dimensional model did not match the measured insertion loss data very well, even with the measured wave speeds. Furthermore, their measurements were performed using PVDF strips applied to the outside of the hose, and not pressure transducers directly exposed to the fluid, so structural vibration of the hose may be affecting their measurements. A study of extended-tube expansion-chamber-style devices and multi-chamber cable-hose devices was undertaken by Munjal and Thawani [29]. Their two-chamber device had chambers of 0.17 and 0.34 m long, but had a maximum effectiveness at 5 kHz, which is far too high to be effective for typical hydraulic systems. There are many patents for devices of similar construction to Klees’ device, however, one that used compliant pressurized bladders in the side-branch path of a concentric tuning coil was issued to Knapp in 1997 [30]. One figure from this patent is shown in Figure 2-5, where the space labeled 27 in the figure is a pocket of air encapsulated by an elastic bladder, 26. This construction is most similar to the device studied in this work, except here a solid, compliant material is used instead of a pressurized bladder.

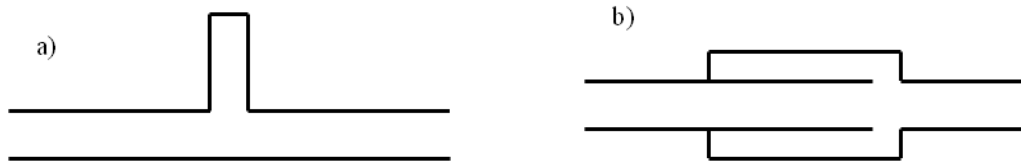


**Figure 2-2: 1/4-wave resonator configurations: a) T-branch b) Concentric.**



**Figure 2-3: Hose tuner.**

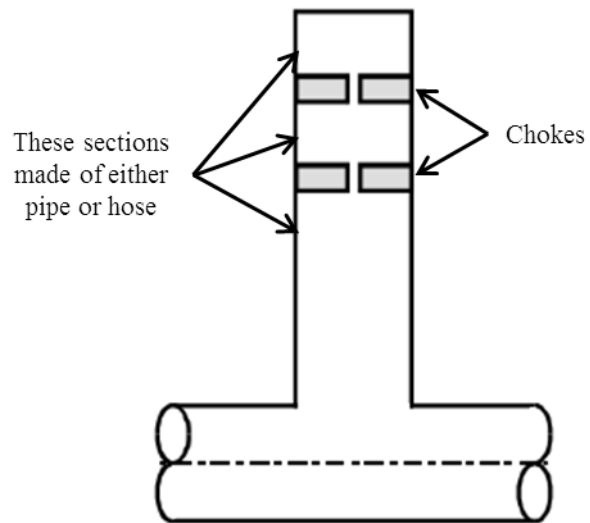


**Figure 2-4: Kojima and Ichiyanagi's "variable resonance-mode type side-branch resonator."**

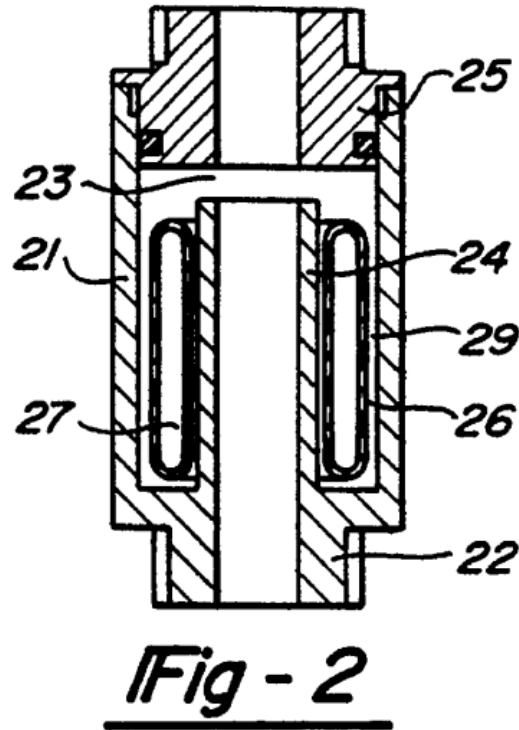
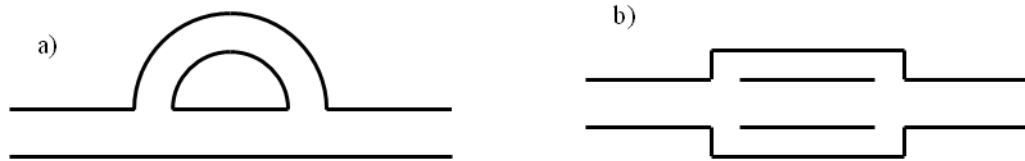


Figure 2-5: A schematic of the bladder-style tuning coil from a patent assigned to Knapp [30].

### 2.3 Herschel-Quincke Tube

A Herschel-Quincke (HQ) tube is a  $\frac{1}{2}$ -wavelength resonator. A schematic of two configurations of HQ tube are shown in Figure 2-6, the traditional parallel-branch configuration is shown in Figure 2-6a, and the concentric configuration is shown in Figure 2-6b. Noise reduction occurs through phase cancellation when the waves in the parallel paths are 180 degrees apart in phase at the reconnection point. This phase difference can be achieved by one or both of a difference in path length or a change in the speed of sound down one path. The Herschel-Quincke tube was first theorized in 1833 [31] and significant contributions were made by Stewart in 1928 [32]. It has seen recent consideration in studies by Selamet, et al. [33] and Selamet and Easwaran [34]; both address systems with air. The latter addresses the use of multiple, parallel, identical tubes to maximize the effect of the Herschel-Quincke tube. Poirier, et al. [35] developed a

higher-order model of a set of parallel HQ tubes around a single duct that accounted for the shape of the connection between the circular paths, and achieved good agreement with their analytical and numerical models. None of these papers addresses a concentric configuration; a concentric  $\frac{1}{2}$ -wave resonator appears to be generally considered as a version of a tuning coil. It is treated as such by Chen and Hastings [36], who perform a complete analysis of the concentric Quincke tube as presented by Klees [37] in his patent for a tuning coil for a fluid system.



**Figure 2-6: Herschel-Quincke tube configuration: a) Traditional b) Concentric.**

A number of patents have been found for  $\frac{1}{2}$ -wavelength resonators that refer specifically to hydraulic systems. One such is a Pulsation Dampener by Burton [38] that consists of a long flexible tube with the ends adjacent in the hydraulic line for phase cancellation. Two patents have been found that use a perforated or dissipative lining for one of the flow paths; a patent by Giordano [39] uses a perforated outer annular cavity for muffling an internal combustion engine, and Ingard [40] used a dissipative liner for air systems: however, both patents refer to systems with air. No patents or research works have been found for devices with compliant linings for hydraulic systems, although it is generally known that the compliance of hydraulic hose lowers the sound speed [41]. The proposed work seeks to exploit this effect on a larger scale by incorporating a compliant liner into the annular path of the device – the slower the sound speed in the annular path, the more compact the device can be for a given resonance frequency.

## **2.4 Research Opportunity**

It can be concluded from a review of the literature that compliance has largely not been exploited for noise control devices in general, and more specifically for fluid power systems. While the lower sound speed within hoses is well-known (and exploited in tuning coils), the achievable compliance is material- and construction-limited. The hose must be stiff enough to contain the static pressure, while being soft enough to lower the sound speed to the desired level. Some means of introducing compliance in Helmholtz resonators have been found, namely gas-filled bellows and compliant tubes, but no theoretical development of the bellows-style devices has been found and the compliant tubes have pressure limitations. In the patent literature, there is some use of elastomeric linings but no corresponding theoretical development.

This work seeks to significantly increase the compliance of a cavity or waveguide in noise control devices for fluid power systems through investigation of a solid, compliant lining material. The material being investigated, as the means to achieve compliance, is syntactic foam, which in this case is comprised of a urethane host matrix with embedded hollow, polymer microspheres, and is described in more detail in the next chapter.

## **CHAPTER 3**

### **SYNTACTIC FOAM**

Syntactic foam is a term used to describe both plastic and metal composites composed of a uniform host matrix with hollow microspheres. The syntactic foam studied in this research is composed of a urethane host matrix with plastic microspheres, or microballoons. Most plastic foams are voided chemically, where the voids that comprise the foam are produced by gasification. Alternately, syntactic foams are mechanically voided by the inclusion of hollow microspheres before the host material sets. The advantage of syntactic foam is that it is closed-cell, which makes it relatively impermeable, stronger than conventional, open-cell foams, and has a controllable void size. The voiding also considerably lowers the density relative to a homogeneous host material; as such, syntactic foams have long been used for buoyancy on buoys and submersibles. Syntactic foams have also been studied for use as anechoic wall coatings for water tanks, some with glass microspheres, and some made of Bakelite, but these studies consider mostly ultrasonic frequencies [42-45]. Design of a lining for hydraulic silencers is different than anechoic linings for acoustic water test tanks in a number of crucial ways: the pressures in hydraulics are significantly higher, the frequencies of interest are significantly lower, and in water tanks, the lining is designed to be acoustically transparent while very lossy. For hydraulic silencers, an impedance mismatch of the liner to the fluid is the objective.

The physical properties of syntactic foam are dependent on frequency, temperature, and static pressure. The urethane host material used in this research exhibits viscoelastic behavior, which means the stress and strain are not necessarily in phase. Of

particular interest to this work is the behavior of the bulk modulus, which can be broken out into two components, represented as a complex function

$$K^* = K' + iK'' \quad (2.1)$$

where  $K'$  is the storage modulus and  $K''$  is the loss modulus. The tangent delta is the ratio of the loss modulus to the storage modulus,

$$\tan \delta = \frac{K''}{K'} \quad (2.2)$$

and is a measure of the viscous behavior of the material. A tangent delta of 0 means there is no time delay between stress and strain. The frequency-dependent behavior of a syntactic foam sample used in this work, provided by the manufacturer, is shown in Figure 3-1, in which the bulk modulus and tan delta are shown for three temperatures at ambient pressure. The bulk modulus and tangent delta curves shift toward higher frequencies with increasing temperature, at the rate of approximately one decade per 10 degrees Celsius. The bulk modulus governs the speed of sound of compression waves by the relationship

$$c = \sqrt{\frac{K}{\rho}} \quad (2.3)$$

where  $c$  is the speed of sound,  $K$  is the bulk modulus, and  $\rho$  is the density. Since the size of resonant noise control components typically scale with the wavelength,  $\lambda$ , and  $\lambda f = c$ , designing a compact device requires small wavelengths, hence a low sound speed and low bulk modulus of the lining material. Therefore, a low bulk modulus, especially at elevated hydrostatic pressure, is necessary for designing compact devices.

The mechanism by which a polymer-microsphere syntactic foam becomes compliant is the buckling of the microspheres at a critical pressure. A study by Trivett, et

al. [46] described the effect of microspheres on the bulk modulus of a Castor oil solution. At low pressure, the microspheres are effectively rigid particles and raise the bulk modulus of the material. This effect was quantified by Guth [47] using the volumetric concentration of the particles in the material,  $\phi$ , by

$$K' = K \left[ 1 + 2.5\phi + 14.1\phi^2 \right]. \quad (2.4)$$

However, the microspheres in the solution buckle as the hydrostatic pressure reaches the critical pressure of the microspheres, also called the elastic stability limit, given by [48]

$$P_{cr} = \frac{2Et^2}{r^2 \sqrt{3(1-\nu^2)}} \quad (2.5)$$

where  $E$  and  $\nu$  are the Young's modulus and Poisson's ratio of the sphere material,  $t$  is the thickness of the shell, and  $r$  is the mean radius. This formula is valid for thin shells, where the ratio of radius to thickness is greater than 10. Two screenshots of a video that shows the buckling of a microsphere are shown in Figure 3-2a for the unbuckled state and Figure 3-2b for the buckled state [49]. The compliance of the material increases post buckling, as the stiffness of the microspheres is now that of a gas bubble. The gas bubble is what remains of the void in the urethane that was originally occupied by the fully spherical microsphere. The compliance continues to increase as pressure increases, and levels off at a value approximating that of the host matrix. In short, it is the buckling action of the microspheres that lowers the bulk modulus with increasing hydrostatic pressure in the range of pressures just above the critical pressure. More rigorous mathematical analysis of spherical shell buckling near the stability limit of microspheres in an elastic matrix was presented by Jones [50]: this work assumed linear elasticity, but

noted that a more complete analysis of the buckling phenomenon would require nonlinear elasticity and finite element analysis.

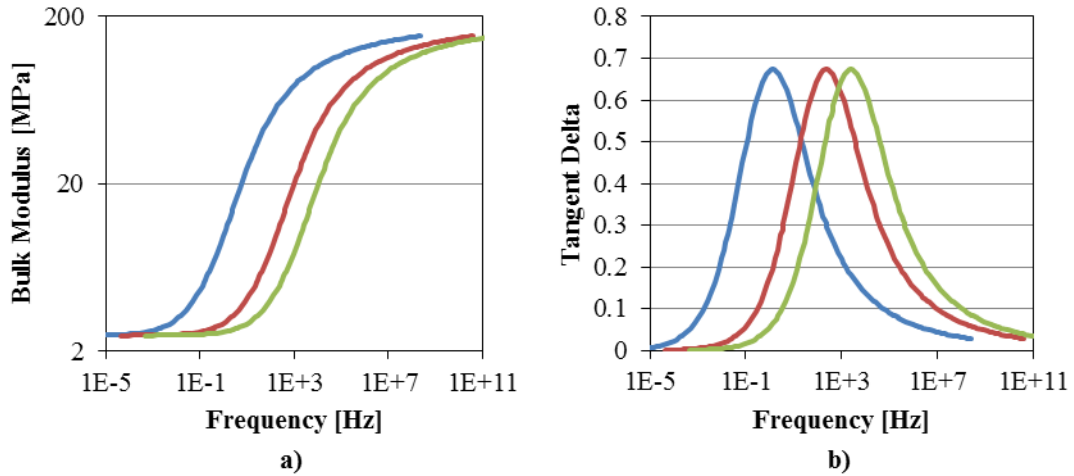


Figure 3-1: a) Bulk modulus and b) tangent delta for a urethane-host syntactic foam at: — 20 C, — 35 C, — 45 C.

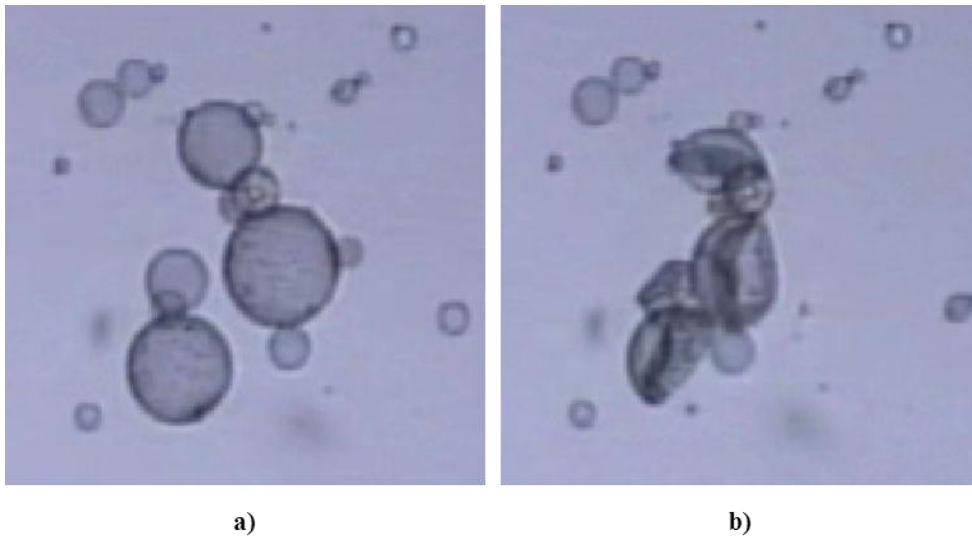


Figure 3-2: a) Expancel microspheres at atmospheric pressure and b) post-buckling [49].

With respect to the prior research into syntactic foams, one patent has been found that refers to the use of syntactic foam (or more generally, microvoided elastomers) in a hydraulic noise control device. A patent issued to Wheeler [51] refers to an in-line hydraulic silencer with syntactic foam-lined flow paths. Wheeler’s syntactic foam used

glass microspheres instead of plastic; glass microspheres fracture instead of reversibly buckle. Furthermore, it would be undesirable to have glass shards shed into the hydraulic oil. Other patents refer to elastomers but not specifically syntactic foam; a patent issued to DiRe [52] describes a lined outlet chamber for a pump to reduce pressure pulsations where the liner is a closed-cell, chemically voided polyester. Likewise, a patent issued to Hansen [53] is a lined in-line silencer where the lining is elastomeric, but makes no reference to voids in the elastomer. None of these products are known to be in commercial use nor is there published research on such devices. In addition, these devices are in-line, single-path flow arrangements – no patents or literature have been found that refer to use of syntactic foam in the devices studied in this research.

## CHAPTER 4

### COMPLIANCE

This chapter discusses the sources of compliance within a noise control device for fluid power systems, such as compliant linings, entrained air, and the compliance of the device shell. First, in order to examine the compliance of the structure or lining, the equations for deformation of a cylinder or cylindrical shell (originally derived by Timoshenko [54]) under hydrostatic pressure with different boundary conditions are presented. This is used in two ways: first, the deformation of a liner informs the change in volume of the liner within a cavity or the change in outer radius when a waveguide is formed between the liner and a rigid shell. Second, the equations for deformation of a liner are used to analyze the compliance of different liner geometries, such as whether it is free in a cavity or bonded to the inner wall of a cavity. The compliance of a liner or structure wall is calculated according to Manring [55] for each case. At the end of the chapter, the effects are totaled into a single metric for compliance.

#### 4.1 General equations

A partial presentation of the derivation of the displacement of a cylinder or cylindrical shell is shown here for the edification of the reader; a complete derivation presented in Timoshenko [54] is shown in Appendix A. For all cases, the general solution to the radial displacement is given by

$$u_r = C_1 r + \frac{C_2}{r} \quad (3.1)$$

where  $u_r$  is the radial displacement,  $r$  is the radial coordinate, and  $C_1$  and  $C_2$  are constants. Boundary conditions on the displacement can be handled directly in Equation (3.1), in

combination with stress boundary conditions which are applied to determine the constants. The stresses are given by:

$$\sigma_r = \frac{E}{1-\nu^2} \left[ C_1(1+\nu) - C_2 \frac{1-\nu}{r^2} \right] \quad (3.2)$$

$$\sigma_t = \frac{E}{1-\nu^2} \left[ C_1(1+\nu) + C_2 \frac{1-\nu}{r^2} \right] \quad (3.3)$$

where subscripts  $r$  and  $t$  reflect the radial and tangential coordinates and  $\nu$  is the Poisson's ratio. The constants  $C_1$  and  $C_2$  are solved through the boundary conditions of stress and displacement at either the inner or outer surface, which then determine the displacement by Equation (3.1). Then, Hooke's law in three dimensions in cylindrical coordinates is used to find the displacement in the axial, or  $z$ , direction given the stresses in the radial plane;

$$\frac{\partial u_z}{\partial z} = \frac{1}{E} \left[ \sigma_z - \nu(\sigma_r + \sigma_t) \right]. \quad (3.4)$$

#### 4.1.1 Dimensions

The radii in the following equations, and the rest of this dissertation, adhere to a consistent numbering scheme. Since the devices considered are of similar construction, this is a convenient representation. The radii are shown graphically in Figure 4-1 and numbered according to the description in Table 1.

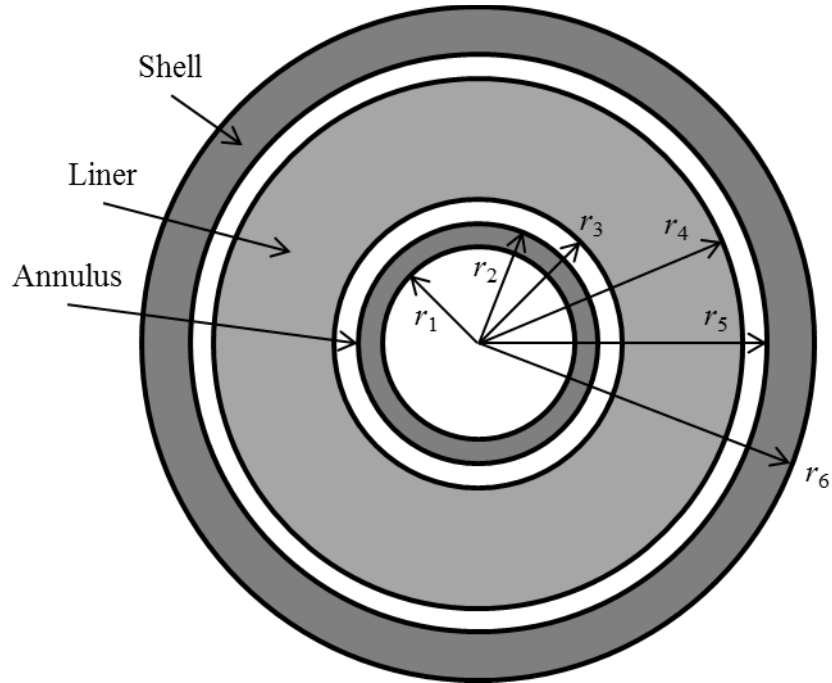


**Figure 4-1: Schematic of device cross-section with labeled components and radii.**

**Table 1: List of dimensions and their description.**

| Dimension | Description             |
|-----------|-------------------------|
| $r_1$     | Inner radius of annulus |
| $r_2$     | Outer radius of annulus |
| $r_3$     | Inner radius of liner   |
| $r_4$     | Outer radius of liner   |
| $r_5$     | Inner radius of shell   |
| $r_6$     | Outer radius of shell   |

## 4.2 Hydrostatic deformation

A thick cylindrical shell exposed to elevated, uniform hydrostatic pressure has equal stresses in all directions, equal to the negative of the external pressure;

$$\sigma_r = \sigma_t = \sigma_z = -p. \quad (3.5)$$

The subscripts  $r$ ,  $t$ , and  $z$  correspond to the radial, tangential, and axial directions. A cylinder or cylindrical shell will deform in all directions symmetrically about both the central axis and medial plane. The displacement is decoupled in the radial and axial directions, such that the radial displacement is given by

$$u_r = -\frac{P}{E_L}(1-\nu_L)r \quad (3.6)$$

and the axial displacement is given by

$$u_z = -\frac{P}{E_L}(1-2\nu_L)z \quad (3.7)$$

where  $z$  is the axial position along the cylinder and  $E_L$  is the bulk modulus of the liner. These dimensional changes also inform the change in total volume, and if the mass of the liner is known the density can also be determined. It is important to note that the sign of the displacements in Equations (3.6) and (3.7) are both negative. This implies that, for pressures above atmospheric, the liner will shrink in both the axial and radial directions, and that this behavior is not dependent on the size or aspect ratio of the liner.

The condition of uniform hydrostatic stress may be desirable for devices seeking to exploit the compliance of syntactic foam. If the stress throughout the syntactic foam is uniform, all microspheres through the material would be buckling at the same static pressure and the bulk stiffness of the material would be relatively predictable.

### 4.3 Cavity Compliance

The procedure for calculating the compliance of a cavity with a particular geometry and material properties is developed below and is found in Manring [55]. A correction for the speed of sound in an elastic tube, as opposed to that in a rigid pipe, is a static analysis that dates back to the 19<sup>th</sup> century, and for the specific case of an elastic, thin-wall cylindrical tube is referred to as the Korteweg-Lamb correction [56-58], and can be found in acoustics texts [59]. The method for calculating the effective bulk modulus of a cavity (and later in this chapter, waveguides) involves writing the equation

for the fluid volume of a cavity (or for a waveguide, the cross-sectional area) and expanding the dimensions of the cavity walls, such as radius or length, with equations for deformation as a function of pressure and material properties. Then, higher-order terms are eliminated. The resulting expression for volume is separated into the “effective volume” and “displaced volume,” which correlate to the original volume and the difference between the pressurized, expanded volume and the original volume of the cavity. A derivative is taken of the displaced volume with respect to pressure; this term and the effective volume are then substituted into an equation for compliance.

#### 4.3.1 Empty cavity

The first case under consideration is that of a right cylindrical cavity with thick walls, as is the case for the shell of a noise control device for a hydraulic system. As a first approximation, only uniform radial expansion of the walls is considered, with axial extension of the shell ignored. The boundary conditions for displacement of the shell are a stress at the inner radius equal to the negative of the hydrostatic pressure and an outer radius at zero gage pressure. The internal pressure is  $p$  and the external pressure is zero. The displacement of the inner and outer boundaries under these conditions are

$$u_{r_5} = \frac{pr_5}{E_S} \left[ \frac{r_6^2 + r_5^2}{r_6^2 - r_5^2} + \nu_S \right], \quad (3.8)$$

$$u_{r_6} = \frac{2p}{E_S} \left[ \frac{r_5^2 r_6}{r_6^2 - r_5^2} \right], \quad (3.9)$$

where  $E_S$  and  $\nu_S$  are the Young's modulus and Poisson's ratio of the wall and the subscript  $S$  refers to the shell (as opposed to the liner). To determine the compliance of

the cavity (with volume  $V_c$ ), the volume is split into the effective ( $V_e$ ) and displaced volumes ( $V_\delta$ ) after an expansion of  $r_5$ ,

$$V_c = \pi r_5^2 L_S. \quad (3.10)$$

The radius is expanded by the displacement,  $u_r$ , such that the volume becomes

$$\begin{aligned} V_c &= \pi (r_5 + u_r)^2 L_S \\ &= \pi \left( r_5^2 + 2r_5 u_r + u_r^2 \right) L_S \\ &= \underbrace{\pi r_5^2 L_S}_{\text{Effective Volume}} + \underbrace{2\pi r_5 u_r L_S}_{\text{Displaced Volume}}, \end{aligned} \quad (3.11)$$

where the effective volume and displaced volume are:

$$V_e = \pi r_5^2 L_S; \quad (3.12)$$

$$V_\delta = 2\pi r_5 u_r L_S. \quad (3.13)$$

Then, the radial displacement from Equation (3.8) is substituted into the displaced volume from Equation (3.11), and then a derivative is taken with respect to pressure, yielding

$$\frac{dV_\delta}{dp} = \frac{2\pi r_5^2 L_S}{E_S} \left( \frac{r_6^2 + r_5^2}{r_6^2 - r_5^2} + \nu_S \right). \quad (3.14)$$

Finally, these equations are substituted into the equation for compliance,

$$\frac{1}{\beta_c} = \frac{1}{V_e} \frac{dV_\delta}{dp} = \frac{2}{E_S} \left( \frac{r_6^2 + r_5^2}{r_6^2 - r_5^2} + \nu_S \right). \quad (3.15)$$

A few insights may be reached from examination of Equation (3.15). The compliance of the cavity is independent of hydrostatic pressure – pressure is not a variable in the equation, and the dimensions of the inner and outer radius in the equation are those of the cavity at atmospheric pressure. Furthermore, by rearranging Equation (3.15) in terms of a thickness,  $t = r_6 - r_5$ , and a mean radius,  $r = (r_5 + r_6)/2$ , and dividing by  $r^2$  yields,

$$\frac{E_s}{2\beta_c} = \frac{\left(\frac{t}{r}\right)^2 + 4}{4\left(\frac{t}{r}\right)} + \nu_s. \quad (3.16)$$

The left- and right-hand sides of Equation (3.16) are non-dimensional, and this equation implies that for given material properties of the shell, increasing the thickness-to-mean radius ratio,  $t/r$ , will decrease the compliance. This equation is plotted in Figure 4-2 to show the behavior of the non-dimensional compliance with respect to the thickness ratio. A thickness ratio of 2 is a physical limit: at this point, the inner radius of the shell vanishes.

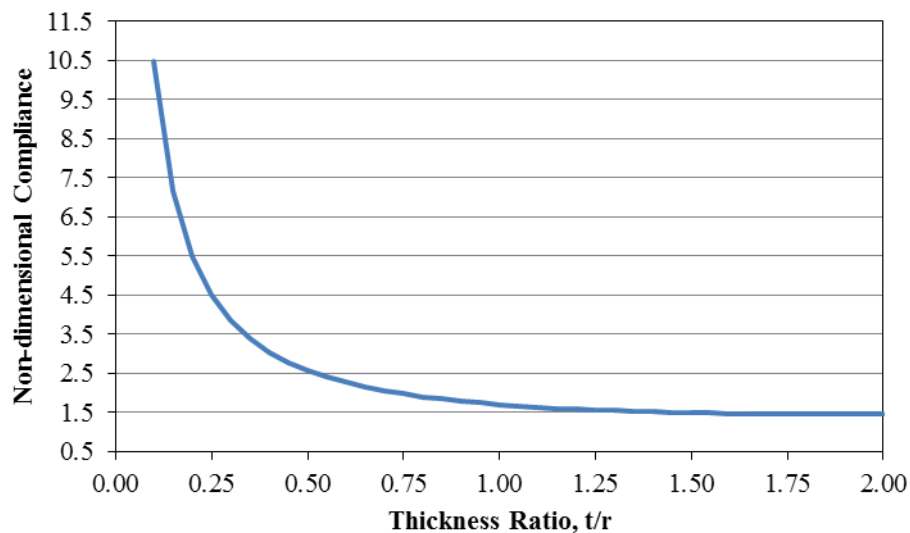


**Figure 4-2: Non-dimensional compliance of an empty shell with internal hydrostatic pressure as a function of the ratio of the wall thickness to mean radius.**

#### 4.3.2 *Solid cylinder*

Similar to the empty cavity, the compliance of a cavity with a solid, elastic cylinder inside can be calculated. In this case, the shell of the cavity is assumed to be perfectly rigid, but the elastic cylinder inside deforms and changes the effective fluid

volume. In this case, including both radial and axial deformation of the cylinder, the compliance is

$$\frac{1}{\beta_c} = \frac{L_L r_4^2}{E_L (L_S r_5^2 - L_L r_4^2)} (3 - 4\nu_L) \quad (3.17)$$

where  $E_L$  is the bulk modulus of the liner and  $\nu_L$  is the Poisson's ratio of the liner. Equation (3.17) can be rewritten in terms of volumes by

$$\frac{1}{\beta_c} = \frac{V_L}{E_L (V_c - V_L)} (3 - 4\nu_L). \quad (3.18)$$

From Equation (3.18), the cavity compliance is directly proportional to liner compliance. Furthermore, both increasing the Poisson's ratio of the liner and increasing the ratio of the liner volume to cavity volume increases the compliance.

#### 4.3.3 Annular cylinder

Also similar to the empty cavity and the solid cylinder, the compliance of a cavity with an elastic liner in the form of a hollow cylinder can be calculated. The compliance is

$$\frac{1}{\beta_c} = \frac{L_L (r_4^2 - r_3^2)}{E_L [L_S r_5^2 - L_L (r_4^2 - r_3^2)]} (3 - 4\nu_L) \quad (3.19)$$

which can also be rewritten in terms of volumes by

$$\frac{1}{\beta_c} = \frac{V_L}{E_L (V_c - V_L)} (3 - 4\nu_L). \quad (3.20)$$

Since equation (3.20) and (3.18) are identical, the difference in the cavity compliance is only a function of the volume of the liner. Thus, a cavity with either a solid or annular cylindrical liner of the same volume and the same material properties will have the same compliance.

## 4.4 Waveguide compliance

It is well-known that a waveguide with compliant walls will have a lower speed of sound than one with rigid boundaries; such is the case for hydraulic hose as compared to rigid pipe [60]. As was the case when considering cavity compliance, the compliance of different configurations of a liner within a rigid shell will be presented. Then, a comparison is made that evaluates which configuration may be the most advantageous in terms of maximizing the compliance of the waveguide formed between the liner and the shell, or between the liner and a rigid annulus. The higher the wall compliance, the lower the speed of sound and the shorter may be devices such as tuning coils and Herschel-Quincke tubes.

### 4.4.1 Solid/Annular Cylinder

The procedure used to calculate cavity compliance is similarly applied here, except only cross-sectional areas and radial displacements are used, as opposed to volumes. Only long pipes are considered here such that axial displacement of the liner is ignored. The compliance of the waveguide formed by the annular section between the outer radius of the compliant, cylindrical liner and the inner radius of the rigid shell is

$$\frac{1}{\beta_c} = \frac{2r_4^2}{E_L(r_5^2 - r_4^2)}(1 - \nu_L). \quad (3.21)$$

This equation does not change whether the liner is a solid or annular cylinder. The displacement of the outer radius of the liner is only a function of the material properties and the non-displaced radius: the geometry of the cylinder (either solid or annular) does not impact the compliance of the waveguide. This also assumes that, for example, the inner boundary of an annular cylinder is unconstrained.

#### 4.4.2 Internal pressure and a fixed outer boundary

The second configuration of interest is that of a liner that is bonded to the inner radius of a rigid shell – this is shown schematically for a tuning coil in Figure 4-3. When the liner is exposed to elevated internal pressure, it will deform radially; this deformation can be assumed uniform around the circumference of the shell. Two cases are of interest: first, the compliance of the waveguide in the entire inner space (that is, without an annulus), and second, the compliance of the space between the liner and a rigid annulus. The first case is the same as for a lined silencer or a lined pipe or hose with a rigid outer boundary, since no annulus is considered. For this case, the compliance of the entire waveguide is

$$\frac{1}{\beta_c} = \frac{2}{E_L} \frac{(1-\nu_L^2)(r_4^2 - r_3^2)}{[r_3^2(1+\nu_L) + r_4^2(1-\nu_L)]} \quad (3.22)$$

And for the second case, the compliance of the space between the liner and rigid annulus is

$$\frac{1}{\beta_c} = \frac{2}{E_L} \frac{r_3^2}{(r_3^2 - r_2^2)} \frac{(1-\nu_L^2)(r_4^2 - r_3^2)}{[r_3^2(1+\nu_L) + r_4^2(1-\nu_L)]}. \quad (3.23)$$

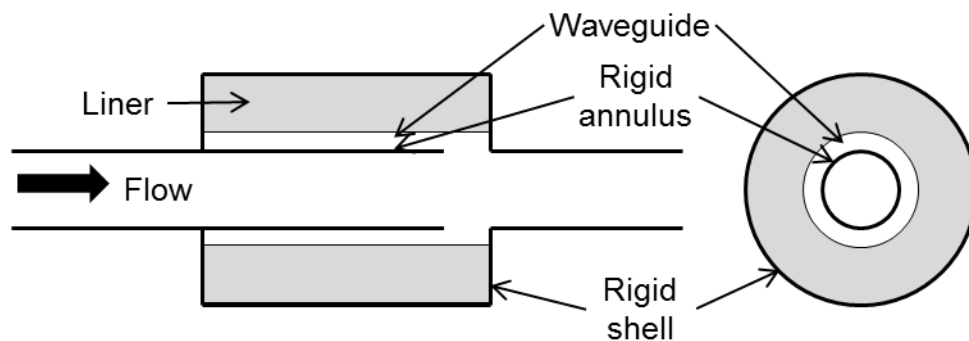
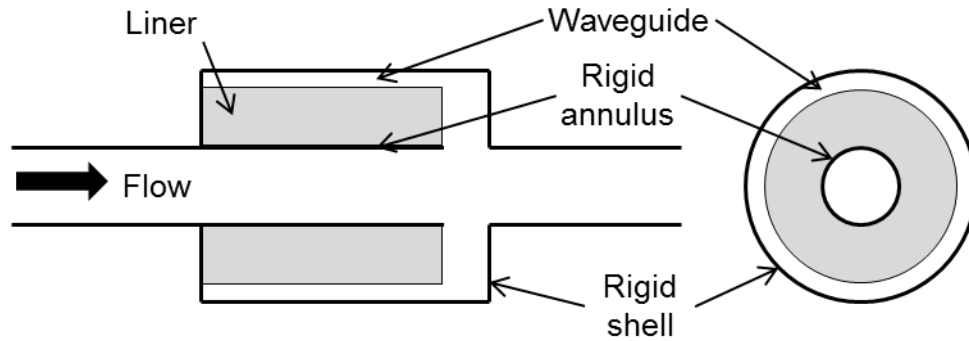


Figure 4-3: Schematic of a tuning coil with a waveguide formed between the liner and annulus.

#### 4.4.3 External pressure and a fixed inner boundary

As was discussed in Section 4.2, under hydrostatic pressure when the liner is not bonded to the outer shell, both the inner radius and outer radius will shrink. Thus, for the case of the tuning coil and Herschel-Quincke tube, the case may arise where the liner compresses enough, under increasing pressure, to tighten around the annulus. This situation then becomes a similar analysis to where the liner is bonded to the inner annulus as opposed to the outer shell. In this case, the boundary condition at the inner radius of the liner is zero displacement and only external pressure is applied to the liner. This configuration forms a gap between the liner and shell, and is shown schematically in Figure 4-4. For this case, the compliance of the waveguide is calculated to be

$$\frac{1}{\beta_c} = \frac{2}{E_L} \frac{r_4^2}{(r_5^2 - r_4^2)} \frac{(1 - \nu_L^2)(r_4^2 - r_3^2)}{[r_4^2(1 + \nu_L) + r_3^2(1 - \nu_L)]}. \quad (3.24)$$



**Figure 4-4: Schematic of a tuning coil with a waveguide formed between the liner and shell.**

#### 4.4.4 Comparison

For design purposes, it is of interest to understand which geometries may yield the highest compliance. Three cases are considered, that of the three previous sections, which evaluate the compliance of an annular waveguide in different orientations: first, a waveguide oriented between a liner and a rigid shell where the liner has unconstrained

boundaries; second, a waveguide between a rigid annulus and a liner where the liner is bonded to the inner wall of a rigid shell, and thirdly a waveguide formed between a liner and the inner wall of a rigid shell where the liner is bonded to the annulus.

First, consider a comparison between the two cases where the waveguide is formed between the outer radius of the liner and the inner radius of the shell, such as in Figure 4-4. The equations that describe the waveguide compliance for this construction were presented previously as Equation (3.21) (here denoted  $\beta_{free}$ , since the liner is not considered to be bonded to or constrained by an annulus) and Equation (3.24) (here denoted  $\beta_{outer}$  for the constrained case where the waveguide is formed by the outermost gap). Consider the dimensions of the liner and shell to be the same for the two cases, where the difference is that in the first case, the liner is not bonded or constrained around an annulus. The ratio of Equation (3.21) to (3.24), or, comparing the stiffness of the waveguides as  $\beta_{outer}/\beta_{free}$  are rewritten in terms of the cross-sectional area of the waveguide,  $S_W$ , and the total cross-sectional area,  $S_T$ , which includes the liner. Comparing the cases on the basis of cross-sectional area of the waveguide is most appropriate, since this keeps the volume velocity of the acoustic propagation in the waveguide the same for different constructions. The specific dimensions considered are listed in Table 2, along with the value of cavity stiffness at a chosen area ratio as a reference, for all the cases considered in this section. The areas of the waveguide and the total area of the cross-section, including the liner, for this first comparison are given by:

$$S_W = \pi(r_5^2 - r_4^2); \quad (3.25)$$

$$S_T = \pi(r_5^2 - r_2^2); \quad (3.26)$$

and the ratio  $\beta_{outer} / \beta_{free}$  can be written in terms of the areas by

$$\frac{\beta_{outer}}{\beta_{free}} = \frac{\frac{2\pi r_2^2}{S_T} + (1 + \nu_L) \left(1 - \frac{S_W}{S_T}\right)}{(1 + \nu_L) \left(1 - \frac{S_W}{S_T}\right)}. \quad (3.27)$$

This waveguide stiffness ratio is plotted for  $S_W/S_T$  from 0 to 1 in Figure 4-5, where 0 indicates that the liner takes up the entire cross-sectional area and there is thus no waveguide, and 1 indicates that the liner thickness approaches zero and  $S_W = S_T$ . Thus, it can be seen from Figure 4-5 that for all waveguide area ratios the case where the liner is constrained or bonded to an annulus is always stiffer, thus has a higher speed of sound, than the case where the inner radius is free to deform. Furthermore, as the liner thickness decreases, or as the ratio  $S_W/S_T \rightarrow 1$ , the ratio of stiffness between the constrained and free case increases dramatically.

**Table 2: Dimensions of two construction cases for an elastic waveguide liner.**

| Dimension              | Free                  | Outer                 | Inner                 |
|------------------------|-----------------------|-----------------------|-----------------------|
| $r_2$                  | 12.0 mm               | 12.0 mm               | 12.0 mm               |
| $r_3$                  | 12.0 mm               | 12.0 mm               | 16.0 mm               |
| $r_4$                  | 30.2 mm               | 30.2 mm               | 32.0 mm               |
| $r_5$                  | 32.0 mm               | 32.0 mm               | 32.0 mm               |
| $\beta_L$              | $1 \times 10^7$ Pa    | $1 \times 10^7$ Pa    | $1 \times 10^7$ Pa    |
| $\nu$                  | 0.45                  | 0.45                  | 0.45                  |
| $S_W / S_T$            | 0.13                  | 0.13                  | 0.13                  |
| $\beta_c$              | $3.35 \times 10^5$ Pa | $4.21 \times 10^5$ Pa | $1.00 \times 10^6$ Pa |
| $\beta / \beta_{free}$ | 1.00                  | 1.26                  | 2.99                  |

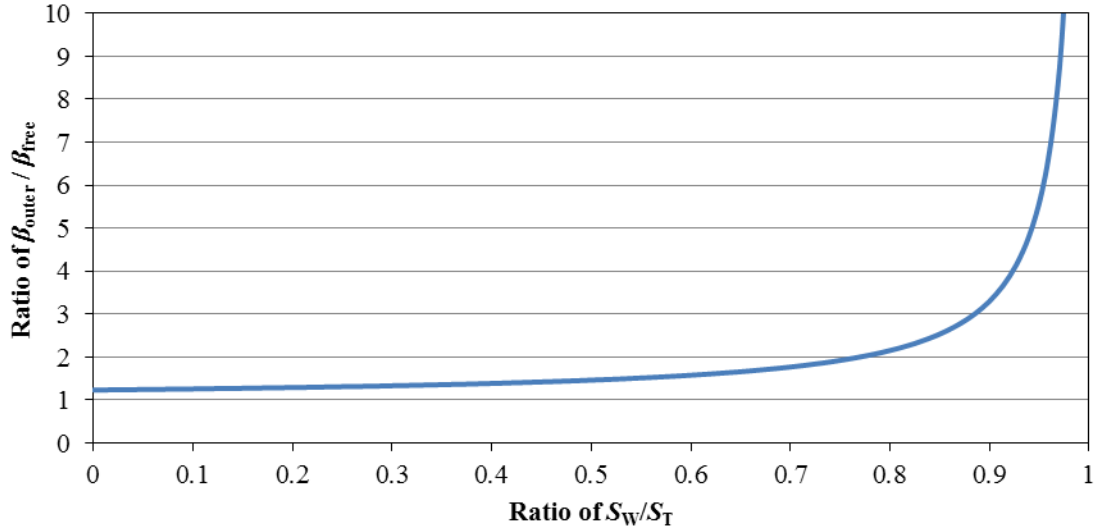


**Figure 4-5: Ratio of waveguide stiffness where the waveguide is between the liner and shell.**

The second comparison of interest is that of the  $\beta_{free}$  case, discussed previously, to the case where a waveguide is formed between a rigid annulus and a compliant liner which is bonded to the inner radius of a rigid shell, denoted here as  $\beta_{inner}$ . The compliance of the latter case was given as Equation (3.23). Between these cases, the waveguide is in a different location, thus, as with the previous comparison, the two will be compared by the cross-sectional area of the waveguide. For the  $\beta_{free}$  case, the area of the waveguide was given previously as Equation (3.25). For the  $\beta_{inner}$  case, the area of the waveguide is

$$S_{W,inner} = \pi(r_3^2 - r_2^2). \quad (3.28)$$

Since it is desired to compare the two cases for the same waveguide cross-sectional area, each equation is rearranged in terms of its respective  $S_W$ . The resulting stiffness ratio for the two cases is

$$\frac{\beta_{inner}}{\beta_{free}} = \frac{\left(1 - \frac{S_W}{S_T} + \frac{\pi r_2^2}{S_T}\right) \left(\frac{S_W}{S_T} + 1 + \nu_L \left(\frac{S_W}{S_T} - 1\right) + \frac{2\pi r_2^2}{S_T}\right)}{\left(\frac{S_W}{S_T} + \frac{\pi r_2^2}{A_T}\right) \left(1 - \frac{S_W}{S_T}\right) (1 + \nu_L)}. \quad (3.29)$$

A plot of the ratio  $\beta_{inner}/\beta_{free}$  against the cross-sectional area ratio  $S_W/S_T$  is shown in Figure 4-6. The case where the waveguide is formed between the annulus and liner, where the liner is bonded to the inner radius of the shell, is stiffer than the “free” case for all values of  $S_W/S_T$ . The stiffness ratio is highest at the extremes, and has a minimum at approximately  $S_W/S_T = 0.53$  where the ratio is 2.215.

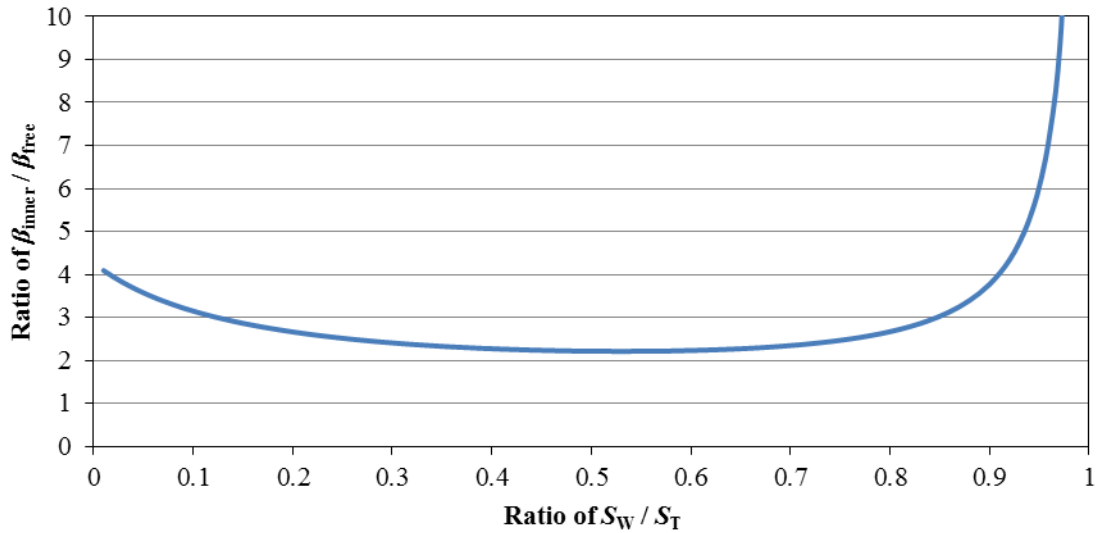


**Figure 4-6: Ratio of waveguide stiffness for two cases: a waveguide formed between an unconstrained liner and a rigid shell, and between a rigid annulus and a liner.**

Finally, for completeness, consider the ratio of the two cases where the liner is bonded either to the annulus or to the shell. As with the last comparison, these two cases have inverse construction, so the comparison will be made based on the cross-sectional area ratio of the waveguide. The waveguide stiffness ratio for this case,  $\beta_{inner}/\beta_{outer}$  is given by,

$$\frac{\beta_{inner}}{\beta_{outer}} = \frac{\left(1 - \frac{S_W}{S_T} + \frac{\pi r_2^2}{S_T}\right) \left(\frac{S_W}{S_T} (1 + \nu_L) + 1 - \nu_L + \frac{2\pi r_2^2}{S_T}\right)}{\left(\frac{S_W}{S_T} + \frac{\pi r_2^2}{S_T}\right) \left(1 + \nu_L - \frac{S_W}{S_T} (1 + \nu_L) + \frac{2\pi r_2^2}{S_T}\right)}. \quad (3.30)$$

This ratio is plotted in Figure 4-7, where it can be observed that the case where the waveguide is toward the outside, shown as  $\beta_{outer}$ , is more compliant for all values of  $S_W/S_T$ . Thus, given the choice between adhering a compliant liner to the annulus or shell, it is advantageous to adhere it to the annulus.

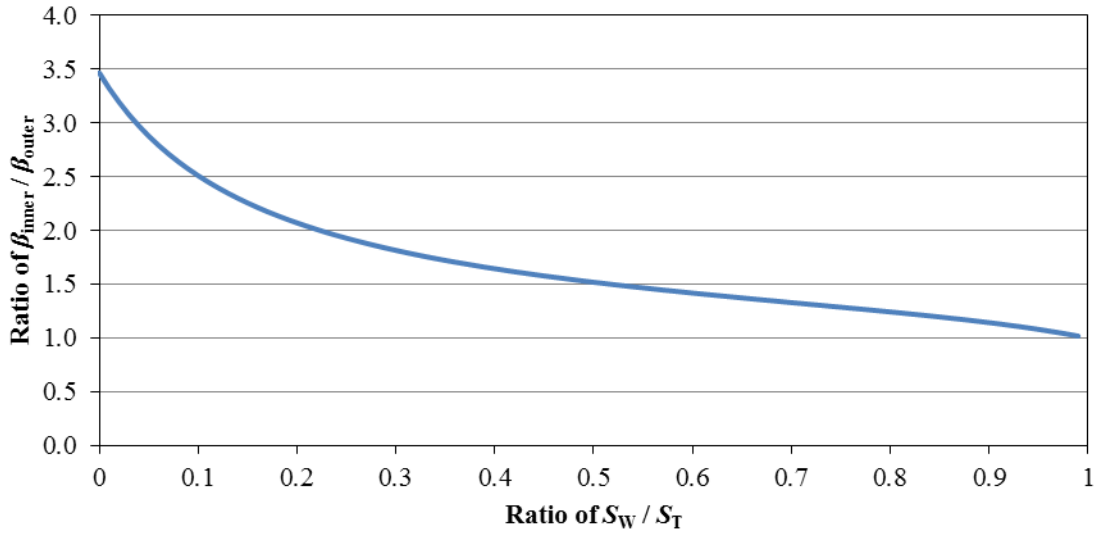


**Figure 4-7: Ratio of waveguide stiffness formed at the outer or inner boundary of a compliant liner in a rigid shell.**

#### 4.5 Sources of Compliance

In addition to the compliance of a cavity or elastic liner, other aspects of a noise control device have some degree of compliance. This includes the oil itself and any entrained air, along with difficult to quantify factors such as seals and threads. The following will discuss the compliance of each relevant aspect of the system, develop an equation that encompasses the necessary terms, and present an analysis of significance.

#### 4.5.1 Fluid

The bulk modulus of pure mineral oils (that is, without polymeric thickeners or entrained air) is a function of temperature and pressure. This was discussed by Song [61], who presented a linear, empirical equation for the secant bulk modulus of non-polymeric mineral oils,

$$\bar{K}_{p,T} \equiv K_{0,T} + A_T p, \quad (3.31)$$

where  $\bar{K}_{0,T}$  is the isothermal secant bulk modulus of the oil at atmospheric pressure and temperature, and itself is correlated to the kinematic viscosity of the fluid

$$\log(\bar{K}_{0,T}) = 0.3766 \left[ \log(\nu_{0,T}) \right]^{0.3307} - 0.2766 \quad (3.32)$$

where  $\nu_{0,T}$  is the kinematic viscosity at atmospheric pressure. The kinematic viscosity of a hydraulic fluid is readily available on its product spec sheet, usually for 40 and 100 C, and can then be extrapolated to other temperatures with an exponentially-fit curve of the form

$$\nu(T) = \nu_0 \exp(-bT). \quad (3.33)$$

where  $\nu_0$  and  $b$  are constants. The coefficient  $A_T$  is the derivative of bulk modulus with respect to pressure,  $A_T = dK/dp$ , and is linearly correlated with temperature, given by the equation

$$A_T = -0.01382T + 5.851 \quad (3.34)$$

where temperature,  $T$ , is in Celsius. It must also be noted that Equation (3.31) is for the isothermal secant bulk modulus – the isothermal tangent bulk modulus can be found by [62-64]

$$K_o = \frac{\bar{K}_{p,T} (\bar{K}_{p,T} - p)}{\bar{K}_{0,T}}. \quad (3.35)$$

The tangent bulk modulus is more thermodynamically appropriate than the secant bulk modulus, since it is the local slope of the function relating pressure to compressibility. The adiabatic bulk modulus and the isothermal bulk modulus are related by the heat capacity ratio,

$$K_A = \gamma K_T \quad (3.36)$$

where subscripts  $A$  and  $T$  refer to adiabatic and isothermal, and  $\gamma$  is the heat capacity ratio. However, Pierce states that the difference in the speed of sound using either an adiabatic or isothermal bulk modulus for liquids is very small, thus, using either is acceptable for the bulk modulus of the hydraulic oil [20]. The isothermal tangent bulk modulus for a pure hydraulic oil (that is, with no entrained air) is plotted for temperatures between 20 C and 100 C. Each 20 C rise in temperature decreases the bulk modulus by approximately 100 MPa, and rises approximately 100 MPa for every 10 MPa increase in the static pressure. For a temperature change from 20 C to 45 C at a constant pressure of 5 MPa, which is a range expected for this work, the bulk modulus would drop by 7.8%. Likewise, at 40 C a pressure change from 2 MPa to 20 MPa would see the bulk modulus of the fluid rise by 10.7%. Ignoring the change in bulk modulus of the fluid as a function of temperature or pressure would result in an estimate of the total system stiffness that is in error by the same percentage.

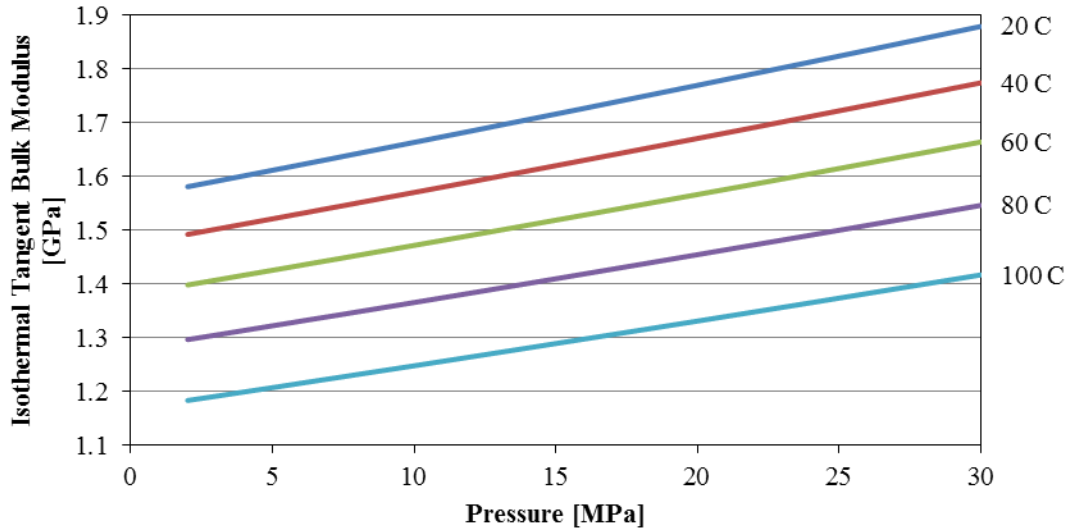


Figure 4-8: Isothermal tangent bulk modulus of hydraulic oil at temperatures from 20 C to 100 C.

#### 4.5.2 Entrained air

A standard equation for the volumetric fraction of air in hydraulic oil has been generally accepted, and is given by

$$X_0 = \frac{V_{g_0}}{V_{g_0} + V_{l_0}} \quad (3.37)$$

where  $X_0$  is the volumetric fraction of air in the air/liquid mixture,  $V_{g_0}$  and  $V_{l_0}$  are the volume of air and oil, where subscript  $0$  indicates standard temperature and pressure [63, 65]. Additionally,  $V_f = V_{g_0} + V_{l_0}$  is used to simplify the total fluid volume in later equations. While many models of the effective bulk modulus of air-infused hydraulic oil have been presented in the literature, Gholizadeh [63] found that three such models are effectively the same. The models considered vary slightly with respect to how they accounted for the volume fraction of air, or whether they were derived for the secant or tangent bulk modulus. When Gholizadeh re-derived the models in the literature using

identical assumptions, the same equation resulted for the bulk modulus of an air-oil mixture, that is

$$K_f = \frac{1 - X_0 + \left(\frac{p_0}{p}\right)^{\left(\frac{1}{n}\right)} X_0}{\frac{X_0}{np} \left(\frac{p_0}{p}\right)^{\left(\frac{1}{n}\right)} + \frac{1 - X_0}{K_o}} \quad (3.38)$$

where  $n$  is the polytropic constant for air ( $n = 1$  for an isothermal process,  $n = 1.4$  for an adiabatic process),  $p$  is the static pressure,  $p_0$  is atmospheric pressure, and  $K_o$  is the bulk modulus of the pure oil. It should be noted that this equation does not consider the means by which the oil and air are mixed, such that it does not matter if the air is a bubble or dispersed in the oil, nor does it account for the critical pressure where the air is fully dissolved in the oil. Figure 4-9 shows the isothermal tangent bulk modulus for hydraulic oil at 20 C for varying levels of entrained air, from 0% to 10%. The softening effect of the air is most dramatic at low pressures. For all volumetric fractions of air, as pressure increases the bulk modulus converges to that of the pure oil. As a point of reference, the static pressures considered this work are primarily from 2.1 MPa to 6.9 MPa, and for some tests up to 21 MPa.

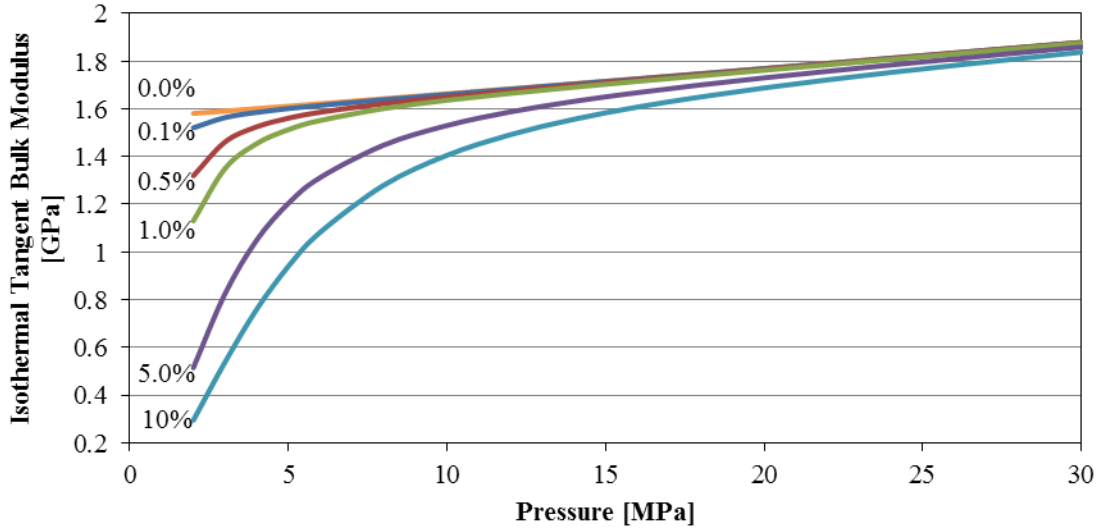


**Figure 4-9: Bulk modulus of hydraulic oil at 20 C with volumetric fractions of entrained air from 0.0% to 10%.**

#### 4.5.3 Structural compliance

Previously, in Section 4.3.1, an expression for the compliance of a cylindrical shell with internal pressure only was derived;

$$\frac{1}{\beta_s} = \frac{2}{E_s} \left( \frac{r_5^2 + r_4^2}{r_5^2 - r_4^2} + \nu_s \right). \quad (3.39)$$

It should be noted also that while the deformation of the shell is a function of pressure, the shell compliance is not.

For a cylindrical, carbon steel shell with an inner radius of  $r_4 = 31.75$  mm and an outer radius of  $r_5 = 44.45$  mm (these are the dimensions of a prototype Helmholtz resonator introduced in the next chapter), the bulk modulus of the shell using Equation (3.39) would be 31.0 GPa, which is 18 times greater than the bulk modulus of hydraulic fluid. For a shell of this inner diameter to have the same bulk modulus as hydraulic fluid, the thickness would have to be reduced from 12.7 mm to 0.72 mm. Further discussion of the effect of cavity compliance is presented in Section 4.5.4.

#### 4.5.4 Net effect

All sources of compliance in the cavity of a fluid power noise control device combine to lower the speed of sound within the device. The bulk modulus of the fluid with any entrained air, bulk modulus of the liner (if included), and the shell stiffness add as springs in series. The net bulk modulus is treated separately depending on the device. For a Helmholtz resonator, the net bulk modulus of the system is

$$\frac{1}{\beta_e} = \frac{1}{\beta_L} + \frac{1}{K_f} + \frac{1}{\beta_S} \quad (3.40)$$

where subscript  $e$  represents the effective stiffness of the system,  $f$  represents the air-oil mixture,  $L$  refers to the cavity compliance based on the liner (from Equation (3.20)), and  $S$  refers to the compliance of the shell.

As an example of the “net effect” of the system compliances, Figure 4-10 shows the bulk modulus of the shell, fluid, and total system with no liner present as the wall thickness of the shell is increased. The fluid in this example is the bulk modulus of pure mineral oil at 20 C and 20.7 MPa, a region where it is expected to be very stiff. For a cylindrical steel shell with an inner radius of  $r_4 = 31.75$  mm, an outer radius of  $r_5 = 44.45$  mm, and a length of 97.28 mm long (the dimensions of a prototype Helmholtz resonator introduced in the next chapter), filled with hydraulic oil with no entrained air, the effective stiffness of the system,  $\beta_e$ , is that of the fluid and shell acting in series, given by

$$\frac{1}{\beta_e} = \frac{1}{K_f} + \frac{1}{\beta_S} \quad (3.41)$$

where  $\beta_S$  is the shell stiffness from Equation (3.39). For increasingly thin-walled shells, the stiffness of the shell is low and thus dominates the effective stiffness, indicated by the effective stiffness approaching the shell stiffness curve asymptotically. Likewise, for

increasingly thick-walled shells, the effective stiffness approaches that of the fluid, since the shell is much stiffer and the fluid is the limiting factor. For the aforementioned case of a 12.7 mm thick wall, the fluid stiffness is 5.7% higher than the effective stiffness: thus, any estimate of the effective stiffness ignoring the shell stiffness would be in error by the same percentage. In any case, the effective stiffness is lower (alternately, the total system compliance is higher) than any single stiffness, and would continue to be the case as the compliances in the system change.

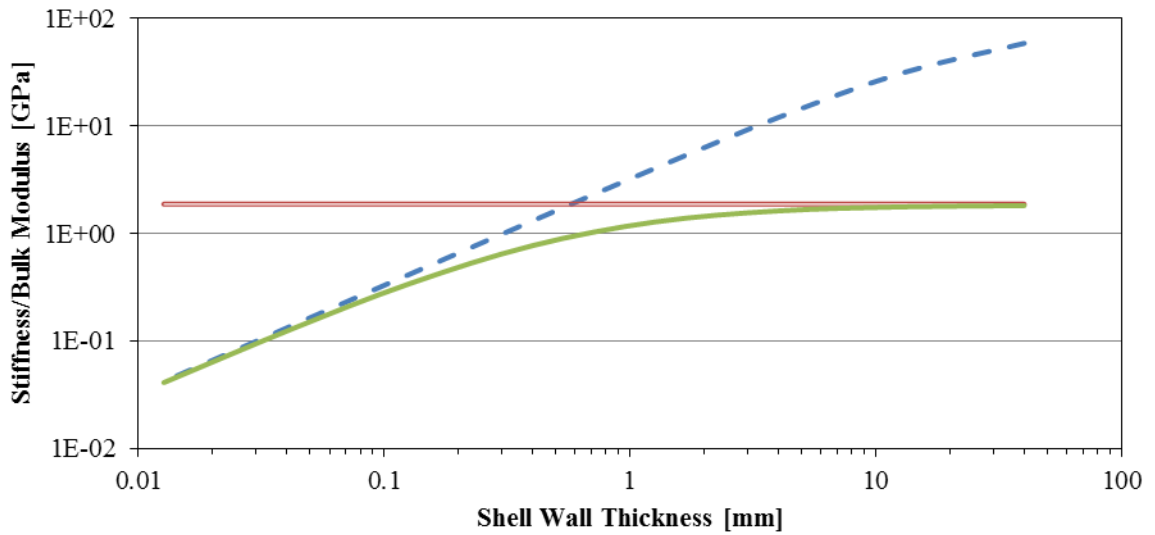


Figure 4-10: Stiffness of hydraulic oil-filled cylindrical cavity: — shell — fluid — total system.

## **CHAPTER 5**

### **EXPERIMENT**

This chapter will discuss the experimental measurement of transmission loss of the compliant-lined noise control devices for fluid power systems. First, a description of the liner materials that were studied is given along with their manufacturer-provided material properties. Then, a description of the devices tested along with drawings and dimensions follows. The experiment to estimate the deformation of the liner materials under pressure is described, along with the theory that is used to determine the compressed volume from the deformed inner radius. A brief theoretical background of transmission loss and the multi-point method of measurement is presented, followed by a detailed description of the equipment used to perform the experiments. Finally, the equations used to compute transmission loss and some implications are discussed.

#### **5.1 Liner Materials**

Both neat urethane compositions and syntactic foam liners were tested. The syntactic foams, also described as “voided” since the microspheres are hollow voids in the material, have the same host urethane as the neat compositions. The compositions were manufactured by Goodrich Inc., using microspheres manufactured by AkzoNobel. Four different syntactic foam compositions were tested, one of which has microspheres with a higher critical pressure: this liner is expected to be more compliant at pressures from 2.1-6.9 MPa. The mass fraction of the microspheres to host material is given by the manufacturer as 0.054:1. Additionally, three liners without microspheres with the same composition as the host matrix of the syntactic foam liners were tested to provide a

reference to the performance without the effect of the microspheres. Table 3 outlines the properties of the liners tested; included are values that characterize a viscoelastic material, such as the peak value of the  $\tan \delta$  and its frequency. The liner IDs with a trailing three-digit number are the voided liners, where the trailing number is the design density in g/L. The data provided by the manufacturer for each composition was given at three temperatures: 20, 35, and 45 C, all at atmospheric pressure. Material properties at elevated pressures are not available from the manufacturer. Likewise, information about the Poisson's ratio of the materials is similarly limited – the Poisson's ratios provided are 0.45 for the voided liners and 0.4995 for the unvoided liners. The dimensions of the liners tested are provided in Table 4.

**Table 3: Liner properties.**

| Liner ID       | Low-Frequency Bulk Modulus [Pa] | Peak $\tan \delta$ [ND] | Frequency [Hz] of $T_g$ at: |          |          |
|----------------|---------------------------------|-------------------------|-----------------------------|----------|----------|
|                |                                 |                         | 20 C                        | 35 C     | 45 C     |
| GR9            | 2.49E+09                        | 0.81                    | 6.76E+04                    | 1.00E+07 | 1.00E+08 |
| GR9-625        | 3.49E+07                        | 0.47                    | 9.36E+04                    | 5.97E+05 | 1.63E+06 |
| GR23           | 1.25E+09                        | 1.10                    | 1.97E+02                    | 5.59E+03 | 3.13E+04 |
| GR23-633       | 2.65E+07                        | 0.60                    | 4.09E+02                    | 1.25E+04 | 7.38E+04 |
| HRPG15(12)     | 1.29E+09                        | 1.24                    | 2.20E+00                    | 2.78E+02 | 2.65E+03 |
| HRPG15(12)-545 | 2.46E+07                        | 0.67                    | 1.25E+00                    | 2.15E+02 | 2.32E+03 |
| GR23 461-663   | 3.47E+07                        | 0.58                    | 5.00E+02                    | 2.38E+04 | 1.97E+05 |

**Table 4: Liner dimensions.**

| Liner ID       | Mass [g] | Length [m] | Inner radius [mm] | Outer radius [mm] | Volume [cm <sup>3</sup> ] | Density [kg/m <sup>3</sup> ] |
|----------------|----------|------------|-------------------|-------------------|---------------------------|------------------------------|
| GR9            | 263.9    | 95.60      | 13.52             | 31.91             | 250.9                     | 1051.7                       |
| GR9-625        | 149.9    | 95.27      | 13.48             | 31.33             | 239.4                     | 626.3                        |
| GR23           | 260.8    | 94.56      | 13.83             | 31.40             | 236.0                     | 1105.0                       |
| GR23-663       | 152.3    | 95.13      | 13.59             | 31.25             | 236.6                     | 643.7                        |
| HRPG15(12)     | 269.1    | 95.24      | 13.82             | 31.35             | 236.9                     | 1135.8                       |
| HRPG15(12)-545 | 131.7    | 95.51      | 13.55             | 31.48             | 242.2                     | 543.7                        |

The microspheres in each of the voided samples in Table 3 except GR23 461-663 are AkzoNobel Expancel 091 DE 80 d30 – these are 80  $\mu\text{m}$  diameter microspheres with a 30  $\text{kg}/\text{m}^3$  density. The microsphere properties are summarized in Table 5. According to Equation (2.5), assuming the spheres are polystyrene, they have a critical pressure of

approximately 92 kPa. The liner designed with a higher critical pressure was formed with Expancel 461 DET 20 d70 microspheres and the GR23 host matrix. This liner is identified as GR23 461-663. Based on a wall thickness estimate from a theoretical microsphere expansion worksheet provided by AkzoNobel [66], it has a critical buckling pressure of approximately 853 kPa, or an order of magnitude higher than the other three voided liners.

**Table 5: Microsphere properties.**

| Microsphere ID | Mean Diameter<br>[ $\mu\text{m}$ ] | Est. Wall<br>Thickness [ $\mu\text{m}$ ] | Density<br>[ $\text{kg}/\text{m}^3$ ] | Est. Buckling<br>Pressure [kPa] |
|----------------|------------------------------------|--|---------------------------------------|---------------------------------|
| 091 DE 80 d30  | 80                                 | 0.2                                      | 30                                    | 92.09                           |
| 461 DET 20 d70 | 20                                 | 0.14                                     | 70                                    | 853.0                           |

The three syntactic foams with low-critical buckling pressure microspheres are designed to explore the effect of the different parameters that characterize the material. These parameters are the low-frequency bulk modulus and the peak value and frequency of the  $\tan \delta$  for given temperatures. For brevity, herein the term “bulk modulus” will refer only to the real part of the complex bulk modulus. The  $\tan \delta$  represents the lossiness of the material, and its peak value occurs at the glass transition temperature  $T_g$ . This value separates the “rubbery” and “glassy” phases of the material, and is temperature and frequency dependent, such that it shifts approximately a factor of ten higher in frequency for every 10 C increase in temperature. Liner HRP15(12)-545 has the lowest low-frequency bulk modulus, but has its  $T_g$  at the lowest frequency by more than two orders of magnitude. Figure 5-1 shows the bulk modulus for this and two other liners: GR9-625 and GR23-633, to illustrate the difference in the low-frequency behavior. Additionally, Figure 5-2 shows the  $\tan \delta$  value for the same three liners. On both plots, a frequency range of interest of approximately 10-1500 Hz is indicated, as both plots span 12 orders

of magnitude in frequency. The low-frequency bulk modulus of liner GR23-633 is similar to that of HRPG15(12)-545, only 7% higher, but it has its  $\tan \delta$  at a much higher frequency. For example, HRPG15(12)-545 will have a much higher bulk modulus at the  $T_g$  than GR23-633 near 230 Hz. This frequency is significant as it is the fundamental frequency of a typical axial piston pump driven at 1500 RPM. Liner GR9-625 has a higher low-frequency bulk modulus, but also has its  $T_g$  at even higher frequencies, and has the lowest  $\tan \delta$  near 230 Hz. With this liner, the  $\tan \delta$  peak occurs at far higher frequencies than the range considered so the losses observed in the system should theoretically only come from the motion of the fluid.

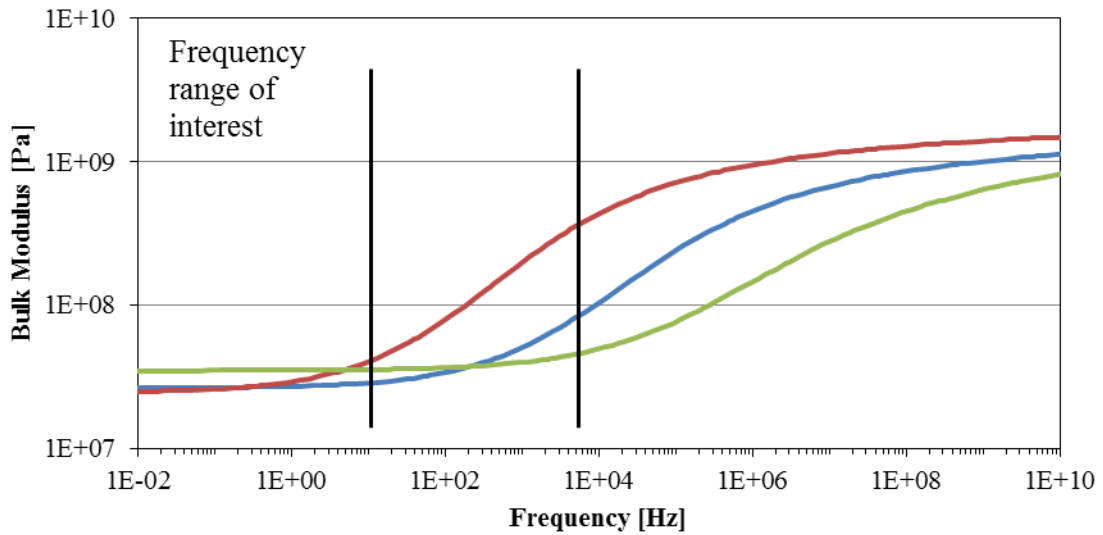


**Figure 5-1: Bulk modulus of liners at 35 C and atmospheric pressure, — HRPG15(12)-545, — GR23-633, — GR9-625.**

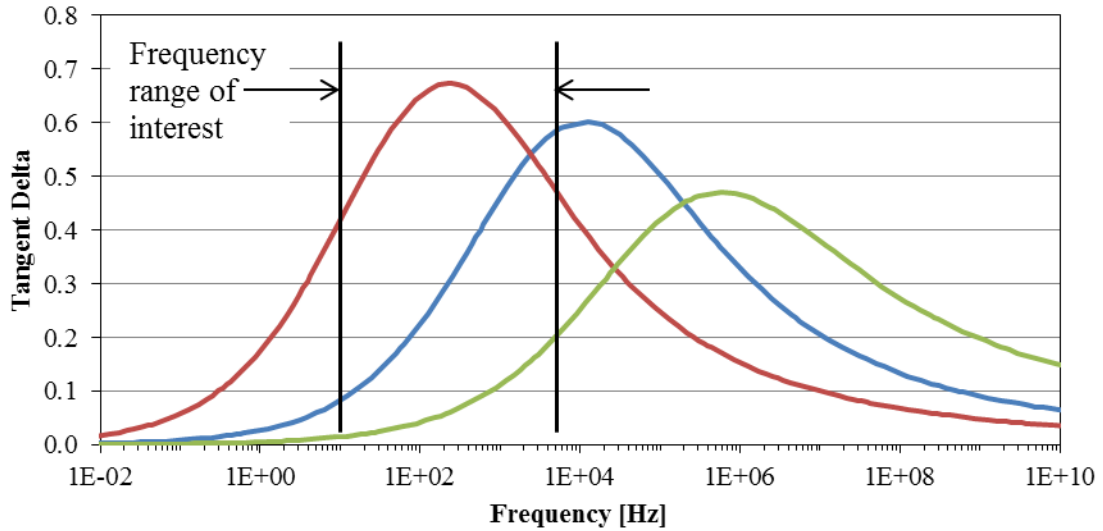


Figure 5-2: Tan delta of liners at 35 C and atmospheric pressure, — HRP15(12)-545, — GR23-633, — GR9-625.

## 5.2 Devices

This section will present a schematic of each of the two noise control devices tested, and list the appropriate dimensions. The listed radii are numbered such to be consistent with the numbering scheme presented in Figure 4-1 and Table 1.

### 5.2.1 Helmholtz Resonator

The Helmholtz resonator tested was constructed per the schematic in Figure 5-3, and a photograph of the prototype device is shown in Figure 5-4. The relevant dimensions, at atmospheric pressure, are listed in Table 6, with all units given in millimeters. Since there is no annulus in the resonator, radii  $r_1$  and  $r_2$  are not given. The dimensions of the liner are approximate as each liner varies in size slightly because of manufacturing variability.

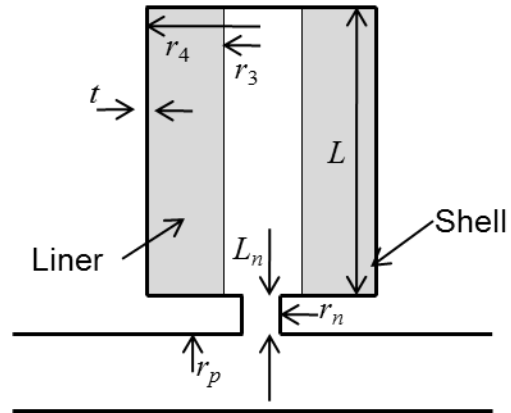


Figure 5-3: Schematic of Helmholtz resonator with dimensions.

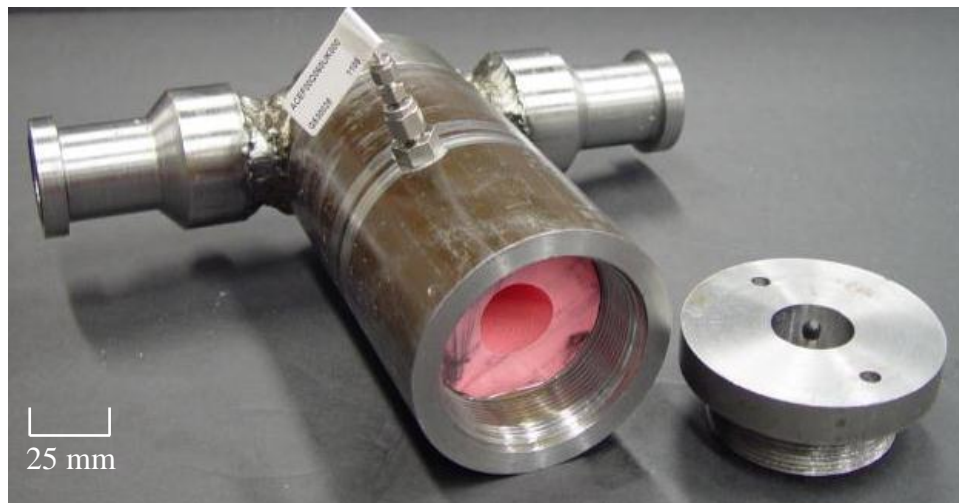


Figure 5-4: Photograph of the Helmholtz resonator prototype with the end cap removed.

Table 6: Helmholtz resonator dimensions.

| Dimension | Value [mm] | Description           |
|-----------|------------|-----------------------|
| $L$       | 96.52      | Length of liner       |
| $L_n$     | 37.34      | Length of neck        |
| $r_3$     | 13.33      | Inner radius of liner |
| $r_4$     | 31.75      | Outer radius of liner |
| $r_5$     | 31.75      | Inner radius of shell |
| $r_6$     | 44.45      | Outer radius of shell |
| $r_n$     | 2.97       | Radius of neck        |
| $r_p$     | 10.31      | Radius of pipe        |
| $t$       | 12.70      | Thickness of shell    |

### 5.2.2 Tuning Coil

The tuning coil tested was constructed per the schematic in Figure 5-5. A photograph of the prototype with one endcap removed and the liner and annulus partially extracted is shown in Figure 5-6. The relevant dimensions are given in Table 7. The washer and spring serve to keep the liner against the upstream face of the shell as it shrinks under pressure. The deformation at elevated pressure also forms a larger gap between the liner and shell than can be seen here, which forms the branch of the device. When the device is assembled at atmospheric pressure, the spring is fully compressed: as the pressure increases, the length of the liner shrinks and the spring elongates. The annulus is sized such that the outer radius is slightly smaller than the inner radius of the liner at 21 MPa. This is to ensure that for all of the pressures considered the liner remains in a state of hydrostatic compression and is not constrained on the annulus to maximize the waveguide compliance as discussed in Section 4.4.4.

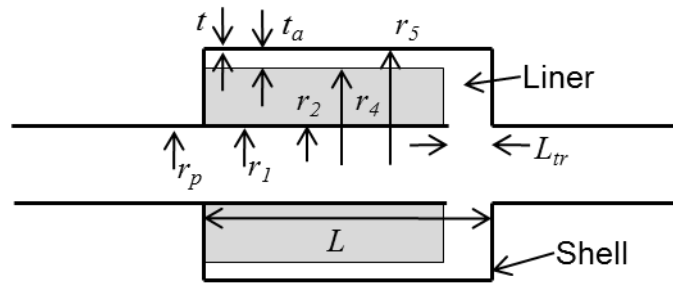
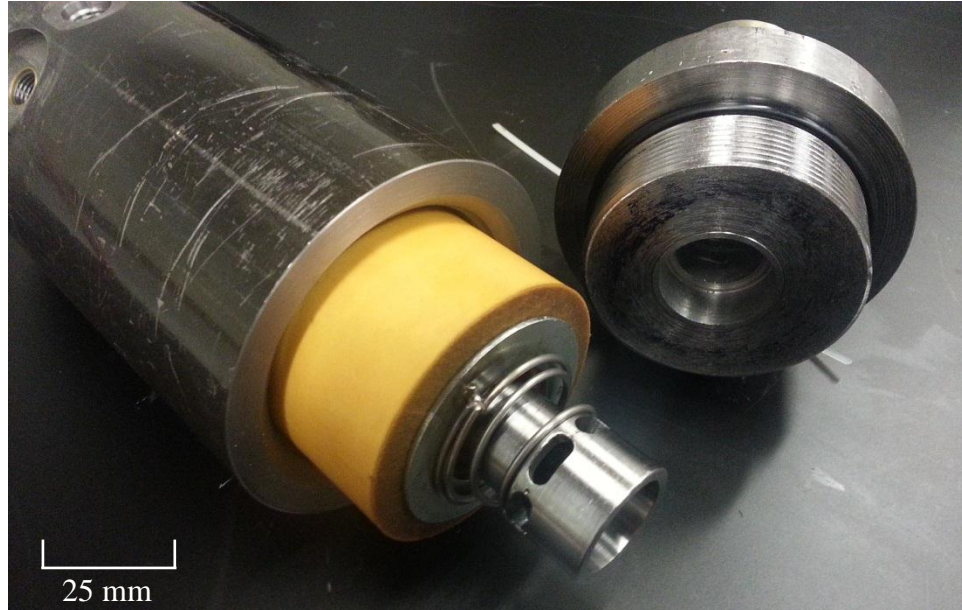


Figure 5-5: Schematic of tuning coil with dimensions



**Figure 5-6: Photograph of tuning coil prototype with one end cap removed and the liner and annulus partially extracted.**

**Table 7: Tuning coil dimensions**

| Dimension | Value [mm] | Description              |
|-----------|------------|--------------------------|
| $L_l$     | 96.52      | Length of liner          |
| $L$       | 104.1      | Internal length of shell |
| $L_{tr}$  | 4.78       | Length of throat         |
| $r_1$     | 9.33       | Inner radius of annulus  |
| $r_2$     | 10.60      | Outer radius of annulus  |
| $r_3$     | 13.33      | Inner radius of liner    |
| $r_4$     | 31.75      | Outer radius of liner    |
| $r_5$     | 31.75      | Inner radius of shell    |
| $r_6$     | 44.45      | Outer radius of shell    |
| $r_p$     | 10.31      | Radius of pipe           |
| $t$       | 12.70      | Thickness of shell       |

### 5.3 Liner Deformation

Since the material properties of the liners at elevated pressures are unknown from the manufacturer, an estimate of the deformation of the liners at these conditions is needed. A test fixture was constructed to estimate the radial compression of each liner as a function of pressure, such that the geometry of the liner (inner radius, outer radius, length and volume) could be included in a theoretical model for each noise control device. The test fixture is composed of a rigid shell, an 18-mm thick, 40-mm diameter

Metaglas (borosilicate) sight glass, and a collar to hold the sight glass onto the shell. The fixture was installed in a hydraulic circuit as a side-branch, similar to how a Helmholtz resonator would be installed, and a digital camera was used to take pictures of the liner under compression at different pressures. A photograph of the test fixture is shown as Figure 5-7. The photographs of the liners under pressure were analyzed to estimate the inner radius of the liner at each pressure. The inner radius decreases as pressure increases for all liners except HRP15(12) – this liner was cast in a different mold than the rest and has a slightly larger outer diameter such that it is press-fit into the shell. Thus, HRP15(12) is under internal pressure and not hydrostatic pressure. The rest of the liners are slip-fit and exposed to pressure on all sides. Using information about the inner radius as a function of pressure, the outer radius and length can be estimated using the equations given in Section 4.2. The observed inner radii for each liner at each pressure are listed in Table 8, and some examples are shown graphically in Figure 5-8. None of the unvoided liners compress appreciably. Of particular interest for the voided liners is the behavior from 0 – 2.1 MPa: for all except the high-pressure liner (GR23 461-663), the inner radius displaces drastically between 0 and 0.7 MPa, and after 2.1 MPa it is approximately linear with pressure. This range encompasses the critical pressure, and demonstrates how drastically the volume changes as a result of the microspheres within the material collapsing. For the low-pressure liner, this transformation occurs entirely below 0.7 MPa. The high-pressure liner, GR23 461-663, uses microspheres with a higher critical pressure and thus the displacement of the inner radius does not drastically change until between 0.7 and 1.4 MPa – consistent with the estimated critical pressure for this liner.

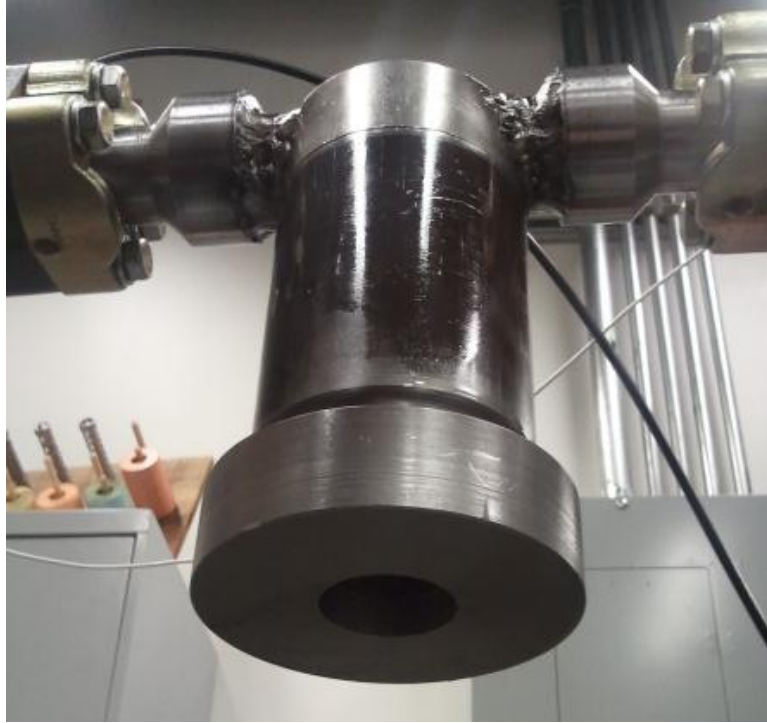


**Figure 5-7: Test fixture for measuring liner compression.**

**Table 8: Inner radius of each liner as a function of pressure (in mm).**

| Pressure<br>[MPa] | GR9     | GR9-625 | GR23    | GR23-633 | HRPG15(12) | HRPG15(12)-545 | GR23 461-663 |
|-------------------|---------|---------|---------|----------|------------|----------------|--------------|
| 0.0               | 13.7380 | 13.1318 | 13.6611 | 13.0249  | 12.9449    | 13.2538        | 12.8045      |
| 0.7               | 13.8113 | 11.9313 | 13.8242 | 11.3316  | 12.9267    | 11.6228        | 12.6960      |
| 1.4               | 13.7929 | 11.4696 | 13.8061 | 11.6294  | 12.9449    | 10.8355        | 12.0449      |
| 2.1               | 13.7380 | 11.6912 | 13.7155 | 11.4805  | 12.9449    | 11.4354        | 11.7917      |
| 2.8               | 13.7380 | 11.5435 | 13.8061 | 11.3130  | 12.9815    | 11.2666        | 11.7194      |
| 3.4               | 13.6098 | 11.2664 | 13.7336 | 11.2200  | 12.9998    | 11.3604        | 11.6109      |
| 4.1               | 13.7380 | 11.3772 | 13.6430 | 11.0898  | 12.9632    | 11.2479        | 11.5747      |
| 4.8               | 13.8662 | 11.2295 | 13.8242 | 11.1642  | 12.9815    | 11.3791        | 11.5566      |
| 5.5               | 13.7380 | 11.2110 | 13.7517 | 11.1270  | 12.9998    | 11.3041        | 11.5204      |
| 6.2               | 13.7380 | 11.2110 | 13.8242 | 11.0153  | 12.9998    | 11.3604        | 11.5566      |
| 6.9               | 13.8845 | 11.1187 | 13.7155 | 11.1642  | 12.9632    | 11.2666        | 11.5385      |
| 8.3               | 13.7929 | 11.0817 | 13.7880 | 11.0153  | 13.1095    | 11.2666        | 11.3577      |
| 9.7               | 13.7380 | 11.0632 | 13.8785 | 11.1642  | 12.9815    | 11.1917        | 11.5204      |
| 11.0              | 13.7380 | 11.0632 | 13.7155 | 11.0153  | 13.0912    | 11.1917        | 11.5747      |
| 12.4              | 13.7380 | 11.0448 | 13.6249 | 11.1642  | 13.0912    | 11.1729        | 11.2672      |
| 13.8              | 13.7380 | 11.0448 | 13.7880 | 11.0153  | 13.0912    | 11.1354        | 11.5204      |

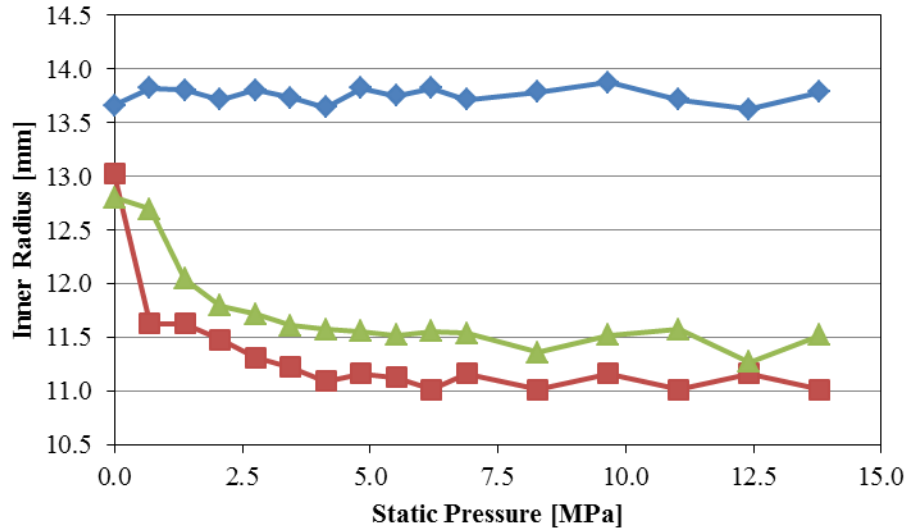


Figure 5-8: Inner radius of liner as a function of static pressure for three liners: ♦ GR23 (unvoided), ■ GR23-633 (voided), ▲ GR23 461-663 (voided).

#### 5.4 Measurement and analysis of transmission loss

One common means of quantifying the performance of noise control devices is a metric called transmission loss ( $TL$ ). This metric, when calculated properly, is a device-specific performance metric, in contrast to system-specific metrics such as Insertion Loss ( $IL$ ), and is thus useful for comparing devices independent of a system. The transmission loss of a noise control device is defined as the ratio of incident to transmitted acoustic power,  $W_{u,i}$  and  $W_{d,t}$ , and is written as

$$TL = 10 \log_{10} \frac{W_{u,i}}{W_{d,t}} \quad (4.1)$$

where subscripts  $u$  and  $d$  refer to the upstream and downstream sides of the device, relative to the source of the acoustic power. Since Equation (4.1) refers to incident and transmitted power, not simply total power, the wave field up- and downstream of the device must be resolved into its forward- and reverse-traveling components in order to compute the transmission loss of a device. Consider a noise control component under

test, connected to rigid pipes at either end with an unknown termination impedance, as shown in Figure 5-9. The termination impedance reflects some of the energy from wave  $D$  as wave  $E$  back toward the device. The two-mic method [5, 67, 68], and an extension of which is the three-mic (or multi-point) method [2, 3, 69-71] have been developed in the literature to resolve the wave fields in each test section. Each technique utilizes a set of microphones or, for hydraulic systems, dynamic pressure sensors, and optionally transfer functions, to determine the resolved wave field in the up- and downstream sections. Knowledge of the wave field can then determine the transmission loss of the device. The test method implemented in this work is the multi-point method, which uses three pressure transducers in both sections, located at  $x_3$ - $x_1$  and  $y_1$ - $y_3$  in Figure 5-9. The advantage of the multi-point method is the elimination of the half-wavelength indeterminacy introduced at a frequency where the transducer spacing is equal to half the wavelength [3], since a least-squares routine fits the measured transfer functions to a theoretical wave propagation model. The resolved wave amplitudes are then used to determine the total acoustic pressure and velocity at the ports, and thus the transmission loss.

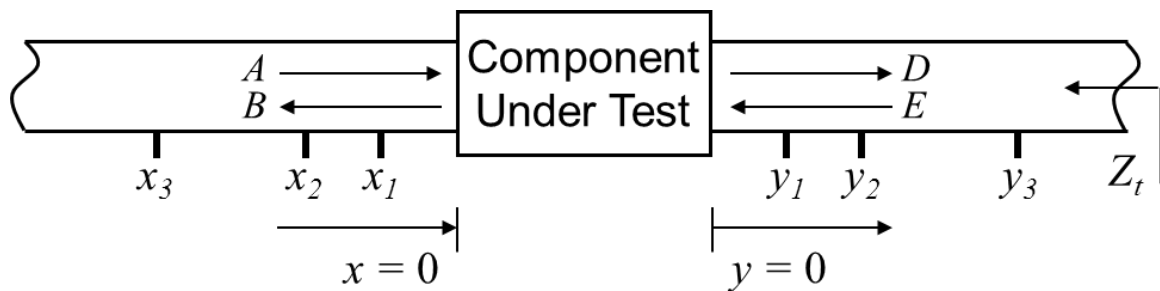


**Figure 5-9: Schematic of a noise control device under test.**

The calculation of  $TL$  requires decomposing the wave field in each up- and downstream section, then solving an over-determined system of equations for the

complex wave amplitudes using experimentally-measured transfer functions. The wave field in each section is decomposed into forward- and reverse-traveling waves

$$\begin{aligned} P_u &= Ae^{-\gamma x} + Be^{\gamma x} & P_d &= De^{-\gamma x} + Ee^{\gamma x} \\ Q_u &= \frac{Ae^{-\gamma x} - Be^{\gamma x}}{Z_0} & Q_d &= \frac{De^{-\gamma x} - Ee^{\gamma x}}{Z_0} \end{aligned} \quad (4.2)$$

where  $A$ ,  $B$ ,  $C$ , and  $D$  are complex acoustic pressures,

$$Z_0 = \frac{\rho c}{\pi r_p^2} \xi \quad (4.3)$$

is the acoustic impedance,  $\rho$  and  $c$  are the density and speed of sound of the fluid,  $r_p$  is the radius of the pipe and

$$\gamma = j \frac{\omega}{c} \xi \quad (4.4)$$

is the complex wavenumber, where the viscous effects are given by the approximation [5]

$$\xi = 1 + \sqrt{\frac{\nu}{j\omega r_p^2} + \frac{\nu}{j\omega r_p^2}} \quad (4.5)$$

where  $\nu$  is the kinematic viscosity of the fluid. Transfer functions  $H_{ij}$  are measured among the sensors and assembled into a vector

$$b = \begin{pmatrix} H_{x3,x2} \\ 1 \\ H_{x1,x2} \\ H_{y1,x2} \\ H_{y2,x2} \\ H_{y3,x2} \end{pmatrix} \quad (4.6)$$

where the sensor at location  $x_2$  is the reference for all  $H_{ij}$  – hence, the transfer function of sensor  $x_2$  relative to itself is unity. The theoretical propagation of the waves in each section are separated into sectors of matrix  $G$  and vector  $X$ , with respect to the pressure at sensor  $x_2$ , which is the reference sensor for each of the transfer functions:

$$G = \begin{bmatrix} \exp(-\gamma x_3) & \exp(\gamma x_3) & 0 & 0 \\ \exp(-\gamma x_2) & \exp(\gamma x_2) & 0 & 0 \\ \exp(-\gamma x_1) & \exp(\gamma x_1) & 0 & 0 \\ 0 & 0 & \exp(-\gamma y_1) & \exp(\gamma y_1) \\ 0 & 0 & \exp(-\gamma y_2) & \exp(\gamma y_2) \\ 0 & 0 & \exp(-\gamma y_3) & \exp(\gamma y_3) \end{bmatrix} \quad (4.7)$$

$$X = \begin{pmatrix} A/P_2 \\ B/P_2 \\ D/P_2 \\ E/P_2 \end{pmatrix} \quad (4.8)$$

The wave amplitudes are then solved, still with respect to the pressure at sensor  $x_2$ , by the Moore-Penrose pseudoinverse:

$$X = G^+ b \quad (4.9)$$

which performs a least-squares fit of the measured transfer functions to the theoretical propagation model. At this point, all four wave amplitudes relative to a single complex pressure are known: what remains is to compute the transmission loss from these values.

The transmission loss can be calculated from the elements of the transfer matrix for the device. The transfer matrix is a common means of representing the acoustic properties of a device, such as the acoustic pressure and velocity at the ports of a two-port, four-pole system,

$$\begin{pmatrix} P_u \\ Q_u \end{pmatrix} = \begin{bmatrix} t_{11} & t_{12} \\ t_{21} & t_{22} \end{bmatrix} \begin{pmatrix} P_d \\ Q_d \end{pmatrix} \quad (4.10)$$

where subscripts  $u$  and  $d$  again indicate the upstream and downstream ports. The elements of the transfer matrix,  $t_{ij}$ , can be derived from Equation (4.10) as:

$$\begin{aligned}
t_{11} &= \frac{P_d Q_d + P_u Q_u}{P_u Q_u + P_d Q_d} & t_{12} &= \frac{P_u^2 - P_d^2}{P_u Q_u + P_d Q_d} \\
t_{21} &= \frac{Q_u^2 - Q_d^2}{P_u Q_u + P_d Q_d} & t_{22} &= \frac{P_d Q_d + P_u Q_u}{P_u Q_u + P_d Q_d}
\end{aligned} \tag{4.11}$$

If the device under consideration can be assumed to be symmetric and reciprocal, the determinant of the transfer matrix is unity [20],

$$t_{11}t_{22} - t_{12}t_{21} = 1 \tag{4.12}$$

and  $t_{11} = t_{22}$ . An expression for the transmission loss of a two-port device, given an anechoic termination, can be derived from Equations (4.10), assuming an anechoic termination, as

$$TL = 20 \log_{10} \left| \frac{1}{2} \left( t_{11} + \frac{t_{12}}{Z_0} + Z_0 t_{21} + t_{22} \right) \right| \tag{4.13}$$

although an anechoic termination is not required to calculate  $TL$ , given that the wave fields up- and downstream of the system are fully resolved. If the wave field is decomposed per Figure 5-9, the upstream and downstream pressure and velocity can be resolved as:

$$\begin{aligned}
P_u &= A + B & P_d &= D + E \\
Q_u &= \frac{A - B}{Z_0} & Q_d &= \frac{D - E}{Z_0}
\end{aligned} \tag{4.14}$$

Equations (4.14) can be substituted into Equations (4.11) and then into Equation (4.13), which after simplification yields

$$TL = 20 \log_{10} \left| \frac{A^2 - E^2}{AD - BE} \right| \tag{4.15}$$

Equation (4.15) accounts for the existence of a reverse-traveling wave downstream of the system under test (wave  $E$ ). Due to the long acoustic wavelengths in hydraulic fluid,

especially relative to the length of the pipe section immediately downstream of the device under test, this term cannot be ignored. However, if there existed an anechoic termination (or equivalently, an infinitely long pipe) wave amplitude  $E$  would vanish and Equation (4.15) would become

$$TL = 20 \log_{10} \left| \frac{A}{D} \right| \quad (4.16)$$

which is the more familiar form of the transmission loss equation.

## 5.5 Test Rig

A test rig was constructed per the schematic in Figure 5-10 using the guidelines set forth by a set of ISO standards, ISO-15096, parts -1 through -3 [72-74], which have been established for the purposes of measuring the speed of sound of fluid in a pipe, the impedance of a pump, and the transmission loss of a two-port device. Specifically, the pipes that comprise the test sections in the test rig were constructed to the dimensions listed in part two of the standard, which describes the measurement of the speed of sound in a rigid pipe. The inner radius of the pipes is such that only plane waves may propagate: the cut-on frequency for the first radial mode is 43 kHz, which is much higher than the frequency range of interest (5 kHz). The pump is a Sauer Danfoss H1 bidirectional 9-piston axial piston pump, driven by a Siemens 60 HP variable-speed ac motor. A Siemens Simovert Masterdrive variable-frequency drive powers the motor. The drive frequency and pump displacement are set and controlled using xPC-Target over a CAN-bus interface. Six high-bandwidth piezoelectric pressure transducers, PCB model 101A06, are connected to two signal conditioners, PCB model 480B21 and 482A16. The analog signals from the signal conditioners are then digitized by a 24-bit, 8-channel National

Instruments data acquisition board, model 4472. Temperatures are measured with type K thermocouples, sensing the oil temperature at the entrance of the rig and at the inner radius of the component under test. The thermocouples were calibrated with an Omega CL3512A thermocouple calibrator and are read by a National Instruments 9211A thermocouple reader. The “termination silencer” is a commercially-available hydraulic noise suppressor, manufactured by Wilkes and McLean, model WM-5081. This suppressor uses a pressurized nitrogen bladder to introduce compliance within the device, and is charged to approximately half the system pressure.

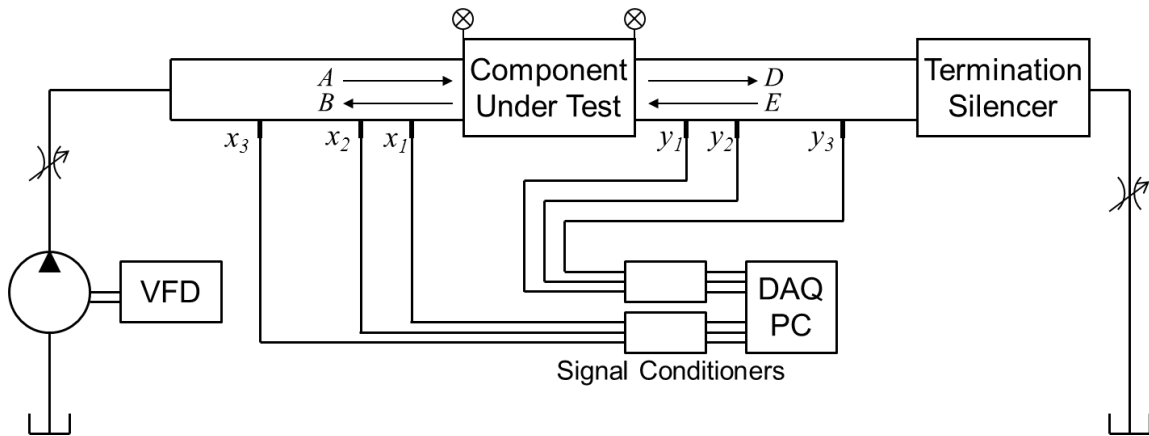


**Figure 5-10: Schematic of the hydraulic test rig.**

### 5.5.1 Calibration

The piezoelectric transducers do not have perfect amplitude or phase response. Therefore, some type of calibration is necessary to correct for this inherent variation. Since the error in these transducers varies frequency-by-frequency, it is necessary to perform frequency-by-frequency calibration of the measured transfer functions with their calibrated values. Transfer functions are used in the calculation of  $TL$ , as discussed in Section 5.4, so only relative calibration of the sensors is necessary. The calibration values are obtained by mounting four sensors at a time in a calibration block, shown in Figure

5-11, which is mounted at the end of a side branch off the main flow path of the test rig. Since the sensors are mounted circumferentially, and only plane waves may propagate in the calibration block, each sensor is exposed to the same acoustic pressure. Transfer functions among the sensors are obtained identical to those obtained when installed in the test rig. When post-processing the experimental data, the transfer functions are calibrated by the method in the standard ISO 15086-2 [73],

$$H_{ij}|_{calibrated} = \frac{H_{ij}|_{measured}}{H_{ij}|_{calibration}}, \quad (4.17)$$

where the measured transfer functions, from an experiment, are divided by the calibration transfer functions associated with the appropriate pair of sensors to obtain the calibrated values.



**Figure 5-11: Picture of calibration block with three sensors installed.**

### 5.5.2 Coherence

An indicator of a successful transfer function measurement is the coherence. The coherence is an indication of the correlation of the signals from two sensors. A coherence

value of unity means the power in each signal is linearly related and correlated. Likewise, a coherence of zero indicates that the signals are either not linearly related or uncorrelated. The coherence is given by

$$C_{xy} = \frac{|G_{xy}|^2}{G_{xx} G_{yy}} \quad (4.18)$$

where  $G_{xy}$  is the cross-spectral density between  $x$  and  $y$ , and  $G_{xx}$  and  $G_{yy}$  are the respective autospectral densities. With respect to the measurement of transfer functions in the experimental set-up as discussed, a low coherence indicates that noise has entered the measurement since the acoustic propagation in hydraulic oil is strongly linear. Typically, for the transfer functions to be considered valid, the coherence must be at least 0.9. Frequencies where the coherence does not satisfy this requirement would then not be included in the transmission loss computation. For the measurement of  $TL$  for Helmholtz resonators, it has been found experimentally that coherence values as low as 0.6 near the resonance frequency are acceptable as long as the measurements are repeatable and the data is smooth. In this case, there may be noise or nonlinearities that are contaminating the measurement near the resonance that are strong enough to reduce the coherence but not strong enough to affect the calculation of  $TL$ . This is especially critical for transfer functions that relate the pressure on different sides of the device under test – one, because the device can reduce the acoustic energy sufficiently to lower the coherence, and two, because without isolation of the downstream wave field noise generated downstream of the test rig can contaminate the measurement. Such is the reason for inclusion of the hydraulic suppressor at the downstream end of the test rig, shown as “termination silencer” in Figure 5-10 – preventing noise generated by the restricting needle valve

downstream from contaminating the wave field, affecting the transfer functions across the device.

## CHAPTER 6

### HELMHOLTZ RESONATOR

In this chapter, a theoretical, lumped-element model for a Helmholtz resonator is derived, which includes the effect of a solid, compliant liner in the cavity. A brief parameter study explores the effect of the liner on the resonance frequency and damping. Then, the results from experimental tests of a prototype, compliant-lined Helmholtz resonator are discussed. The theoretical model is fit to experimental results within a least-squares routine to estimate the complex bulk modulus of the liners. The effects of temperature and pressure on the performance are explored, and compared to expected trends.

#### 6.1 Modeling

The Helmholtz resonator can be most simply described as the acoustic analogue of a resistor-inductor-capacitor (RLC) circuit. In the long wavelength limit (typically where the longest characteristic dimension is less than  $1/16^{\text{th}}$  of a wavelength [75]) the behavior of the resonator can be broken down into simple lumped elements, as, acoustically, the interior acts in bulk. The development of the lumped-element model generally follows the derivation given in Kinsler, Frey, et al. [76] Figure 6-1 is a schematic of a Helmholtz resonator with a compliant lining, with resolved incident and transmitted waves and relevant dimensions. The dimensions of the Helmholtz resonator, such as the radii for the liner and shell, follow the same numbering scheme introduced in Figure 4-1 and Table 1. Figure 6-2 indicates an analogous electric circuit model. The lumped parameter, acoustic impedance of the resonator is given by

$$Z_H = R + j \left( \omega L - \frac{1}{\omega C} \right) \quad (5.1)$$

where  $R$ ,  $L$ , and  $C$  are the equivalent acoustic resistance, inertance, and compliance, and  $\omega$  is the radian frequency. The electrical analogy is depicted in Figure 6-2a) and b). Figure 6-2a) depicts the impedance of a resonator in a transmission line (or, in the case of hydraulics, a pipeline), where  $Z_L$  is a load impedance downstream of the device, and  $V$  and  $I$  are the electrical analogy of the acoustic pressure and velocity. Figure 6-2b) is the circuit analogy for the resonator itself.

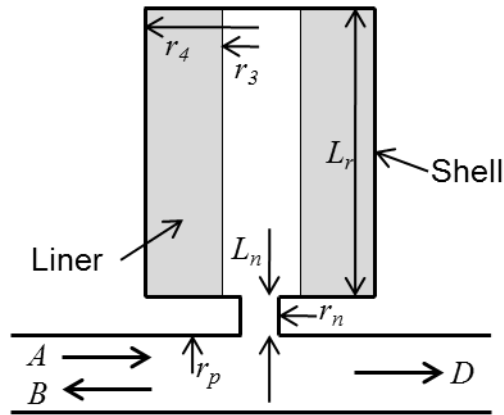


Figure 6-1: Helmholtz resonator with compliant lining.

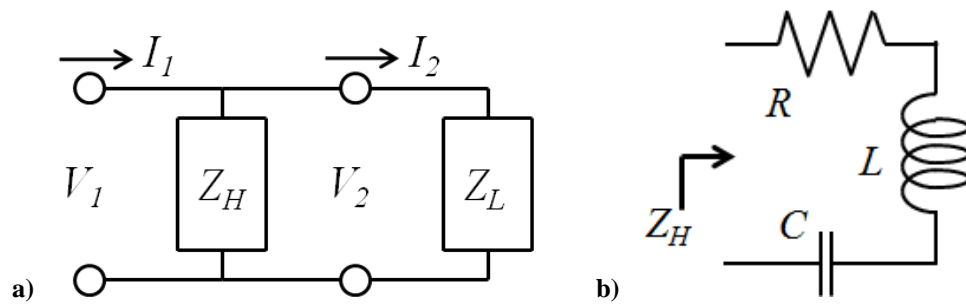


Figure 6-2a): Transmission line analogy with Helmholtz resonator and load impedance b) Circuit analogy of Helmholtz resonator.

The resonance frequency of the Helmholtz resonator occurs when the reactance  $\omega L - 1/\omega C$  in Equation (5.1) goes to zero. The compliance of the cavity is the inverse of the effective stiffness, which has contributions from the bulk modulus of both the fluid

and liner. It is necessary, then, to find the compliance of the resonator considering the volume and bulk modulus of both media. Solving for the compliance,  $C$ , from Equation (5.1), gives

$$C = \frac{1}{\omega_r^2 L} \quad (5.2)$$

where  $\omega_r$  is the resonance frequency and  $L$  is the inertance. Rearranging Equation (5.2) results in an equation for the resonance frequency of the device given an inertance and compliance,

$$\omega_r = \frac{1}{\sqrt{LC}} \quad (5.3)$$

which reveals that higher compliance will result in lower resonance frequencies. The compliance, along with how it is modified by a compliant liner, will be treated in more detail later in this section. The remaining physical quantities are discussed first, such as the inertance,  $L$ , which is given by

$$L = m/S_n^2 \quad (5.4)$$

where  $m$  is the mass of fluid in the neck and  $S_n$  is the cross-sectional area of the neck. The mass  $m$  is a function of the density of the fluid and the cross-sectional area and effective length of the neck,

$$m = \rho_f S_n L'_n \quad (5.5)$$

where the length of the neck is corrected to include acoustic radiation loading by

$$L'_n = L_n + 1.7r_n. \quad (5.6)$$

At this point in the development of the model, the volume of the resonator is assumed to be encapsulated by a rigid shell and filled only with fluid. The bulk modulus of the fluid is related to the speed of sound by

$$K_f = \rho_f c^2. \quad (5.7)$$

The effective stiffness of a rigid resonator cavity is given in [76], and is expressed as

$$s = \frac{\rho c^2 S_n^2}{V_c}. \quad (5.8)$$

where  $V_c$  is the volume of the cavity. The compliance is the inverse of the stiffness, and substituting Equation (5.7) into (5.8) for  $c^2$  and recasting the volume of the cavity as the volume of fluid yields

$$C = \frac{S_n^2}{s} = \frac{V_f}{K_f}. \quad (5.9)$$

In Equation (5.9),  $K_f$  is the stiffness of the entire system, but at this point in the derivation the fluid is the only compliance that has been considered. This term will be revisited and expanded when considering other compliances in the system later in this section. First, the damping effects of the resonator need to be accounted for. The acoustic resistance of the fluid in the neck, including both resistance from viscous effects,  $R_r$ , and radiation resistances,  $R_w$ , is

$$R = (R_r + R_w) / S_n^2. \quad (5.10)$$

The radiation resistance is given from [76] as

$$R_r = \frac{\rho_f c_e k_e^2 S_n^2}{2\pi} \quad (5.11)$$

where  $k_e = \omega / c_e$  is the effective wavenumber in the resonator, at the frequency considered and the effective sound speed in the resonator is given by

$$c_e = \sqrt{\frac{V_f}{\rho_f C}}. \quad (5.12)$$

The derivation of the viscous resistance of the fluid motion in the neck begins with the approximation for the complex wavenumber for fluid lines given by [5],

$$\xi = 1 + \sqrt{\frac{\nu}{j\omega r_n^2}} + \frac{\nu}{j\omega r_n^2}. \quad (5.13)$$

where  $\nu$  is the kinematic viscosity of the fluid and  $r_n$  is the radius of the neck. The loss factor in the complex wavenumber is determined by the ratio of the imaginary to complex part of the complex wavenumber,

$$\alpha_w = -\text{Im}(k\xi)/\text{Re}(k\xi). \quad (5.14)$$

Finally, the loss factor is used in the equation for the viscous resistance in the resonator neck, as given by [76]

$$R_w = 2m\omega\alpha_w. \quad (5.15)$$

At this point, the compliance of the cavity, previously given as Equation (5.9), is expanded to account for the compliance of the shell and the compliance of a liner within the cavity. The compliance of the system can be decomposed into the compliances of the liner, fluid, and shell acting in series, such that

$$C = C_L + C_f + C_s \quad (5.16)$$

where  $C_L$  represents the compliance of the liner,  $C_f$  represents the compliance of the fluid, and  $C_s$  represents the compliance of the shell. Rewriting (5.16) in terms of stiffnesses and substituting into Equation (5.9) gives

$$C = \frac{V_f}{\beta} = V_f \left[ \frac{1}{\beta_L} + \frac{1}{K_f} + \frac{1}{\beta_s} \right]. \quad (5.17)$$

Note that this compliance will also modify the effective speed of sound,  $c_e$ , in Equation (5.12). The compliance of the shell was derived as Equation (3.15) in Section 4.3.1, reprinted here as Equation (5.18)

$$\frac{1}{\beta_s} = \frac{2}{E_s} \left( \frac{r_6^2 + r_5^2}{r_6^2 - r_5^2} + \nu_s \right). \quad (5.18)$$

In Section 4.3.3, Equation (3.20) (shown here as Equation (5.19)) was derived that estimates the compliance of the cavity with the presence of an annular, cylindrical compliant liner,

$$\frac{1}{\beta_L} = \frac{V_L}{E_L (V_c - V_L)} (3 - 4\nu_L) \quad (5.19)$$

where  $V_L$  is the volume of the liner. For the liners discussed in this work, the volume of the liner as a function of static pressure is known experimentally, as described in Section 5.3, and the presence of the liner reduces the fluid volume for a fixed shell size. Furthermore, for liner materials that exhibit viscoelastic behavior (the stress and strain are not in phase), the elastic moduli, such as the Young's or bulk modulus, may be represented as complex values, where the real part is the storage modulus and the imaginary part is the loss modulus as

$$E_L^* = E_L' + iE_L'' \quad (5.20)$$

The ratio of the loss modulus to the storage modulus is referred to as the loss tangent or  $\tan \delta$ , and is a measure of the viscoelasticity of the material,

$$\tan \delta = \frac{E_L''}{E_L'}. \quad (5.21)$$

Thus, the liner introduces material losses to the system in addition to the acoustic radiation and viscous losses.

Continuing the discussion of compliance, substituting Equations (5.18) and (5.19) into (5.17) yields an equation for the compliance of the resonator given the bulk modulus of the fluid and the dimensions and material properties of the shell and liner,

$$C = V_f \left[ \frac{V_L}{E_L^* (V_c - V_L)} (3 - 4\nu_L) + \frac{1}{K_f} + \frac{2}{E_s} \left( \frac{r_6^2 + r_5^2}{r_6^2 - r_5^2} + \nu_s \right) \right]. \quad (5.22)$$

Given a Young's modulus and Poisson's ratio for the liner, the bulk modulus can then be calculated by

$$K_L^* = \frac{E_L^*}{3(1 - 2\nu_L)}. \quad (5.23)$$

The Poisson's ratio is estimated by the manufacturer to be 0.45 for the syntactic foams and 0.4995 for the neat urethanes. From Equation (5.23), the bulk modulus is strictly larger than the Young's modulus for Poisson's ratios greater than 0.33. Given the higher Poisson's ratio for the neat urethanes, their bulk moduli will be much higher than for the syntactic foams even for comparable Young's modulus. The bulk modulus of the fluid is known based on the viscosity, temperature, and pressure of the oil considered, given by the model discussed in Section 4.5.1. For the theory, an assumption of no entrained air in the fluid is made and is justified in Section 6.3.2 for the experiments.

Previously, in Section 4.5.4, the relative magnitude of series compliances, such as developed for the resonator in Equation (5.17), was explored in terms of the effect of one quantity being much larger than the others. The net compliance will be dominated by the highest compliance (or lowest stiffness) in the system, whether it is the liner, fluid, or shell. Even with two compliances of the same magnitude, the net compliance will be half its nominal value. Substituting the first relation in Equation (5.17) into Equation (5.3) yields the relationship

$$\omega_r = \sqrt{\frac{\beta}{LV_f}} \quad (5.24)$$

where  $\beta$  is the total stiffness of the system. To decrease the resonance frequency of a device with a constant volume, either the inertance needs to be raised or the stiffness needs to be reduced. Since increasing the inertance means a larger neck with more fluid, hence a larger device, this contradicts the stated goal of compact devices. Alternately, if a compliant liner is introduced to the cavity, the size of the device can remain the same but the resonance frequency can be reduced, or the size of the device reduced for the same resonance frequency.

From the computation of the resonator impedance, the transmission loss can be calculated from the elements of the transfer matrix for the resonator. The transfer matrix for a Helmholtz resonator mounted in a rigid pipe is

$$T = \begin{bmatrix} 1 & 0 \\ 1/Z_H & 1 \end{bmatrix} \quad (5.25)$$

where  $Z_H$  is the impedance of the resonator from Equation (5.1). The transmission loss is the input-output acoustic energy balance across a two-port device. The transmission loss of the resonator in a system with an infinite downstream pipe (or anechoic termination downstream) can be calculated from the transfer matrix elements by [5]

$$TL = 20 \log_{10} \left[ \frac{1}{2} \left| t_{11} + \frac{t_{12}}{Z_0} + Z_0 t_{21} + t_{22} \right| \right] \quad (5.26)$$

where  $t_{ij}$  are the transfer matrix elements and  $Z_0$  is the acoustic impedance of the test pipe, given by

$$Z_0 = \frac{\rho_f c_f}{S_p} \quad (5.27)$$

where  $S_p$  is the cross-sectional area of the pipe. From the transfer matrix elements in Equation (5.25), Equation (5.26) becomes

$$TL = 20 \log_{10} \left[ \frac{1}{2} \left| 2 + \frac{Z_0}{Z_H} \right| \right]. \quad (5.28)$$

## 6.2 Parameter Study

A theoretical model for the transmission loss of a Helmholtz resonator has thus been developed. From a design perspective, it is of interest to evaluate the theoretical performance of the device given assumed material properties for the liner and fluid, and the impact of variation of the properties on the performance. First, consider two devices of identical neck geometry and resonance frequency. Then, Equation (5.2) is used for comparison, such that

$$\frac{1}{L_1 C_1} = \frac{1}{L_2 C_2}. \quad (5.29)$$

Since  $L$  is a function of the fluid density and neck geometry only, it is the same for both devices, thus  $L_1 = L_2$ . Substituting Equation (5.9) for compliance  $C$ , generalizing the stiffness of the fluid to the stiffness of the system and rearranging yields

$$\frac{\beta_1}{\beta_2} = \frac{V_{f,1}}{V_{f,2}}. \quad (5.30)$$

Therefore, the ratio of fluid volume between otherwise identical devices is directly proportional to the ratio of the effective stiffness. Assuming the introduction of the liner reduces the effective stiffness from that of the fluid alone, approximately 1560 MPa, to 4.79 MPa, this leads to a reduction in the fluid volume by a factor of 326. Some additional cavity volume is required for the liner to occupy, but in general, the device

with the liner would be two orders of magnitude smaller than the unlined device, with all other aspects unchanged.

Likewise, the effect of introducing a liner to the cavity can be explored in terms of the transmission loss. Figure 6-3 depicts the transmission loss of a Helmholtz resonator of the schematic in Figure 6-3 and the dimensions in Table 9, for three configurations: no liner, a liner with a bulk modulus,  $K'$ , of 656 MPa, and a liner with a bulk modulus of 53.8 MPa (these are the bulk moduli of GR9-625 at 21 C, 6.9 and 2.1 MPa). For each case the  $\tan \delta$  is zero. The resonance frequencies for each of these configurations are 295 Hz, 124 Hz, and 36 Hz, respectively – since the resonance frequency is directly related to the effective stiffness of the cavity by Equation (5.24), which is dominated by the stiffness of the liner. Through comparison of the lined vs. unlined  $TL$  predictions, it is evident that a significant reduction in the resonance frequency by an order of magnitude may be obtained solely by introducing a compliant liner to the cavity. The peak  $TL$  decreases and quality factor,  $QF$ , increases as the resonance frequency increases due to the viscous and radiation resistances, both which increase with increasing frequency. The quality factor is the ratio of the resonance frequency and the bandwidth of the resonance, measured 3 dB down from the peak value, given by

$$QF = \frac{f_r}{\Delta f}. \quad (5.31)$$

Higher quality factors signify less damping.

The effect of increasing the losses in the liner by increasing the  $\tan \delta$  of the liner material can also be explored using the theoretical model. The transmission loss for a lined Helmholtz resonator, where the liner has a bulk modulus of 656 MPa, is shown in Figure 6-4 for liner  $\tan \delta$  values of 0.0 through 0.6. The implication of Figure 6-4 is that

the quality factor of the resonance, along with the maximum of the transmission loss, decreases with increasing  $\tan \delta$ , and can be modified independent of the resonator geometry through appropriate design or selection of the liner's material properties.

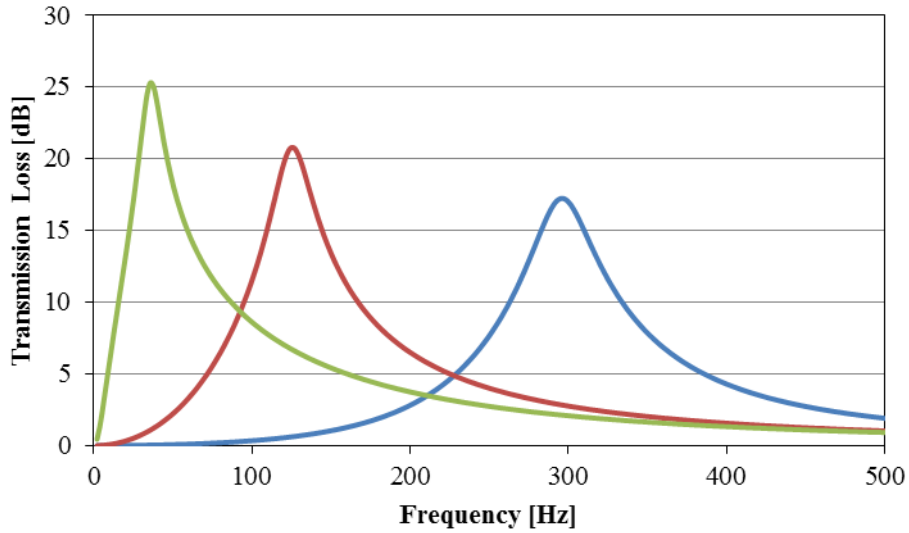


Figure 6-3: Theoretical model for Helmholtz resonator with a neck 37.34 mm long and a radius of 2.97 mm, with a cavity volume of 0.31 L: — No liner, — Liner with  $K' = 656$  MPa, — Liner with  $K' = 53.8$  MPa.

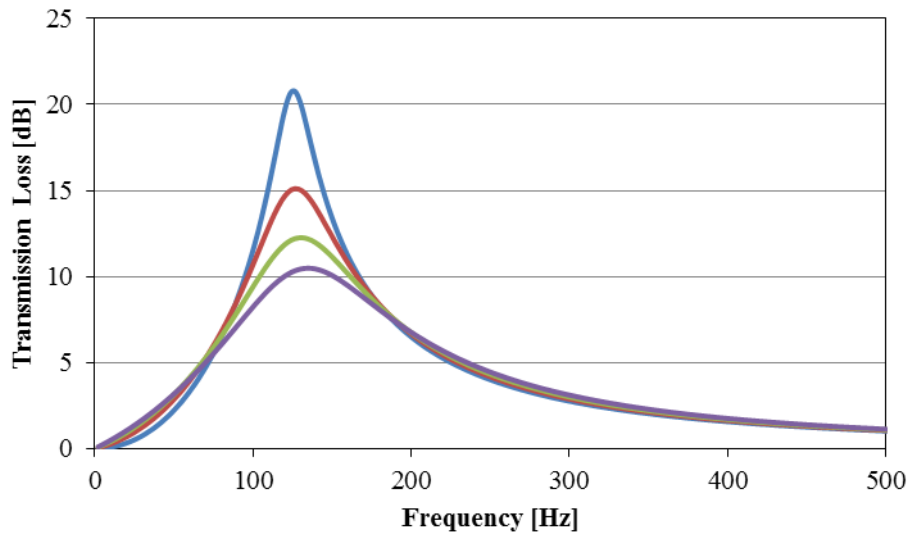


Figure 6-4: Theoretical model for lined Helmholtz resonator with a neck 37.34 mm long and a radius of 2.97 mm, with a cavity volume of 0.31 L: — Liner  $\tan \delta$  0.0, — 0.2, — 0.4, — 0.6.

**Table 9: Dimensions of theoretical Helmholtz resonator.**

|        | Inner Radius | Outer Radius | Length   |
|--------|--------------|--------------|----------|
| Neck   | -            | 2.97 mm      | 37.34 mm |
| Lining | 13.30 mm     | 31.75 mm     | 97.28 mm |

### **6.3 Discussion of Experiment**

Experiments were conducted to test the transmission loss of Helmholtz resonators with compliant linings. The remainder of this chapter is dedicated to validating the assumption of no entrained air in the cavity, and discussing the fit of the theoretical model to the experimental data. Then, the results of the experiments conducted in terms of the effects of temperature and pressure on the bulk modulus and tan delta of the liners are presented and discussed. In addition, other parameters such as the effective speed of sound in the cavity are explored and the neat liners are compared to the syntactic foams to highlight the effect of the microspheres on the performance at elevated pressures.

#### *6.3.1 Method*

The liners tested are those discussed in Section 5.1, and the transmission loss was calculated using the method in Section 5.4 using the test rig as described in Section 5.5. For each liner, the pump in the test rig was turned on, the static pressure was set initially at 2.1 MPa, 30 averages of test data was taken, and the static pressure was set to the next highest desired value and the process repeated. After the highest desired pressure, the pressure was set to approximately 13.8 MPa and the oil was allowed to heat up. When the oil in the cavity reached a desired temperature, the process of acquiring data was repeated starting at the lowest pressure. After three temperatures, the oil was allowed to cool for at least 24 hours to the ambient temperature. The analytical model, developed in Section 6.1, was fit to the experimental data using a least-squares routine with the complex Young's modulus of the liner from Equation (5.22) as the fitting parameter; once

determined, it is converted to bulk modulus and discussed here. The volume of the shell and the liner are compensated for; the liner deformation is estimated as discussed in Section 5.3. In the model, no entrained air is assumed to exist in the cavity: justification of this assumption is given in the following section.

### 6.3.2 *Entrained Air*

In Chapter 4, a model was presented for hydraulic fluids that predicted the bulk modulus of a fluid based on its viscosity function, accounting for changes in temperature, pressure, and volume fraction of entrained air. Since the volume fraction of entrained air can have a significant effect on the bulk modulus of the fluid, as observed in Figure 4-9, it should be quantified for the experiments where the material properties are estimated. However, this value cannot be uniquely determined when solving the inverse problem for the liner properties. To study the effect of an entrained air assumption on the calculated liner properties, the least-squares fit to the experimental data was solved using four different fractions of entrained air,  $X_0$ , in the theoretical model at 22.8 C: 0%; 0.1%; 1.0%; and 10%. The bulk modulus of the liner for these four cases is shown in Figure 6-5, and tabulated in Table 10. Very little error is introduced at values of  $X_0$  up to 1.0%, with the greatest effect at low pressure, resulting in error in bulk modulus at 2.1 MPa of 4.60%. Above 1.0% the deviations are higher, however, the model does not fit the data well at these levels. Examples of the model fit for the 1.0% and 10% cases at 2.1 MPa are shown in Figure 6-6, where it is evident that the least-squares solution is able to find a better solution at the 1.0% level of entrained air versus 10%. The conclusion is then that the volume fraction of entrained air in the system is likely on the order of 1.0% or lower, and, given that the level of error in the material properties at this assumption is generally

much less than 5%, then assuming a volume fraction of entrained air of 0% will introduce very little error into the results.

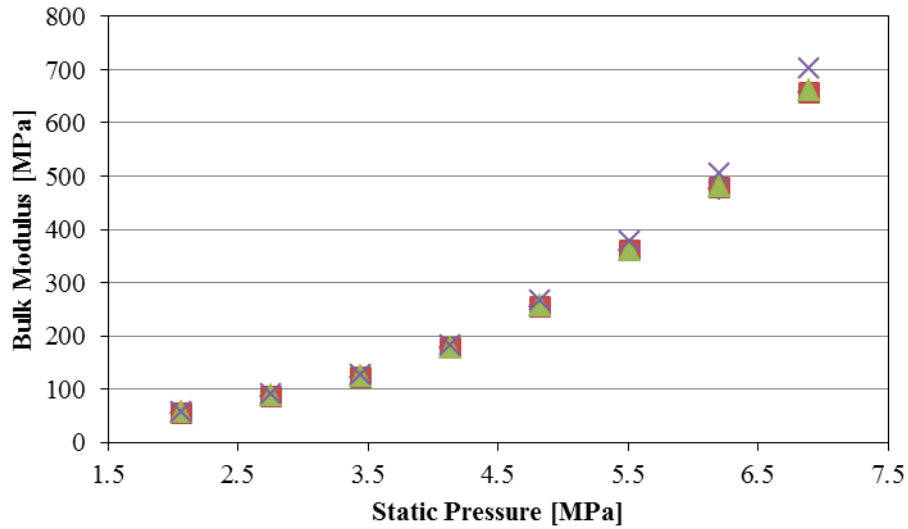
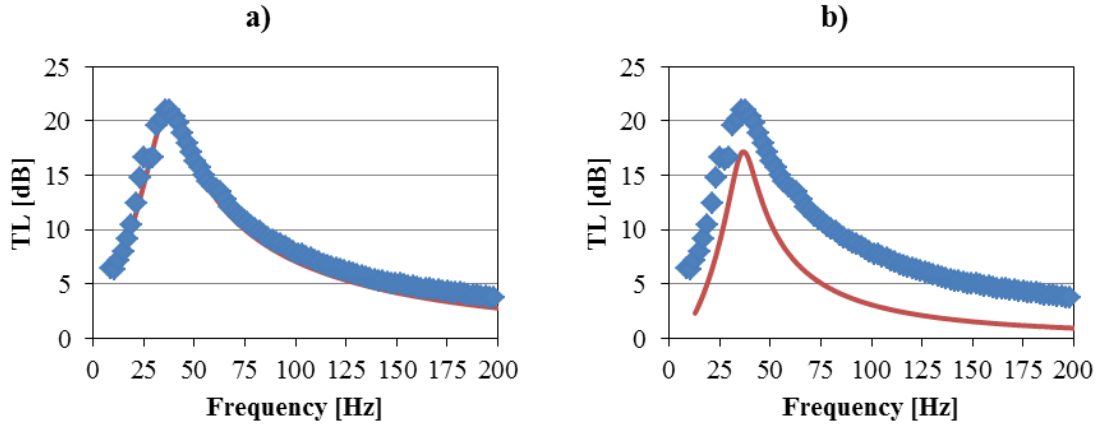


Figure 6-5: Bulk modulus of GR9-625 assuming fraction of entrained air: ♦ 0%, ■ 0.1%, ▲ 1.0%, and × 10%.

Table 10: Bulk modulus of GR9-625 at 22.8 C for assumed fractions of entrained air.

| $X_0$ :               | 0.0%               |                    | 0.1%              |                    | 1.0%              |                    | 10%               |  |
|-----------------------|--------------------|--------------------|-------------------|--------------------|-------------------|--------------------|-------------------|--|
| Static Pressure [MPa] | Bulk Modulus [MPa] | Bulk Modulus [MPa] | Error from 0% [%] | Bulk Modulus [MPa] | Error from 0% [%] | Bulk Modulus [MPa] | Error from 0% [%] |  |
| 2.1                   | 53.8               | 54.4               | 1.04              | 56.3               | 4.60              | 57.0               | 6.05              |  |
| 2.8                   | 86.2               | 86.6               | 0.45              | 88.4               | 2.49              | 90.4               | 4.87              |  |
| 3.4                   | 122.5              | 122.8              | 0.19              | 124.0              | 1.23              | 127.2              | 3.78              |  |
| 4.1                   | 176.5              | 176.6              | 0.09              | 177.7              | 0.70              | 182.7              | 3.54              |  |
| 4.8                   | 254.4              | 254.6              | 0.07              | 255.9              | 0.60              | 265.8              | 4.48              |  |
| 5.5                   | 359.5              | 359.7              | 0.06              | 361.5              | 0.55              | 378.0              | 5.16              |  |
| 6.2                   | 477.1              | 477.4              | 0.06              | 479.8              | 0.57              | 505.3              | 5.91              |  |
| 6.9                   | 656.5              | 656.9              | 0.06              | 660.7              | 0.64              | 703.2              | 7.11              |  |



**Figure 6-6** Fit of experiment to model for GR9-625 at 2.1 MPa and 22.8 C assuming a) 1.0% entrained air b) 10% entrained air: ♦ Experiment — Model.

### 6.3.3 Model Fit

As an example of the transmission loss data and the fit of the theoretical model, using the assumption of 0% entrained air, the  $TL$  for liner GR23 461-663 is shown in Figure 6-7 along with the fit of the theoretical model to the data for pressures of 2.1, 6.9, and 21 MPa. The material properties determined for these conditions are listed in Table 11 for reference. The model fits the data extremely well at 6.9 and 21 MPa, and underestimates the peak  $TL$  of the experimental data at 2.1 MPa by less than 1 dB. The data that drops below 0 dB at low frequencies are the result of artifacts in the experiment, along with the troughs near 420 Hz. The artifacts are described in more detail in Section 7.3 and do not appreciably affect the least-squares fit of the model. Figure 6-7 also shows the pressure dependence of the material: the resonance frequency of the prototype Helmholtz resonator varies from 42 Hz at 2.1 MPa to 335 Hz at 21 MPa. This wide range of resonance frequencies is associated with an even wider range of liner bulk modulus as pressure increases: the functional relationship between system stiffness (a function of liner bulk modulus) and resonance frequency was shown previously as Equation (5.24).

The pressure dependence to the liner bulk modulus will be discussed in more detail for each liner material in the next section.

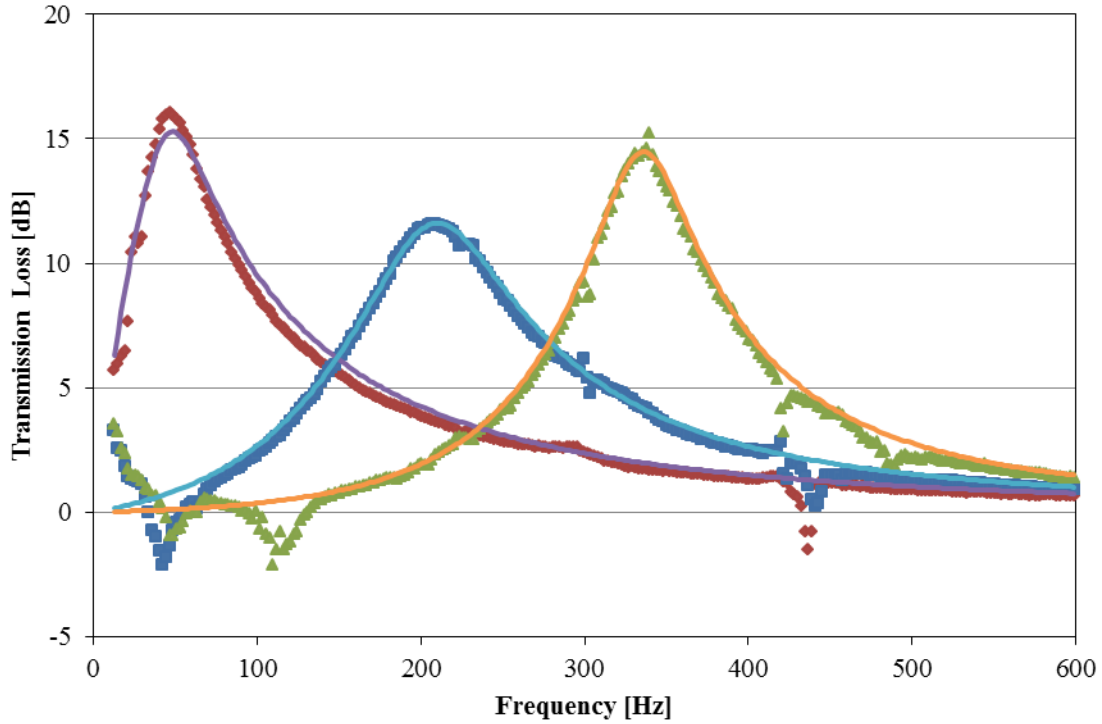


Figure 6-7: Measured transmission loss of liner GR23 461-663, model: — 2.1 MPa, — 6.9 MPa, — 21 MPa; experiment: ◆ 2.1 MPa, ■ 6.9 MPa, ▲ 21 MPa.

Table 11: Liner GR23 461-663 calculated bulk modulus and tan delta values at three pressures.

| Pressure [MPa] | Bulk Modulus [MPa] | Tan Delta [ND] |
|----------------|--------------------|----------------|
| 2.1            | 82.31              | 0.66           |
| 6.9            | 2202               | 0.26           |
| 20.7           | 8957               | 0.09           |

## 6.4 Experimental Results

### 6.4.1 General Behavior

To give a general picture of the bulk modulus as a function of temperature and pressure, the bulk modulus for liner GR23-633 is shown in Figure 6-8 for temperatures from 23 to 33 C. The observed bulk modulus is higher for higher temperatures: this is physically consistent with the idea that the post-buckled microspheres are essentially air

pockets, which then stiffen with increasing pressure. From the properties of viscoelastic materials, however, the glass transition shifts 10 C higher for every factor of ten increase in frequency. Thus, for the same frequency but higher temperatures, the host material should be getting softer in the same frequency range for increasing temperature. The data in Figure 6-8 runs counter to this, since the bulk modulus instead increases with temperature. A brief study of the literature for the effect of pressure on polymers finds some evidence for increasing elastic modulus with increasing pressure, from Sauer [77]. It is important to note, however, that this study was for neat polymers where the mechanism by which modulus changes with pressure is likely not the same as in the syntactic foams studied here.

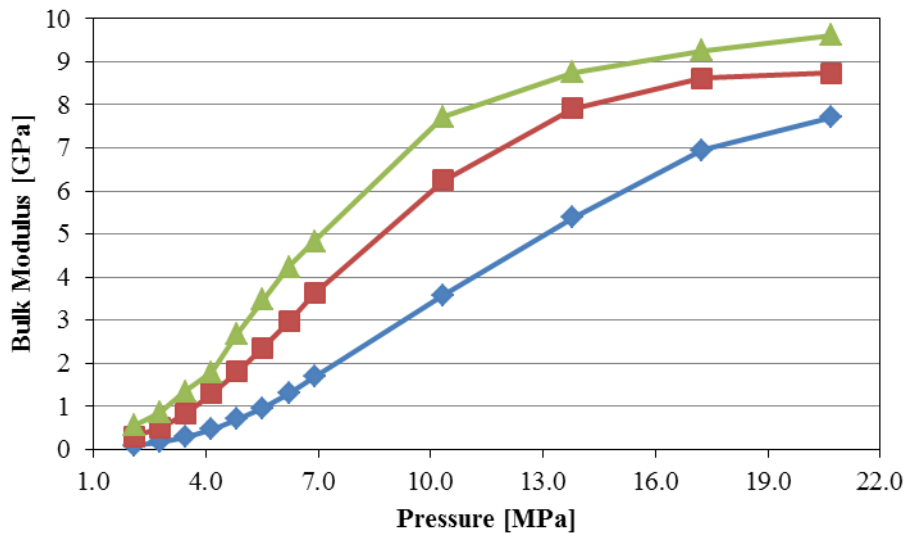


**Figure 6-8: Bulk modulus of liner GR23-633 at ◆ 23 C, ■ 26 C, and ▲ 33 C.**

A pressure-dependent behavior for the neat urethane liners is similarly observed. The bulk modulus of liner GR23 over the range 2.1-6.9 MPa is shown in Figure 6-9 for temperatures of 23-33 C – note that this pressure range is different than that shown in Figure 6-8, as only GR23-633 and GR23 461-663 were tested up to 21 MPa. For the liner

HRPG15(12), shown in Figure 6-10, it is interesting to note that the bulk modulus does not strictly increase with temperature for this material – the data at 26 C and 33 C are effectively the same from 4-6.9 MPa. The bulk modulus of liner GR9 is shown in Figure 6-11. For both HRPG15(12) and GR9, the bulk modulus above 30 C is not strictly stiffer than at lower temperatures. In fact, for HRPG15(12) the bulk modulus at 32 C is less than at 23 C for 3.4 MPa, and for GR9 the bulk modulus at 32 C is less than at 23 C from 5.5 to 6.9 MPa.

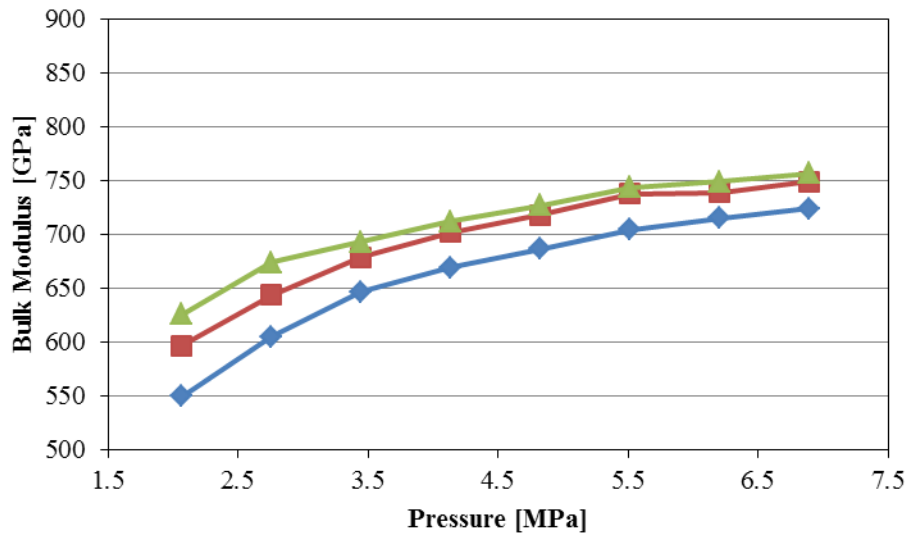


Figure 6-9: Bulk modulus of liner GR23 at ◆ 23 C, ■ 26 C, and ▲ 33 C.

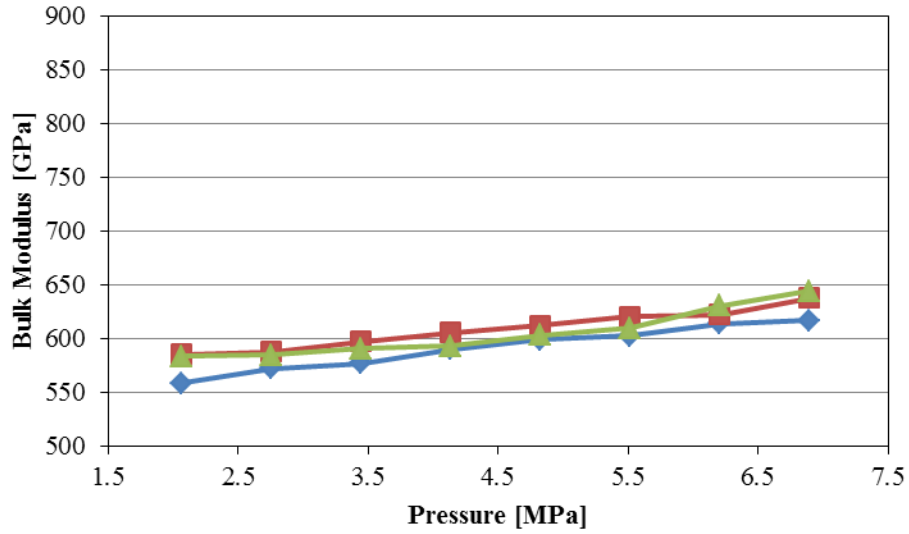


Figure 6-10: Bulk modulus of liner HRPG15(12) at  $\blacklozenge$  23 C,  $\blacksquare$  25 C, and  $\blacktriangle$  32 C.

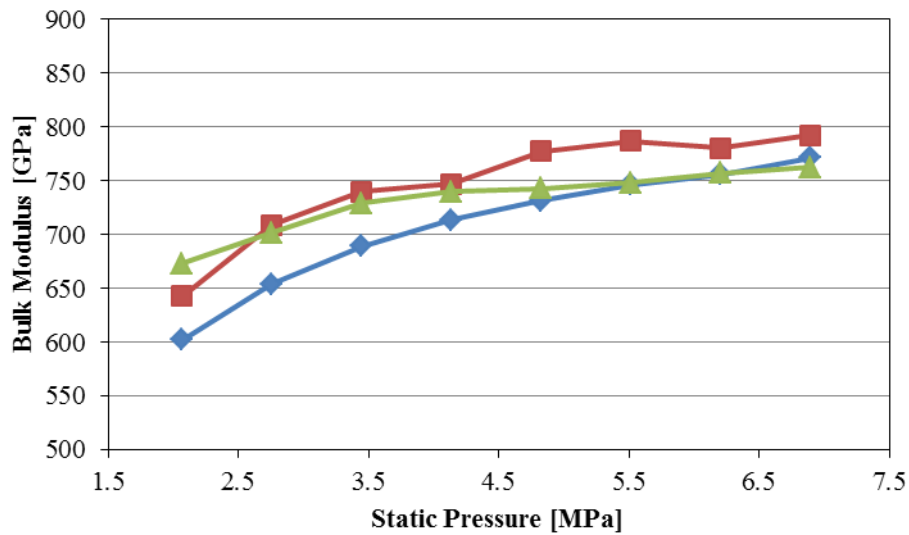


Figure 6-11: Bulk modulus of liner GR9 at  $\blacklozenge$  23 C,  $\blacksquare$  25 C, and  $\blacktriangle$  32 C.

#### 6.4.2 Stiffness Comparison

To observe the relationship between the total system stiffness and each of the constituent stiffness terms in Equation (5.17), these terms were acquired using the least-squares fit and plotted for 2.1 MPa and approximately 21 C for liner GR9-625 in Figure 6-12 and for GR9 in Figure 6-13. The total stiffness is lower than any single stiffness,

which is expected. The shell stiffness and fluid stiffness are the same for both cases – the significant difference, and what most directly impacts the total stiffness, is the stiffness of the liner. Note that this liner stiffness is not the bulk modulus of the material, but the entire term including the volume terms and the Poisson’s ratio. Between Figure 6-12 and Figure 6-13, the total system stiffness including the neat urethane liner is 39 times higher at this pressure than when including the syntactic foam. This change in stiffness dramatically lowers the resonance frequency of the device. In Figure 6-13, it is observed that the stiffness of the neat liner is less than the stiffness of the fluid, which would normally imply improved compliance: however, inclusion of the liner also raises the volume of fluid in the cavity, and the compliance change is not enough to overcome the volume change. For instance, the resonance frequency for the resonator with an empty cavity is 295 Hz: for the cavity with a GR9 liner at the conditions listed, the resonance frequency is 320 Hz. Thus, even with lower total stiffness, the volume of fluid is reduced to the extent that the resonance frequency is increased.

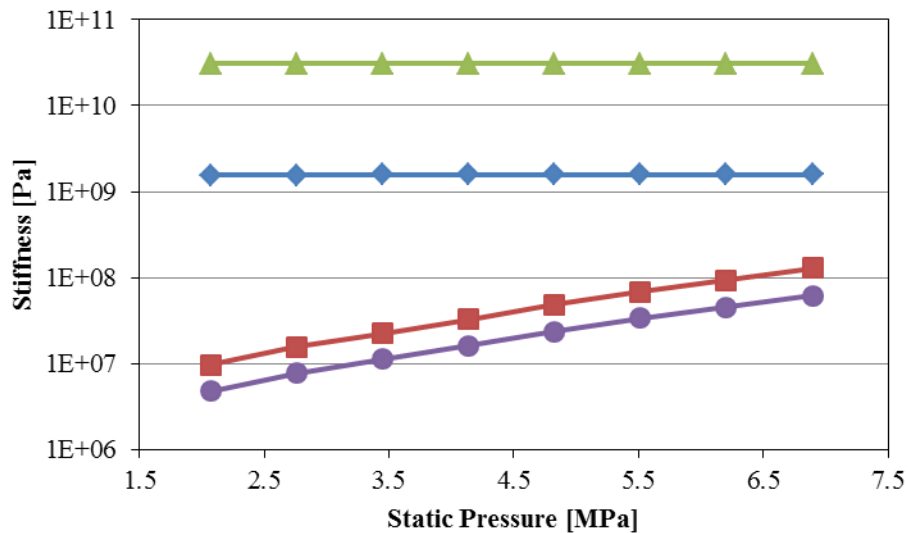
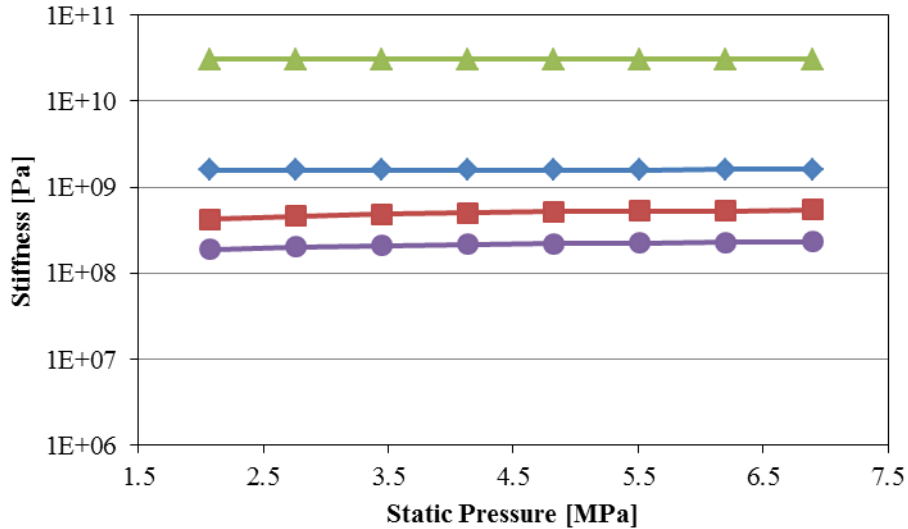


Figure 6-12: Constituent stiffness terms for a Helmholtz resonator with liner GR9-625 at 2.1 MPa and 22.8 C: ▲ shell, ◆ fluid, ■ liner, ● total.



**Figure 6-13: Constituent stiffness terms for a Helmholtz resonator with liner GR9 at 2.1 MPa and 20.0 C: ▲ shell, ◆ fluid, ■ liner, ● total.**

### 6.4.3 Voided vs. Neat

The voiding has a dramatic effect on all compositions. Among all of the neat liners, the lowest estimated bulk modulus of 549 GPa is with the GR23 liner at 22.6 C. This is in contrast to the lowest estimated bulk modulus with a syntactic foam liner of 53.8 MPa, which is GR9-625 at 26.3 C. This is a difference of four orders of magnitude smaller than the softest neat liner. To show this change graphically, the bulk modulus of the GR23 and GR23-633 compositions are graphed on a logarithmic scale in Figure 6-14. This difference in the bulk modulus leads to dramatically lower resonance frequencies – to the extent that the resonance frequency at 2.1 MPa is 48 Hz for the voided liner and 308 Hz for the neat liner. This gap shrinks to 192 Hz to 342 Hz at 6.9 MPa, but the resonance frequency of the voided liner is still nearly half that of the neat liner at this pressure. Similarly, this difference in liner bulk modulus can permit devices that are much smaller for the same resonance frequency – Equation (5.30) showed a direct and proportional relationship between the effective stiffness of the cavity and the cavity

volume for otherwise identical Helmholtz resonators. Thus, using a liner that has a bulk modulus of up to four orders of magnitude more compliant than another liner of the same size, for a total stiffness up to two orders of magnitude less, will permit devices that are up to two orders of magnitude smaller in volume.

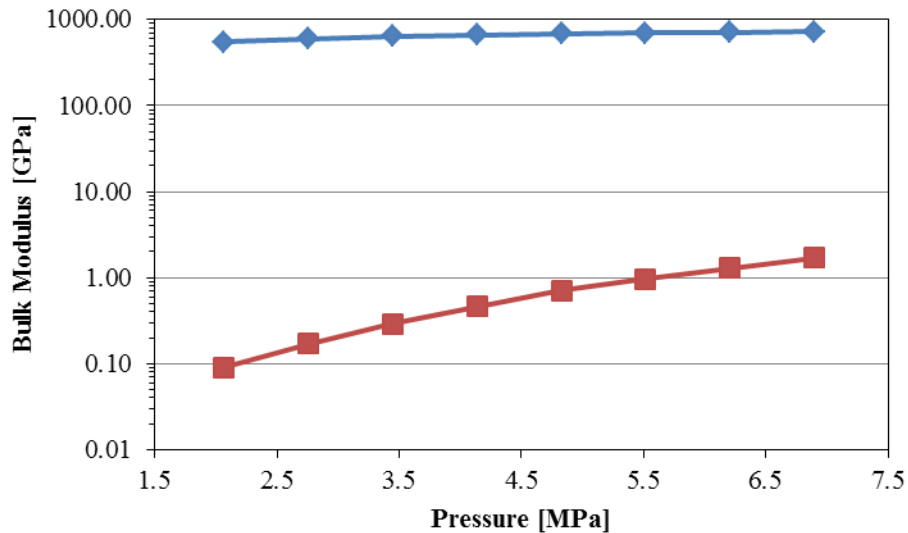


**Figure 6-14:** Bulk modulus of ◆ GR23, neat urethane, at 26 C, ■ GR23-633, syntactic foam, at 29 C.

#### 6.4.4 Pressure Effects

As observed in Figure 6-8, there is a significant pressure dependence to the material properties. At pressures above the critical pressure of the microspheres, at a state where the microspheres have buckled and are effectively air pockets within the material which stiffen with increasing pressure. It is then of interest to understand how the pressure dependence changes for different compositions of syntactic foams. The bulk modulus as a function of pressure and temperature for GR9-625, GR23-633, and HRP15(12)-545 are shown on identical scales in Figure 6-15, Figure 6-16, and Figure 6-17, respectively. Considering the three materials, GR9-625 has the lowest bulk modulus across all pressures and temperatures, especially at 6.9 MPa where it is more

than half as stiff as GR23-633 at 29.2 C. From the liner properties at ambient pressure listed in Table 3, GR9-625 has its glass transition point at the highest frequency. This means that the “rubbery” region, where the bulk modulus is near its low-frequency asymptote, extends to higher frequencies for the same temperature than the other materials. Moreover, GR9-625 has the lowest bulk modulus from 2.1-6.9 MPa than the other materials even though its low-frequency bulk modulus is the highest of the three.

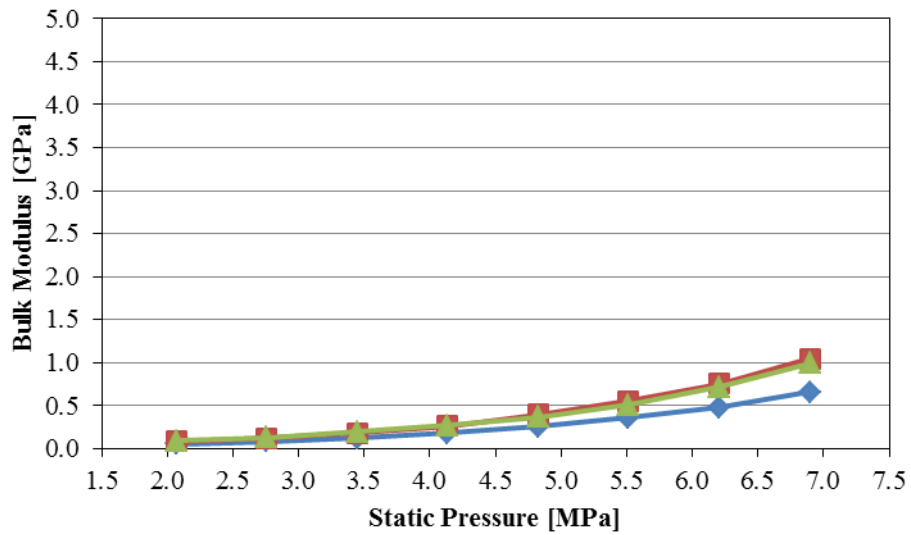


Figure 6-15: Bulk modulus of GR9-625 at  $\blacklozenge$  29.2 C,  $\blacksquare$  37.7 C,  $\blacktriangle$  47.1 C.

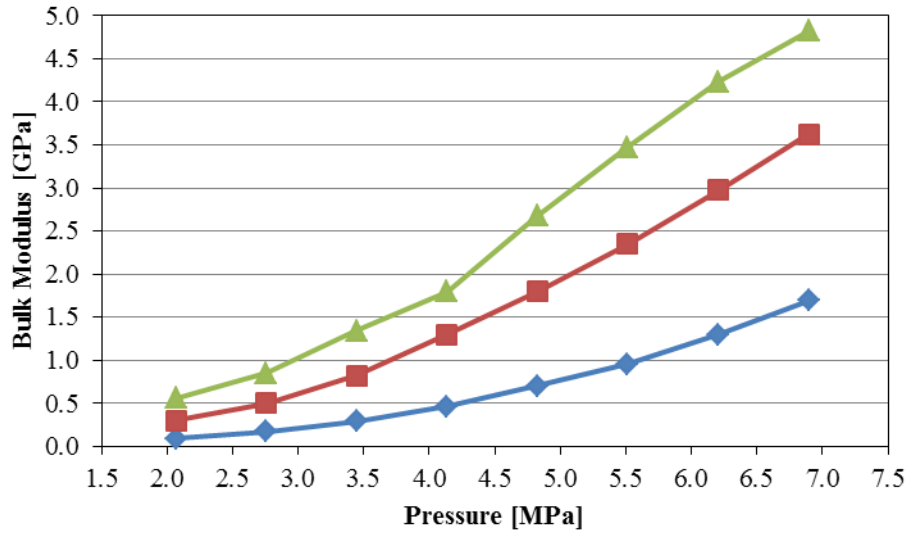


Figure 6-16: Bulk modulus of GR23-633 at  $\blacklozenge$  29.2 C,  $\blacksquare$  37.7 C,  $\blacktriangle$  47.1 C.

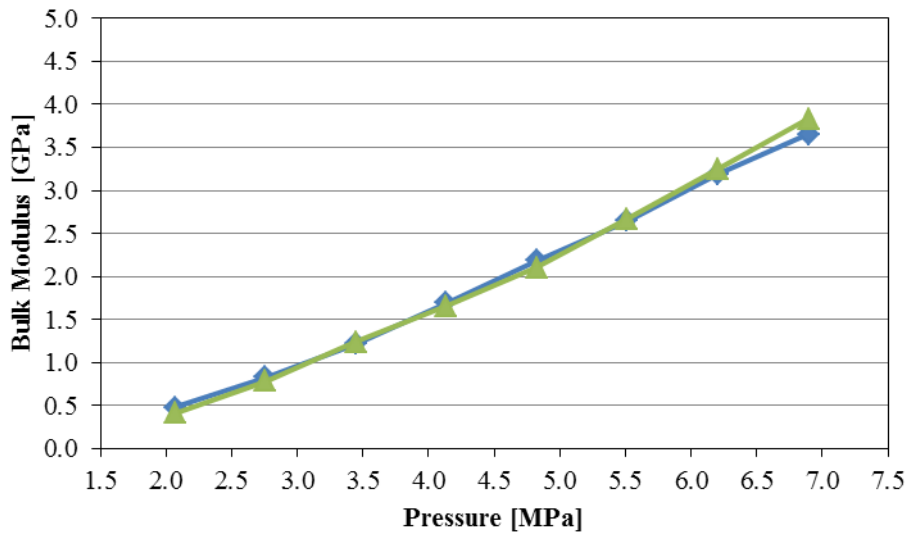


Figure 6-17: Bulk modulus of HRP15(12)-545 at  $\blacklozenge$  29.2 C,  $\blacktriangle$  47.1 C.

The calculated properties of the three syntactic foams reveals that GR23-633 has the most variability in bulk modulus with changes in temperature. This is a trend that is not correlated to properties at ambient pressure. Furthermore, at ambient pressure, it would be expected that the syntactic foam soften as temperature increases, when at elevated pressures, the inverse is observed. The syntactic foams, most especially GR23-

633, show stiffer properties for increasing temperatures. One hypothesis for this behavior is that at higher temperatures, the bulk modulus of the polymer microspheres falls. If the microspheres are softer they have a lower critical pressure, thus will buckle at a lower static pressure and syntactic foam will exhibit a higher stiffness at elevated pressures. Then, at the same pressure a warmer liner will be further into its pressure-stiffening state than a cooler one. A second hypothesis may be that the hysteresis of the buckling behavior affects the results, as the liners are not brought back to ambient pressure between separate temperature tests.

In a like vein, HRP15(12)-545 shows very little change in the bulk modulus from 2.1-6.9 MPa, even though its glass transition point occurs at frequencies in the range of the resonance frequency of the Helmholtz resonator between 20 C and 35 C. Of all the syntactic foams, HRP15(12)-545 should have the most variation as a function of temperature, based on properties at ambient pressure, but experimental results at elevated pressures do not follow this expectation.

#### *6.4.5 Second-Generation Syntactic Foam*

A second generation of syntactic foam was cast for the purpose of developing a material with a higher critical pressure, with the expectation that it would be more compliant at elevated static pressures. This material was cast using the same host material as the GR23-633 liner using smaller, thicker-wall microspheres: AkzoNobel Expancel 461 DET 20 d70. This syntactic foam liner is listed in Table 3 as GR23 461-663. The pressure- and temperature-dependence of the material is shown in Figure 6-18. Comparing the high-pressure design to the original shows different material properties. The calculated bulk modulus is shown for comparison for GR23 461-663 and GR23-633

at two temperatures, approximately 23 C in Figure 6-19 and approximately 33 C in Figure 6-20. At temperatures of about 23 C, the first-generation material, GR23-633, has the same or lower bulk modulus at all pressures – however, this trend shifts at both of the higher temperatures. The second-generation material is more compliant from 2.1-13.8 MPa, and at higher pressures is essentially the same stiffness. This is a promising result which demonstrates that syntactic foams can be made more compliant at higher static pressures by using microspheres with a higher buckling pressure.

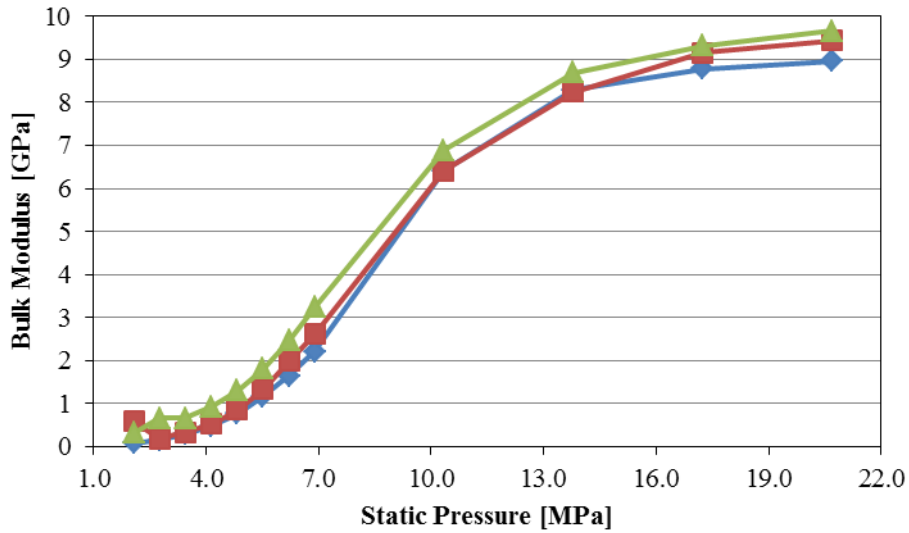


Figure 6-18: Bulk modulus of GR23 461-663,  $\blacklozenge$  24.3 C,  $\blacksquare$  27.7 C,  $\blacktriangle$  32.6 C.

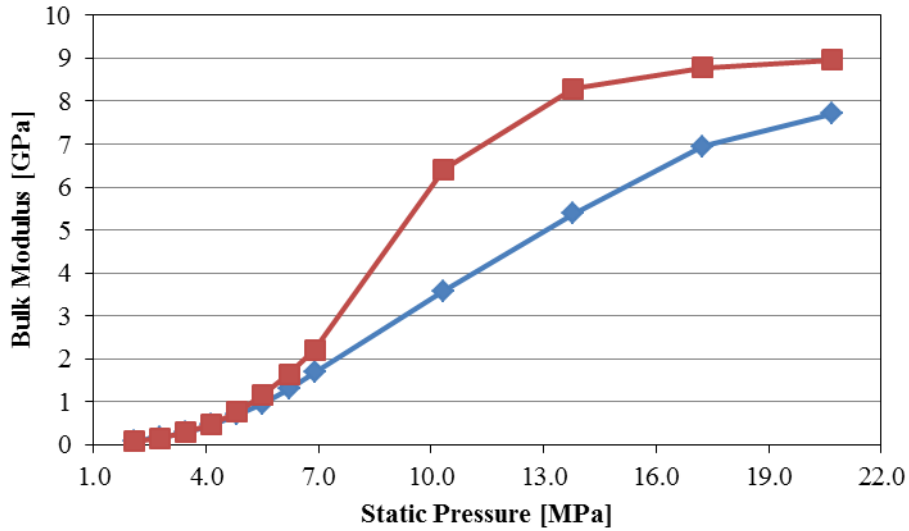


Figure 6-19: Bulk modulus at 23 C, ♦ GR23-633, ■ GR23 461-663.

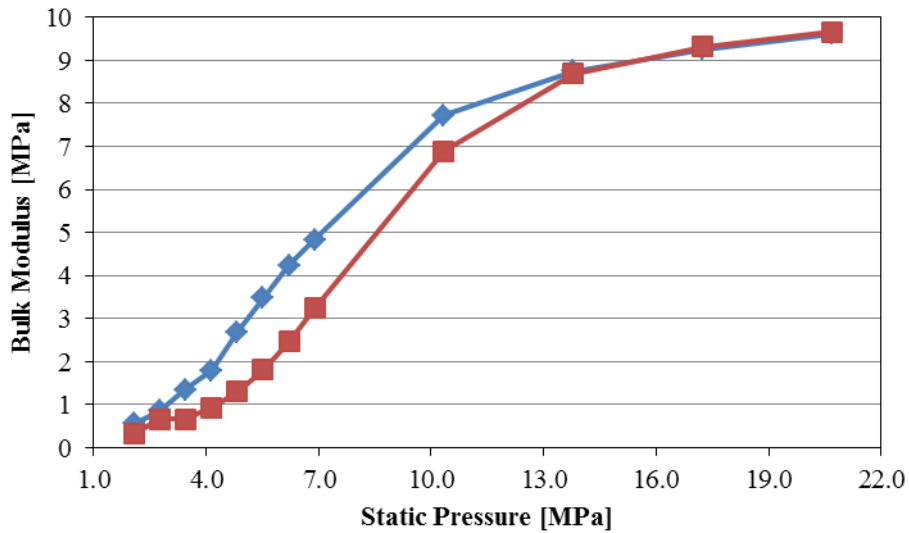


Figure 6-20: Bulk modulus at 33 C, ♦ GR23-633, ■ GR23 461-663.

#### 6.4.6 Tan Delta and Quality Factor

The least-squares routine uses the complex bulk modulus of the liner as a fitting parameter to fit the theoretical model to experimental data. The acoustical losses in the resonator, such as radiation resistance and viscous damping in the neck are accounted for theoretically in the model, so the remaining losses are captured in the complex bulk

modulus and attributed to the liner. Previously in Figure 5-2, the  $\tan \delta$  of three syntactic foam compositions at atmospheric pressure and 35 C were compared that showed HRPG15(12)-545 as having the highest  $\tan \delta$ , followed by GR23-633 and GR9-625. This trend is also observed experimentally at elevated pressures; the  $\tan \delta$  for these three liners at approximately 32 C is shown in Figure 6-21. The  $\tan \delta$  for each of the syntactic foams decreases with increasing pressure.

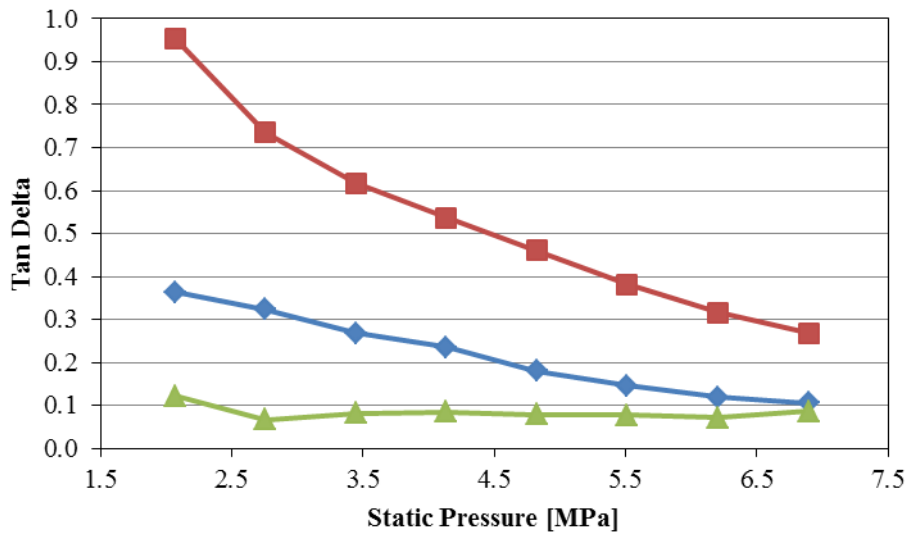


Figure 6-21: Tan delta of liners at 32 C,  $\blacklozenge$  GR23-633,  $\blacksquare$  GR23-633,  $\blacktriangle$  GR9-625.

The  $\tan \delta$  is also generally much higher for the syntactic foams than for the neat urethane liners. As an example, the  $\tan \delta$  for HRPG15(12) and HRPG15(12)-545 for two temperatures is shown in Figure 6-22. The  $\tan \delta$  for the neat liner is less than 0.11 for pressures from 2.1-6.9 MPa, while the  $\tan \delta$  for the syntactic foam is no less than 0.25 and as high as 0.96. From Table 3, the peak  $\tan \delta$  for the neat liners are higher than for the syntactic foams, but under elevated pressure this “lossiness” drops considerably. This is the case for all neat liners; the highest observed  $\tan \delta$  in a neat liner is for HRPG15(12). HRPG15(12)-545 is the only syntactic foam of the three that is observed to have a  $\tan \delta$

that increases with increasing temperature; the other two decrease with increasing temperature. This is shown in Figure 6-23 for GR23-633 at three temperatures. At 10.3 MPa and above, the  $\tan \delta$  changes relatively little: this is also the pressure range in which the bulk modulus levels out. There then appears to be a correlation between the compliance of the material and its lossiness – the neat liners are very stiff and have very low  $\tan \delta$  values, and the syntactic foams have  $\tan \delta$  values that are high at low pressure, and level out at low values as the bulk modulus approaches its maximum value at higher pressures.

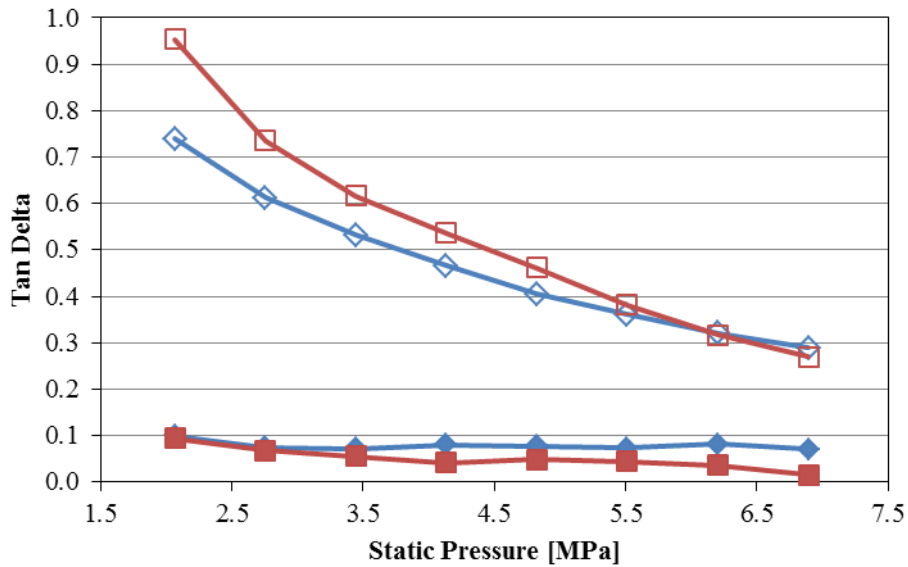
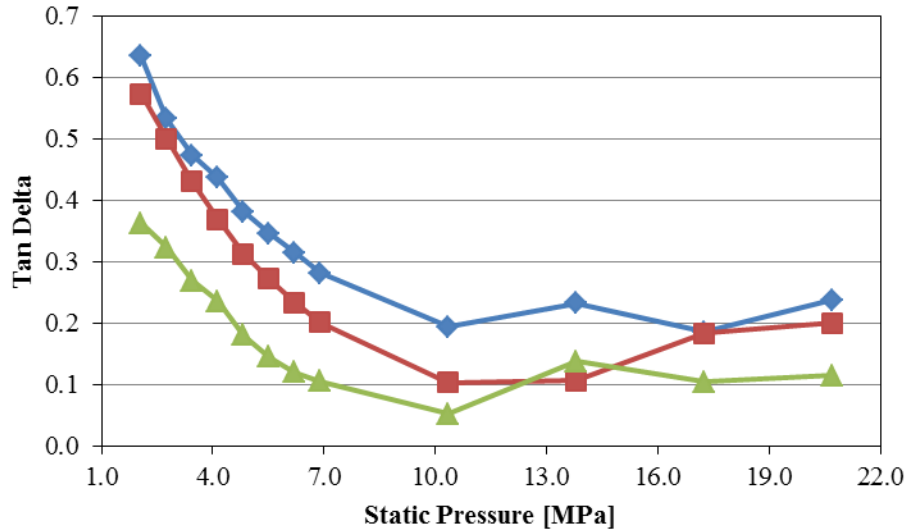


Figure 6-22: The  $\tan \delta$  of liner HRP15(12) at  $\blacklozenge$  22.9 C,  $\blacksquare$  32.6 C, and of liner HRP15(12)-545 at  $\blacklozenge$  24.1 C,  $\square$  32.7 C.



**Figure 6-23: The  $\tan \delta$  of liner GR23-633 at  $\blacklozenge$  23.3 C,  $\blacksquare$  25.8 C,  $\blacktriangle$  33.0 C.**

The amount of damping associated with a resonance phenomena can be quantified in a term known as the quality factor,  $QF$ . This factor was discussed when presenting the model in Section 6.2. The  $QF$  is calculated from the theoretical model that is fit to the experimental data to get more reliable values for resonance frequency and bandwidth. The highest observed  $QF$  is 11.6 for the GR23 liner at 32.5 C and 6.9 MPa and the lowest observed  $QF$  is 1.1 for the GR23-633 liner at 23.3 C and 2.1 MPa. Given that high  $QF$  is associated with low damping, the  $QF$  is inversely correlated with  $\tan \delta$ . This can be observed in Figure 6-24 for GR23 and GR23-633 at 23 C: for both liners, the  $\tan \delta$  decreases and the  $QF$  increases with increasing pressure. The  $QF$  is directly a function of the resonance frequency and the bandwidth of the resonance. The bandwidth for the Helmholtz resonator varies from 19 Hz for GR9-625 at 2.1 MPa and 35 C, a condition associated with a low resonance frequency and a low  $\tan \delta$ , to 118 Hz for HRP15(12)-545 at 3.4 MPa and 33 C, which is a condition associated with a high resonance frequency and a high  $\tan \delta$ .

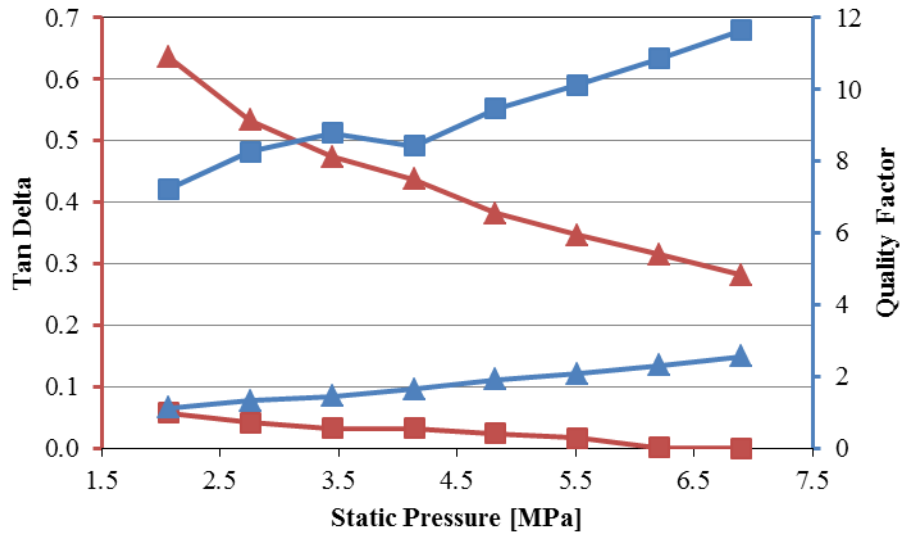


Figure 6-24: Tan Delta and Quality Factor at 23 C for ■ GR23 ▲ GR23-633.

#### 6.4.7 Speed of Sound

A parameter of the Helmholtz resonator that is important to note, as it relates to other resonant-style devices, is the effective speed of sound in the cavity. This informs the degree to which the compliance of the liner modifies the speed of sound of the fluid, for the purpose of understanding how other resonant-style devices may be affected. The effective speed of sound in the cavity is calculated by Equation (5.12) in the model, which involves the volume of the cavity, the effective density (the density of the fluid and liner each times their volume, divided by the total cavity volume) and the cavity compliance. The bulk modulus of the liner and the cavity compliance are inversely related, so the bulk modulus of the liner and the effective speed of sound should be proportional. This relationship is shown in Figure 6-25 for GR9-625 at 22.8 C, which exhibits the lowest effective speed of sound at 103 m/s. This is two orders of magnitude lower than the bulk speed of sound of hydraulic fluid, which is approximately 1400 m/s. To show this relationship at higher pressures, the bulk modulus and effective sound speed

are presented for GR23 461-663 from 2.1-21 MPa in Figure 6-26, which also exhibits the highest effective speed of sound at 919 m/s. It is clear that the speed of sound reaches a maximum value as pressure increases.

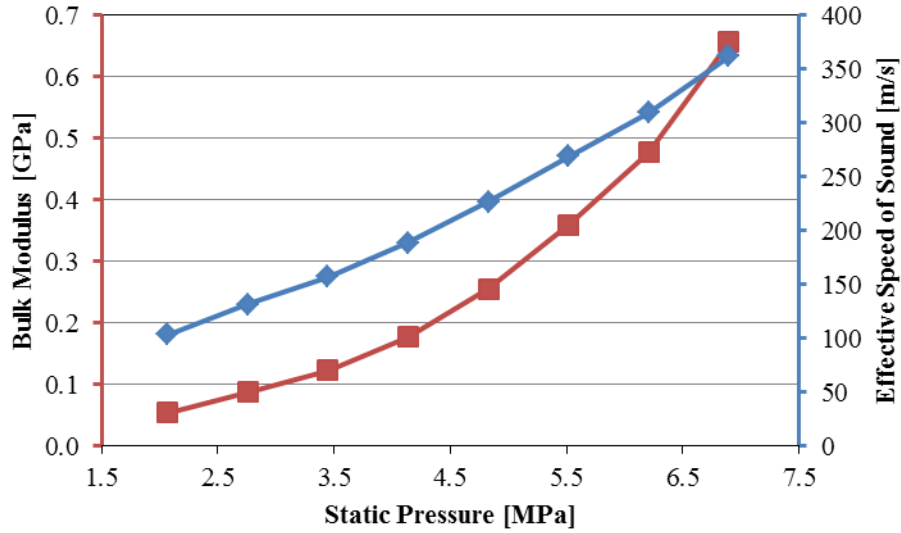


Figure 6-25: The bulk modulus and effective speed of sound in the Helmholtz resonator with liner GR9-625 at 22.8 C: ■ bulk modulus, ◆ effective speed of sound.

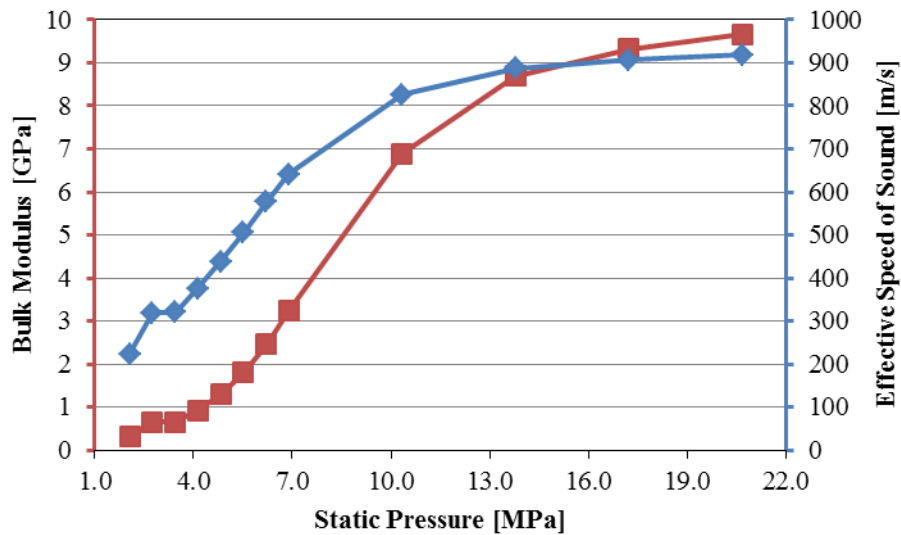


Figure 6-26: The bulk modulus and effective speed of sound in the Helmholtz resonator with liner GR23 461-663 at 32.6 C: ■ bulk modulus, ◆ effective speed of sound.

## CHAPTER 7

### TUNING COIL AND HERSCHEL-QUINCKE TUBE

In this chapter, a tuning coil and Herschel-Quincke tube are modeled, where a compliant liner, made of syntactic foam, forms a compliant inner wall of the annular waveguide. The devices studied here are of the concentric side-branch resonator type: this is in contrast to tuning coils used in hydraulic power steering systems which use a coiled tube (called the “tuner”) within a hydraulic hose to achieve wave interference effects and damping through viscous losses and leakage through the tuner. The Herschel-Quincke tube studied here uses a different sound speed in a parallel path of a similar length to achieve phase interference, while other types use two tubes of physically different lengths to achieve the same objective. For the tuning coil studied here, the effects of liner compliance on the first resonance frequency of the device are explored theoretically along with the effect of liner damping. The model is extended to Herschel-Quincke tubes, where the performance of the device with a compliant liner is explored theoretically. For a prototype compliant-lined tuning coil, experimental transmission loss is presented and compared to the predictions of the theoretical model. The behavior of commercially-available tuning coils is studied and compared to the prototype device along with claims in the literature regarding their performance.

#### 7.1 Modeling – Tuning Coil

Previous work by Hastings and Chen [26, 36] sought to model tuning coils using a solution that encompassed only plane waves in the flow path and annulus of the tuning coil, capturing the effects of viscous losses in the fluid. The model used in this work

follows the same development: the key addition will be the treatment of a flexible wall, in the form of a syntactic foam liner, which significantly modifies the speed of sound in the branch. Figure 7-1 shows a schematic of the device with the port numbering used in the derivation.

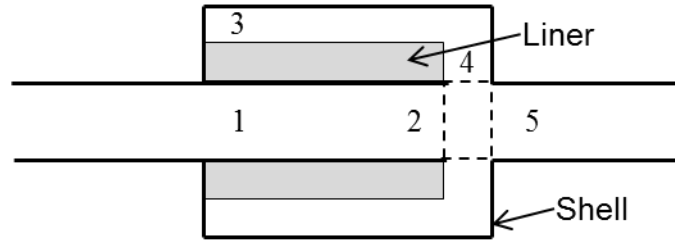


**Figure 7-1: Port numbering of tuning coil.**

The acoustic propagation in the main flow path of the tuning coil, from port 1 to 2, is that of a straight, rigid pipe and is represented in transfer matrix form by D'Souza and Oldenburger [78] by

$$\begin{pmatrix} P_1 \\ Q_1 \end{pmatrix} = \begin{bmatrix} \cosh(\Gamma_1 L) & \frac{Z_{c1}}{\pi r_1^2} \sinh(\Gamma_1 L) \\ \frac{\pi r_1^2}{Z_{c1}} \sinh(\Gamma_1 L) & \cosh(\Gamma_1 L) \end{bmatrix} \begin{pmatrix} P_2 \\ Q_2 \end{pmatrix} \quad (6.1)$$

where  $r_1$  is the inner diameter of the annulus,

$$Z_{c1} = \frac{\rho c_1}{\alpha} \quad (6.2)$$

is the characteristic impedance,

$$\Gamma_1 = \frac{s\alpha}{c_1} \quad (6.3)$$

is the propagation constant where  $s = j\omega$  is the Laplacian operator, and

$$c_1 = \sqrt{\frac{K_f}{\rho_f}} \quad (6.4)$$

is the speed of sound in the flow path where  $K_f$  and  $\rho_f$  are the bulk modulus and density of the fluid. The component of the propagation constant which models the frequency-dependent attenuation per unit distance is the function

$$\alpha = \left[ 1 - \frac{2}{ir_1\sqrt{s/\nu}} \frac{J_1(ir_1\sqrt{s/\nu})}{J_0(ir_1\sqrt{s/\nu})} \right]^{-1/2} \quad (6.5)$$

where  $J_0$  and  $J_1$  are Bessel's function of the first kind of order zero and one and  $\nu$  is the kinematic viscosity of the fluid. Likewise, the acoustic propagation in the annular path is given by the method of Washio and Konishi [79] as the matrix

$$\begin{pmatrix} P_3 \\ Q_3 \end{pmatrix} = \begin{bmatrix} \cosh(\Gamma_2 L) & \frac{Z_{c2}}{\pi(r_5^2 - r_4^2)} \sinh(\Gamma_2 L) \\ \frac{\pi(r_5^2 - r_4^2)}{Z_{c2}} \sinh(\Gamma_2 L) & \cosh(\Gamma_2 L) \end{bmatrix} \begin{pmatrix} P_4 \\ Q_4 \end{pmatrix} \quad (6.6)$$

where the impedance

$$Z_{c2} = \frac{\rho c_2}{G} \quad (6.7)$$

and the propagation constant is

$$\Gamma_2 = \frac{sG}{c_2} \quad (6.8)$$

where  $G$  is the component of the propagation that models the attenuation in the fluid, and is defined later in this section. The radii,  $r_4$  and  $r_5$ , correspond to the outer radius of the liner and the inner radius of the shell. The speed of sound in this section is

$$c_2 = \sqrt{\frac{\beta}{\rho_f}} \quad (6.9)$$

where  $\beta$  is the effective stiffness of the hydraulic oil in the flow path, given by the springs-in-series method described in Section 4.5.4 as

$$\frac{1}{\beta} = \frac{1}{K_f} + \frac{1}{\beta_c} \quad (6.10)$$

where  $\beta_c$  is the stiffness of the waveguide. This model uses the mechanical compliance of the liner and shell to modify the bulk modulus of the fluid to determine the effective stiffness. The compliance of the waveguide formed between the outer radius of a compliant liner and the inner radius of a rigid shell, given an unconstrained inner radius of the liner, is calculated using Equation (3.21), shown here as Equation (6.11),

$$\frac{1}{\beta_c} = \frac{2r_4^2}{E_L^*(r_5^2 - r_4^2)}(1 - \nu_L) \quad (6.11)$$

where  $E_L^*$  and  $\nu_L$  are the Young's modulus and Poisson's ratio of the liner. The use of this equation presumes that the liner inside a tuning coil is unconstrained at its inner boundary, even at elevated pressures as it shrinks in compression. Should the liner shrink to the extent that it becomes constrained on the annulus, Equation (3.24) would then be the appropriate function for the waveguide compliance. It is also important to note that the Young's modulus in Equation (6.11) may be a complex value, depending on the  $\tan \delta$  of the material, which will introduce additional losses into the acoustic propagation in the branch beyond the viscous losses in the fluid.

Both the speed of sound in the waveguide and viscous losses are modeled for the annular waveguide. The loss factor for wave propagation in the annular section is given by

$$G = \left[ 1 - \frac{2}{i\chi(1-m^2)} \frac{\begin{vmatrix} J_{01} - J_{02} & J_{12} - mJ_{11} \\ Y_{01} - mY_{02} & Y_{12} - mY_{11} \end{vmatrix}}{\begin{vmatrix} J_{01} & J_{02} \\ Y_{01} & Y_{02} \end{vmatrix}} \right]^{-1/2} \quad (6.12)$$

where

$$\chi = \sqrt{\frac{r_5^2 s}{\nu}} \quad (6.13)$$

$$m = \frac{r_4}{r_5} \quad (6.14)$$

$$J_{np} = J_n(ir_p \sqrt{s/\nu}) \quad (6.15)$$

$$Y_{np} = Y_n(ir_p \sqrt{s/\nu}) \quad (6.16)$$

for  $p=[4 \ 5]$  and  $J$  and  $Y$  are the  $n$ -th order Bessel functions of the first and second kind. The matrices in Equation (6.12) are ill-conditioned and difficult to compute.

Washio and Konishi addressed this by presenting an approximation to  $G$  for  $|\chi| \gg 1$ ,

$$G' = 1 + \frac{1}{(1-m)\chi} + \frac{3}{2(1-m)^2 \chi^2} - \frac{1-22m+m^2}{8m(1-m)^3 \chi^3}. \quad (6.17)$$

For the viscosity of hydraulic oil at 25 C and  $r_4 = 13.30$  mm,  $|\chi|$  is no less than 5.6 at 2.1 Hz, so the approximation is considered valid over the frequency range of interest.

The boundary conditions for the two sections, the main flow path and the annulus, are such that the pressure must be equal at the ports, the velocity at the closed end of the annular section is zero, and the velocity at the downstream port is the difference between the velocity in flow path and the branch:

$$\begin{aligned}
P_5 &= P_2 = P_4 \\
Q_5 &= Q_2 - Q_4 \\
Q_3 &= 0
\end{aligned} \tag{6.18}$$

The matrices in Equation (6.1) and Equation (6.6) are then assembled using the boundary conditions in Equation (6.18) into

$$\begin{pmatrix} P_1 \\ Q_1 \end{pmatrix} = \begin{bmatrix} 1 & 0 \\ \frac{\pi(r_5^2 - r_4^2)}{Z_{c2}} \sinh(\Gamma_2 L) & 1 \end{bmatrix} \begin{bmatrix} \cosh(\Gamma_1 L) & \frac{Z_{c1}}{\pi r_1^2} \sinh(\Gamma_1 L) \\ \frac{\pi r_1^2}{Z_{c1}} \sinh(\Gamma_1 L) & \cosh(\Gamma_1 L) \end{bmatrix} \begin{pmatrix} P_5 \\ Q_5 \end{pmatrix} \tag{6.19}$$

Finally, the transmission loss of the tuning coil may be computed from the transfer matrix by

$$TL = 20 \log_{10} \left[ \frac{1}{2} \left| t_{11} + \frac{t_{12}}{Z_0} + Z_0 t_{21} + t_{22} \right| \right] \tag{6.20}$$

where

$$Z_0 = \frac{\rho_f c_f}{S_p} \tag{6.21}$$

and  $S_p$  is the cross-sectional area of the pipe at either end of the tuning coil.

### 7.1.1 Parameter Study

With a model for the tuning coil developed in the previous section, it is of interest to evaluate theoretically how varying different parameters affects the performance of the device. The model for a tuning coil incorporates the fluid model, based on temperature and pressure, models for viscous losses in both the main flow path and annular section, and the effect on the speed of sound of the branch due to the compliance of the wall. The material properties of liner GR23 461-633 are used in the model at different pressures to show the effect of varying liner stiffness on the behavior of the tuning coil. In the model,

the outer radius of the liner,  $r_4$ , along with the inner radius of the shell,  $r_5$ , together determine the width of the annular waveguide in the tuning coil, which then determines the damping based on Equation (6.17), along with the temperature and thus viscosity of the oil. As with the Helmholtz resonator, there is assumed to be a small enough level of entrained air in the fluid that its effect is negligible. While this is not true of real systems, this assumption was justified in Section 6.3.2, where the error in the calculated material properties resulting from this assumption was determined to be acceptable. To calculate the transmission loss of the tuning coil, the bulk modulus of liner GR23 461-633 and its measured radii were used in the model to develop theoretical performance curves, along with an assumed Poisson's ratio of 0.45. From the model, the effective bulk modulus of the waveguide, or branch of the tuning coil, and the speed of sound in this path were calculated. These results are shown in Table 12 along with the given pressure and bulk modulus used in the model. The transmission loss for these three pressures is plotted in Figure 7-2.

**Table 12: Properties of a tuning coil using liner GR23 461-633 at 23.3 C.**

| Pressure [MPa] | Bulk modulus of liner [GPa] | Tan $\delta$ of liner [ND] | Effective bulk modulus of branch [GPa] | Speed of sound in branch [m/s] | Frequency of first resonance [Hz] |
|----------------|-----------------------------|----------------------------|--|--------------------------------|-----------------------------------|
| 2.1            | 0.224                       | 0.66                       | 0.016                                  | 140                            | 289                               |
| 6.9            | 5.879                       | 0.27                       | 0.365                                  | 635                            | 1304                              |
| 20.7           | 24.61                       | 0.09                       | 0.923                                  | 1005                           | 2067                              |

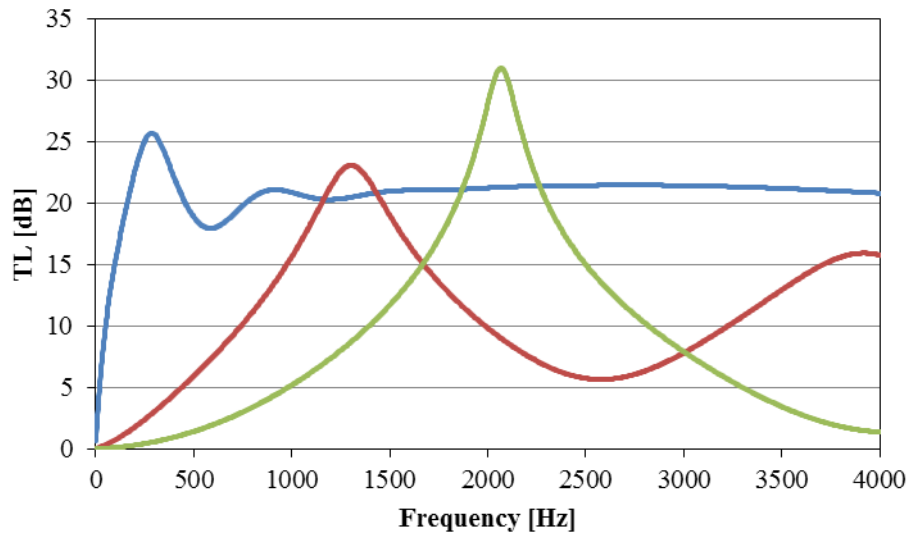


**Figure 7-2: Predicted transmission loss of a tuning coil with GR23 461-633 at 23.3 C at — 2.1 MPa, — 6.9 MPa, and — 20.7 MPa.**

The stiffness of the liner has a dramatic effect on the performance of the tuning coil. The physical mechanism of this effect is the compliance of the waveguide, which is a function of the elastic modulus of the liner, the thickness of the liner and the width of the annular gap formed between the liner and shell. Increased compliance lowers the speed of sound in the branch of the tuning coil. By lowering the speed of sound, the wavelength at a given frequency is shorter, thus the device is physically longer relative to the wavelength of sound. Therefore, the device has the same behavior as a device that is physically larger but does not modify the speed of sound. The effect of lowering the speed of sound in an elastic tube is well known, but the extent to which this can be achieved for a hydraulic system (which operates at high pressure) using syntactic foam is much greater than with conventional materials. From Figure 7-2, the damping observed in the transmission loss for the same material at each pressure is different: for instance, the damping for the *TL* at 2.1 MPa is much higher than at 21 MPa. Of particular interest from Figure 7-2 is the transmission loss at 2.1 MPa – the device exhibits a nearly

constant 20 dB  $TL$  above about 250 Hz. This is largely a result of the high damping and very low effective sound speed: experimental tests should show whether this effect is physical or whether there are limits to the model. There is likely a frequency-dependence to the material damping that is not included here: the  $\tan \delta$  of the syntactic foams from experiments with the Helmholtz resonator only determined a single  $\tan \delta$  value for each pressure based on a narrow band of low frequencies. Thus, the frequency-dependence of this value is unknown and extrapolating the known  $\tan \delta$  to higher frequencies is likely problematic. With respect to the total losses in the device, there are two factors at play: one is the thickness of the gap between the liner and shell, which affects the viscous losses and is also a function of the material properties due to hydrostatic compression, and the other is the  $\tan \delta$  of the liner.

To observe the effects of gap width and  $\tan \delta$  individually, Figure 7-3 shows the transmission loss for this tuning coil at 6.8 MPa for different values of the outer radius of the liner (with the inner radius of the shell fixed) and a liner  $\tan \delta$  of zero. One significant aspect of the behavior with varying gap width – which is also implying a thinner liner – is that not only do the damping and peak  $TL$  change but the compliance of the waveguide decreases with a thinner liner. The peak  $TL$  increases with an increasing gap width due to the higher volume velocity in the branch – more acoustic energy is entering the branch for a higher degree of phase cancellation. The effective speed of sound in the branch increases with decreasing liner thickness, which is consistent with Equation (6.11).

The effect of varying the liner thickness, and thus gap width, in a tuning coil with a compliant liner presents an interesting design decision, as there is a trade-off between taking advantage of additional volume velocity with a thicker gap, while sacrificing

waveguide compliance and thus the effective speed of sound in the branch. Alternately, the liner thickness could be held constant and the gap thickness increased by increasing the inner radius of the shell, which would then result in a larger device.

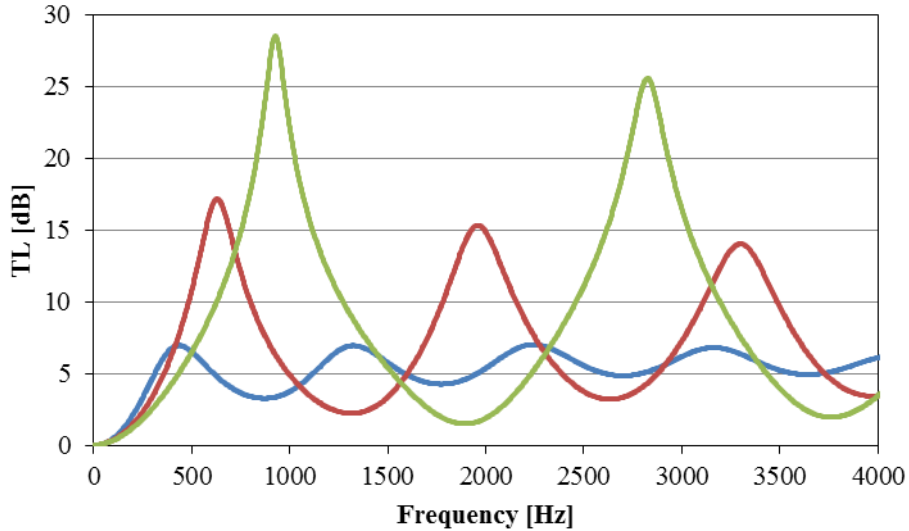


**Figure 7-3: Predicted transmission loss of a tuning coil with GR23 461-633 at 23.3 C at 6.9 MPa, a  $\tan \delta$  of zero, a fixed inner radius of the shell, and an annular gap width of — 0.5 mm, — 1 mm, and — 2 mm.**

The effect on the transmission loss from the  $\tan \delta$  of the liner can also be examined theoretically using the model for the tuning coil. In this case, the same liner bulk modulus is used, but the  $\tan \delta$  is varied by modifying the imaginary part of the modulus for a fixed gap width. Figure 7-4 shows the transmission loss for GR23 461-663 at 6.9 MPa for a gap width of 1 mm and  $\tan \delta$  values of 0.0, 0.2, and 0.4. The results here are more clear-cut: increasing the damping lowers the peak  $TL$  values and raises the troughs while the resonant frequencies remain the same. The damping with a  $\tan \delta$  of 0.0 is still finite due to the viscous effects in the gap, but the effect is exaggerated when liner damping is included. From a design perspective, even though the peak  $TL$  is diminished, there is a higher bandwidth from raising the troughs: for the  $\tan \delta$  value of 0.4 the  $TL$  is a

minimum of 5 dB above 450 Hz. This value shifts higher with thinner liners due to the increase in branch volume velocity at the expense of effective speed of sound.

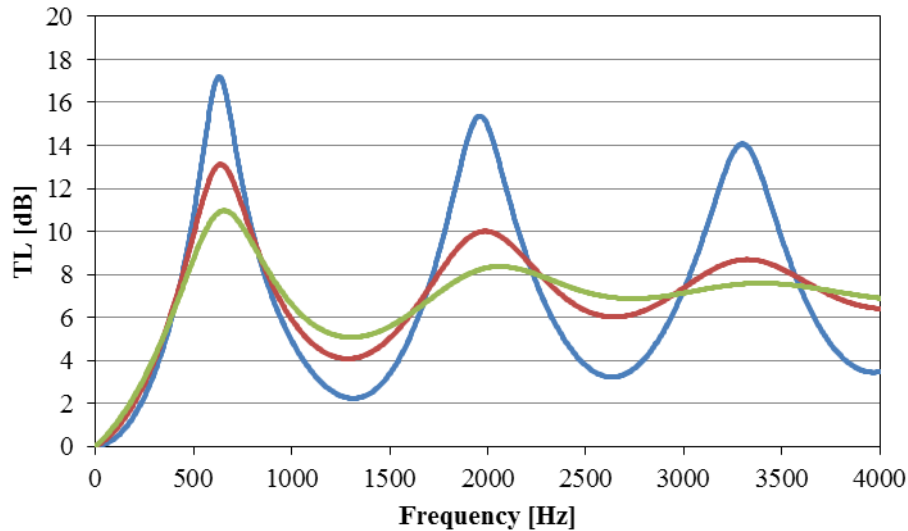


**Figure 7-4: Predicted transmission loss of a tuning coil with GR23 461-633 at 23.3 C at 6.9 MPa, a gap width of 1 mm, and a  $\tan \delta$  of — 0.0, — 0.2, and — 0.4.**

## 7.2 Modeling – Herschel-Quincke Tube

A theoretical model of a Herschel-Quincke (HQ) tube is developed in a similar manner as the tuning coil in the previous section. Furthermore, since a Herschel-Quincke tube has its first resonant mode at twice the frequency of a similarly-sized tuning coil, it is less useful from the standpoint of constructing compact devices for the reduction of fluid-borne noise for fluid power systems. An exception to this may be that it is more broad-band than a tuning coil, however, if such is the case an in-line silencer is likely more appropriate. Therefore, only a theoretical study of the effect of a compliant liner on the performance of a Herschel-Quincke tube is presented, and informed by estimated material properties from the Helmholtz resonator experiments.

A model for a Herschel-Quincke tube was also presented by Hastings and Chen in the papers mentioned previously [26, 36]. The development of the model here follows in

a like fashion, using the methods of D'Souza and Oldenburger [78] and Washio and Konishi [79] to describe the motion of a plane wave in either a pipe or an annular cylindrical tube. As with the tuning coil, the effect of a syntactic foam liner is included which modifies the compliance, and thus the speed of sound, of the branch. A schematic of the device considered is shown in Figure 7-5 which includes the port numbering.

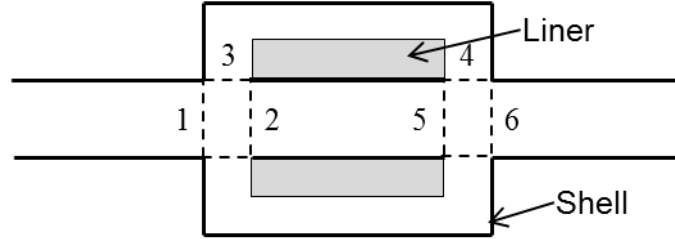


**Figure 7-5: Schematic of a Herschel-Quincke tube with a compliant liner.**

Transfer matrices are used to represent the propagation in the main flow path and the annulus as in Equation (6.1) and Equation (6.6), but are now subject to a modified set of boundary conditions. The condition of velocity identical to zero at the end of the annular section is replaced by a superposition of the velocity in the flow path and annulus equal to that at the port. The boundary conditions are

$$\begin{aligned} P_1 &= P_2 = P_3 \\ Q_1 &= Q_2 + Q_3 \end{aligned} \quad (6.22)$$

at the upstream junction and

$$\begin{aligned} P_4 &= P_5 = P_6 \\ Q_6 &= Q_4 + Q_5 \end{aligned} \quad (6.23)$$

at the downstream junction. Through the boundary conditions the transfer matrices are manipulated to arrive at

$$\begin{pmatrix} P_6 \\ Q_6 \end{pmatrix} = \mathbf{T} \begin{pmatrix} P_1 \\ Q_1 \end{pmatrix} \quad (6.24)$$

where matrix  $\mathbf{T}$  is

$$\mathbf{T} = \frac{1}{a_{12} + b_{12}} \begin{bmatrix} a_{11}b_{12} + a_{12}b_{11} & a_{12}b_{12} \\ (a_{21} + b_{21})(a_{12} + b_{12}) + (b_{22} - a_{22})(a_{11} - b_{11}) & a_{22}b_{12} + a_{12}b_{22} \end{bmatrix} \quad (6.25)$$

and where the variables  $a_{ij}$  and  $b_{ij}$  correspond to the appropriate terms in matrices

$$a_{ij} = \begin{bmatrix} \cosh(\Gamma_1 L) & -\frac{Z_{c1}}{\pi r_1^2} \sinh(\Gamma_1 L) \\ -\frac{\pi r_1^2}{Z_{c1}} \sinh(\Gamma_1 L) & \cosh(\Gamma_1 L) \end{bmatrix} \quad (6.26)$$

and

$$b_{ij} = \begin{bmatrix} \cosh(\Gamma_2 L) & -\frac{Z_{c2}}{\pi(r_5^2 - r_4^2)} \sinh(\Gamma_2 L) \\ -\frac{\pi(r_5^2 - r_4^2)}{Z_{c2}} \sinh(\Gamma_2 L) & \cosh(\Gamma_2 L) \end{bmatrix}. \quad (6.27)$$

As before, the speed of sound in the main flow path ( $c_1$ ) is a function of the bulk modulus of the fluid and its density, while the speed of sound in the annular section is a function of the effective bulk modulus described in Equation (6.10). The attenuation terms, propagation constants, and impedances are likewise identical. To compute the transmission loss, the transfer matrix  $\mathbf{T}$  in Equation (6.25) is inverted, and the elements of the resulting matrix are substituted into the equation for transmission loss,

$$TL = 20 \log_{10} \left[ \frac{1}{2} \left| t_{11} + \frac{t_{12}}{Z_0} + Z_0 t_{21} + t_{22} \right| \right]. \quad (6.28)$$

### 7.2.1 Parameter Study

The behavior of a Herschel-Quincke (HQ) tube is more complex than for either the Helmholtz resonator, which is a simple second-order system, or a tuning coil, which exhibits clear resonances at odd-numbered harmonics. The additional junction permits further standing wave effects in both the main flow path and annulus, and the resulting  $TL$  no longer resembles a simple side-branch resonator. For an initial study of behavior,

the  $TL$  for a HQ tube is plotted for pressures from 2.1 to 21 MPa in Figure 7-6. The performance at low pressures, relative to pressures of 5.5 MPa and above, is clearly superior, with at least 20 dB of  $TL$  above approximately 350 Hz. The pressure-stiffening behavior is evident in the location of the first resonant peak: for 3.4 MPa, this is at approximately 715 Hz, at 1215 Hz for 5.5 MPa, and at 1550 Hz for 6.9 MPa. For the 2.1 MPa case, the effective speed of sound in the branch is 140 m/s. Half-wave resonator theory provides two conditions that predict the frequencies of phase interference effects [40]: first, when

$$\phi_1 = \frac{2\pi fL}{c_p} \left( \frac{c_p}{c_b} - 1 \right) = (2n-1)\pi \quad (6.29)$$

where  $L$  is the length of the path (in this case for simplicity, assumed equal for the branch path and main path),  $c_p$  is the speed of sound in the pipe,  $c_b$  is the speed of sound in the branch, and  $n=1,2,\dots$ . The second condition is when

$$\phi_2 = \frac{2\pi fL}{c_p} \left( \frac{c_p}{c_b} + 1 \right) = 2n\pi. \quad (6.30)$$

Between these two conditions, the density (in frequency) of the standing wave modes within the device can be high, especially for large ratios of  $c_p/c_b$ . In particular, however, from Equation (6.29), when  $n=7$ , the frequency of the interference condition is 2288 Hz, which correlates closely with the peak observed in the  $TL$  at 2.1 MPa. Since the frequency of this peak is a function of the speed of sound ratio, manipulating the waveguide compliance can control the frequency of this and other resonances to achieve high  $TL$  as desired. Figure 7-7 shows the  $TL$  for GR23 461-663 for varying gap

thicknesses, all at 2.1 MPa. Since both damping and compliance are affected by gap thickness, the peak  $TL$  values shift both in amplitude and in frequency.

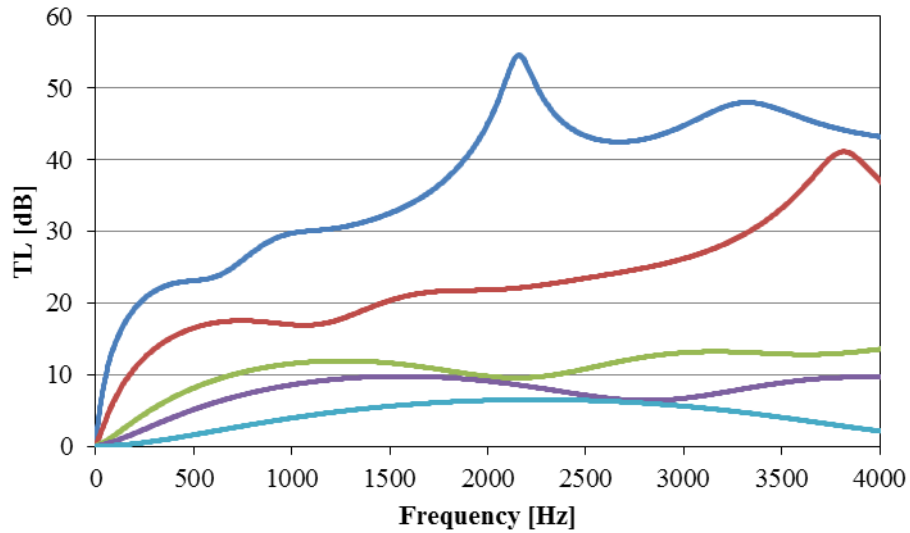


**Figure 7-6:** Predicted transmission loss of a Herschel-Quincke tube with a GR23 461-663 liner at pressures of — 2.1 MPa, — 3.4 MPa, — 5.5 MPa, — 6.9 MPa, and — 21 MPa.

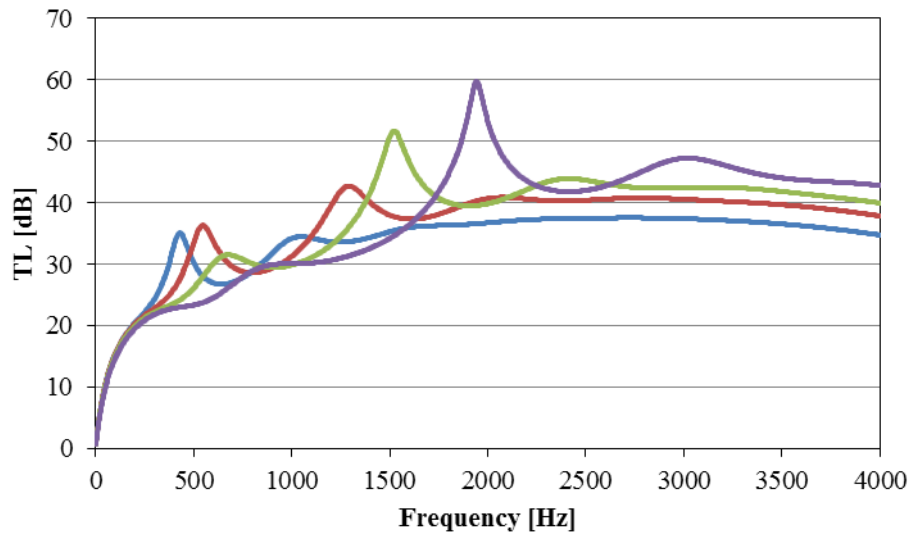


**Figure 7-7:** Predicted transmission loss of a Herschel-Quincke tube with a GR23 461-663 liner at gap thickness of — 1 mm, — 1.5 mm, — 2 mm, and — 3 mm.

The preceding figures and discussion regarding the performance of HQ tubes using liner GR23 461-663 used the complex Young's modulus of the liner in the model,

which has a  $\tan \delta$  value of 0.66 at this pressure. In Figure 7-7, the liner properties were unmodified. Figure 7-8 shows the  $TL$  for the HQ tube with varying liner  $\tan \delta$ , using the same real value of the Young's modulus. For the case of no liner damping, or a  $\tan \delta$  of 0.0, the  $TL$  does not return to zero because of the presence of viscous losses in the device. At increasing values of  $\tan \delta$ , the low frequency behavior is unaffected up to 350 Hz, after which the  $TL$  progressively increases. It may also be predicted from Equations (6.3) and (6.8) that for high levels of damping, a resonant structure to the  $TL$  would not be observed: acoustic energy incident on the upstream port (location 3 in Figure 7-5) and propagating into the branch would be dissipated before reaching the downstream port (location 4 in Figure 7-5).

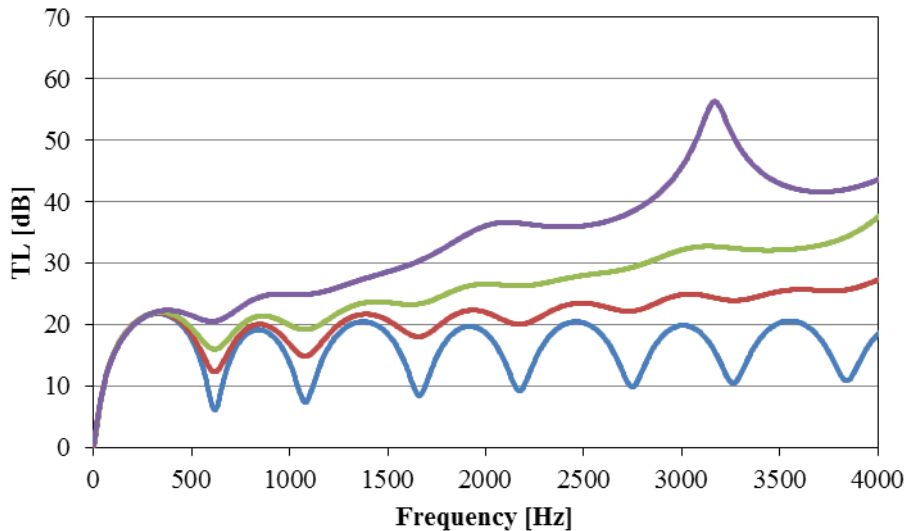


**Figure 7-8: Predicted transmission loss of a Herschel-Quincke tube with a GR23 461-663 liner at  $\tan \delta$  of — 0.0, — 0.1, — 0.2, and — 0.4.**

### 7.3 Experimental Results

This section presents experimental results for the prototype tuning coil in comparison to the theoretical model. The prototype tuning coil was constructed according to the schematic in Figure 5-5 and the dimensions in Table 7, and a photograph of the

device was shown in Figure 5-6. The tuning coil was tested in the experimental test rig discussed in Section 5.5 at approximately 22 C from 2.1-21 MPa, using liner GR9-625. The model uses an interpolated Young's modulus based on the cavity temperature from the experiment for a given pressure, with the real and imaginary parts of the modulus interpolated separately. Moreover, the model accounts for the dimensions of the liner at the given pressure, along with the temperatures from the experiment, and calculates the  $TL$  for the tuning coil. This data is then overlaid on the experimentally-obtained  $TL$  at the same conditions to evaluate the fit and study the behavior.

### 7.3.1 Comparison to Model

The transmission loss simulation of the tuning coil with liner GR9-625 at 2.1, 4.8, and 6.9 MPa is shown with experimental data in Figure 7-9, Figure 7-11, and Figure 7-12 at approximately 23 C for each pressure. The fluctuations in the transmission loss at frequencies from 3-4 kHz in each of these cases, along with some features at lower frequencies, are non-physical artifacts in the data. While the frequency-dependent nature of the  $TL$  from 3-4 kHz appears to have the same behavior as might be expected in a tuning coil, at least two factors indicate otherwise: the periodicity of these fluctuations does not match what would be expected given the size and compliance of the device, and the periodicity does not change with pressure, which would be expected given the pressure-dependent nature of the material properties. A relationship has been found empirically that roughly predicts the frequencies of features identified as artifacts:

$$\left| \arctan\left(\frac{BD}{AC}\right) \right| \approx 0 \quad (6.31)$$

where  $A$ ,  $B$ ,  $C$ , and  $D$  are the calculated complex wave amplitudes. A plot of the function on the left-hand side of Equation (6.31) for the TL of liner GR9-625 at 2.1 MPa and 22.5 C is shown as Figure 7-10. The frequencies where this function is close to zero may be such non-physical artifacts. The data points at the frequencies corresponding to the 30 smallest local minima in this function in Figure 7-9 and for the  $TL$  data in all figures following Figure 7-10 are encircled to indicate what features in the  $TL$  may not be physical. It should be noted that this is a necessary, but not sufficient condition to which frequencies may be artifacts.

In Figure 7-9, the frequency of the first resonant peak in the model underestimates the first resonance in the experimental  $TL$  by about 25%: the model predicts a peak  $TL$  at 185 Hz compared to approximately 253 Hz in the model. The peak  $TL$  of the model, however, is within 1 dB of the experiment. Given that the peak  $TL$  fits within 1 dB, it is most likely the case in Figure 7-9 that the  $\tan \delta$  in the model is accurate. From the parameter study in Section 7.1.1, the resonant frequency is a function of both the real part of the elastic modulus of the liner and the gap thickness. Since the resonant frequency of the model in Figure 7-9 is too low, the model is over-estimating the compliance, thus either the bulk modulus of the material is too low or the liner dimensions are inaccurate. It is also possible that the model for waveguide compliance is incorrect – the assumption made in the design of the annulus and in the model is that the liner does not shrink to the extent that it becomes constrained on the annulus at the given pressure. Using Equation (3.24) for the waveguide compliance, which represents the case where the liner is constrained on the annulus, reflects the experimentally-observed behavior more accurately. The model and experiment for this case at 4.8 MPa is shown in Figure 7-13.

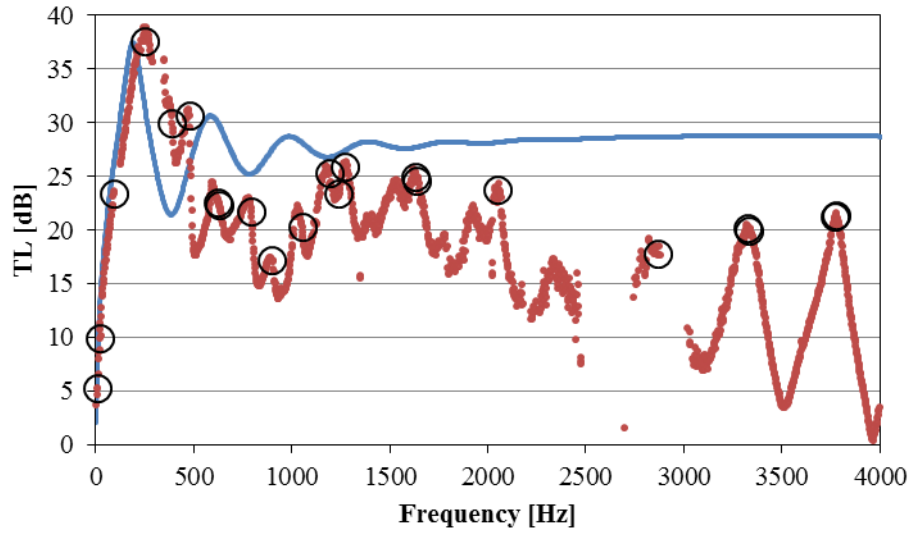


Figure 7-9: Measured transmission loss of tuning coil with GR9-625 at 2.1 MPa and 22.5 C, — model, ● experiment, ○ frequencies of possible artifacts.

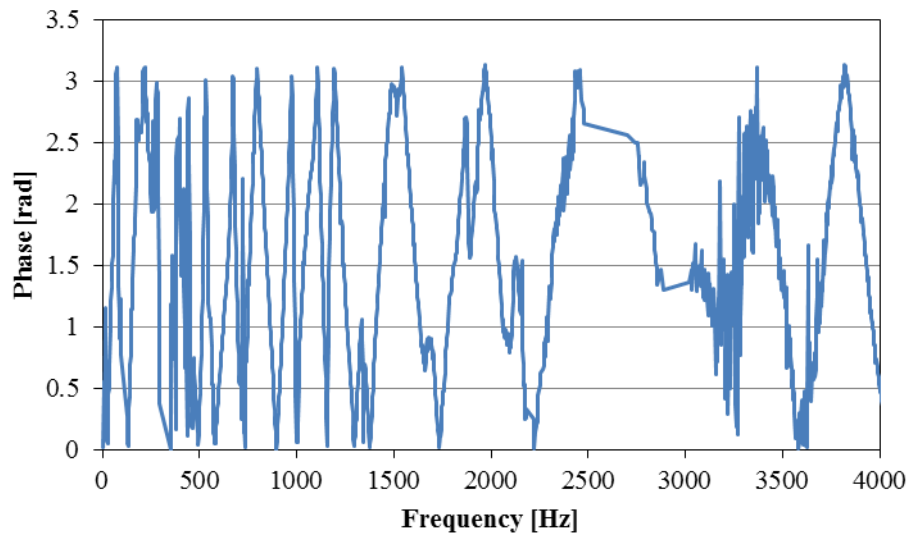


Figure 7-10: Plot of the phase condition, Equation (6.31), where points near 0 may indicate frequencies of artifacts in experimental data.

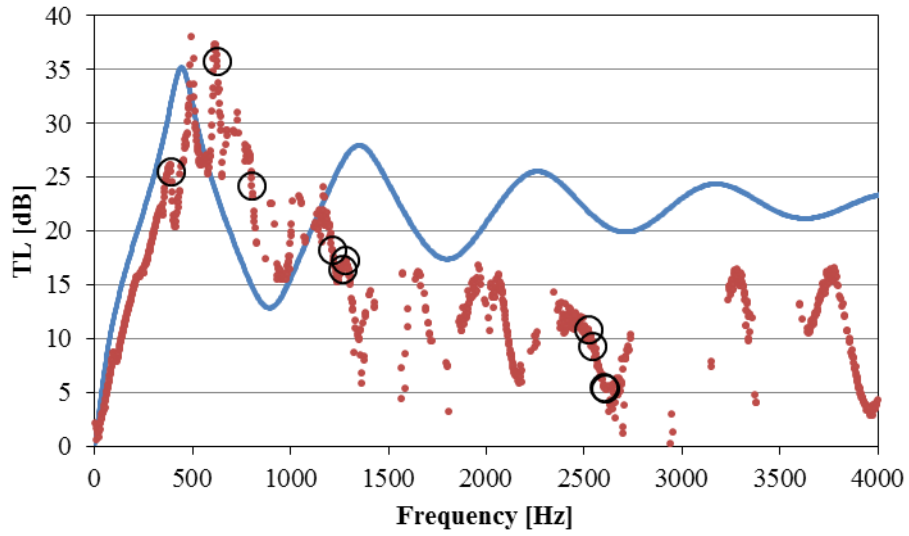


Figure 7-11: Measured transmission loss of tuning coil with GR9-625 at 4.8 MPa and 22.8 C, — model, • experiment, ○ frequencies of possible artifacts.

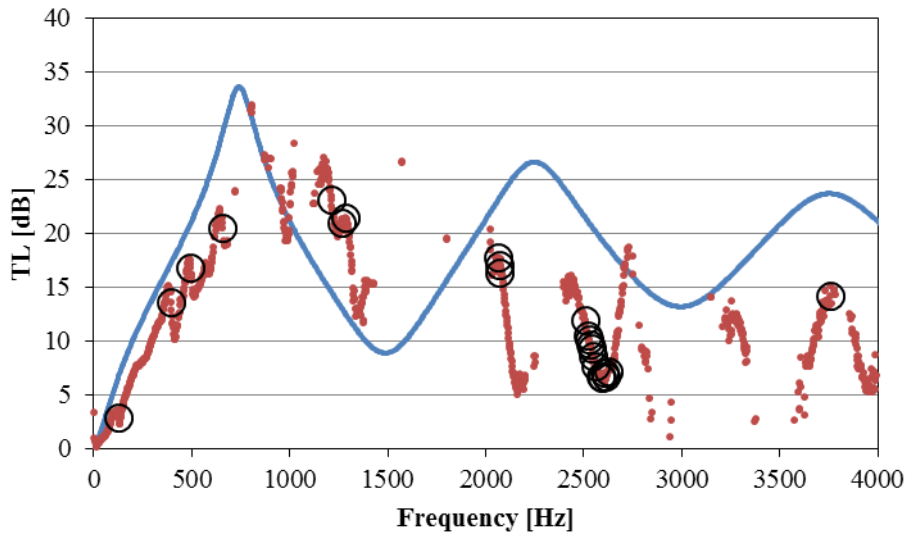
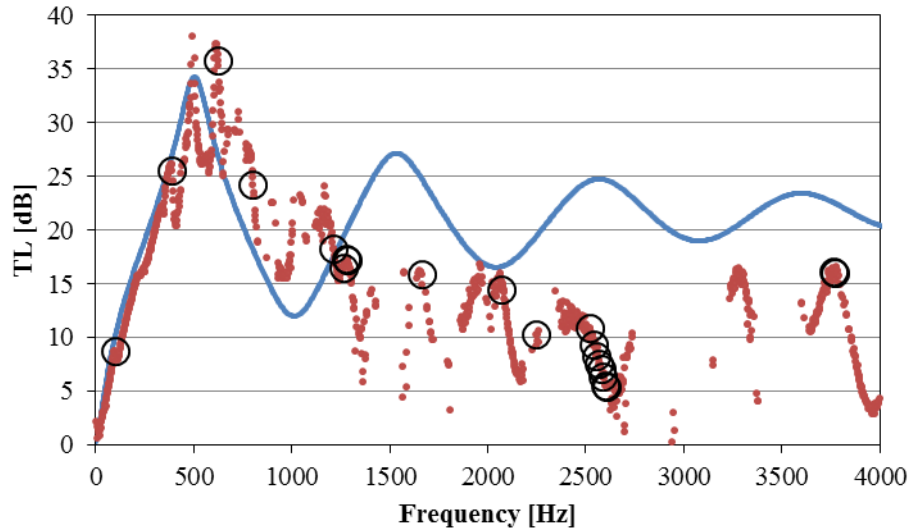


Figure 7-12: Measured transmission loss of tuning coil with GR9-625 at 6.9 MPa and 23.1 C, — model, • experiment, ○ frequencies of possible artifacts.



**Figure 7-13: Measured transmission loss of tuning coil with GR9-625 at 4.8 MPa and 23.1 C with a modified waveguide compliance, — model, • experiment, ○ frequencies of possible artifacts.**

For the transmission loss of all three of the pressures considered for GR9-625, the simulated  $TL$  at frequencies higher than the first resonant peak do not match the experimental data. The transmission loss calculated by the model fluctuates about a mean value that, for these cases, is between 15 dB and 25 dB. In the model of a tuning coil, this finite damping at higher frequencies is a result of acoustic energy incident on the throat from the main path coupling well with higher-order modes in the cavity. These higher-order modes are subject to attenuation from both viscous flow and material damping, thus some of the acoustic energy incident on the device is damped, thus not reflected, leading to a finite transmission loss. The question is then raised whether a tuning coil model is the most appropriate model for the prototype device given the experimental data. The next section will explore the fit of the Helmholtz resonator model to the experimental  $TL$  for the tuning coil prototype.

### 7.3.2 Resonator Model

The Helmholtz resonator model was modified to reflect the dimensions of the prototype tuning coil. Three key changes are made to the model: the length of the shell is longer than the prototype Helmholtz resonator, and the length and width of the neck are calculated based on the openings in the throat of the tuning coil. Figure 5-6 is a photograph of the tuning coil prototype which shows the openings that comprise the throat of the tuning coil. The sum of these openings are considered to be the resonator neck, where the total cross-sectional area of the openings is used along with the depth of the openings to represent the area and length of the neck. The results of the model are plotted with the experimental transmission loss for the same three conditions in the previous section: the GR9-625 liner at approximately 22 C at 2.1, 4.8, and 6.9 MPa. As in the previous section, the Young's modulus of the material is interpolated for the given temperature at each pressure. For all three pressures, both the resonant frequency and the peak *TL* of the model matches almost exactly, but more significantly, the resonator model more accurately reflects the behavior at higher frequencies where the experimental *TL* trails off gradually, approaching zero.

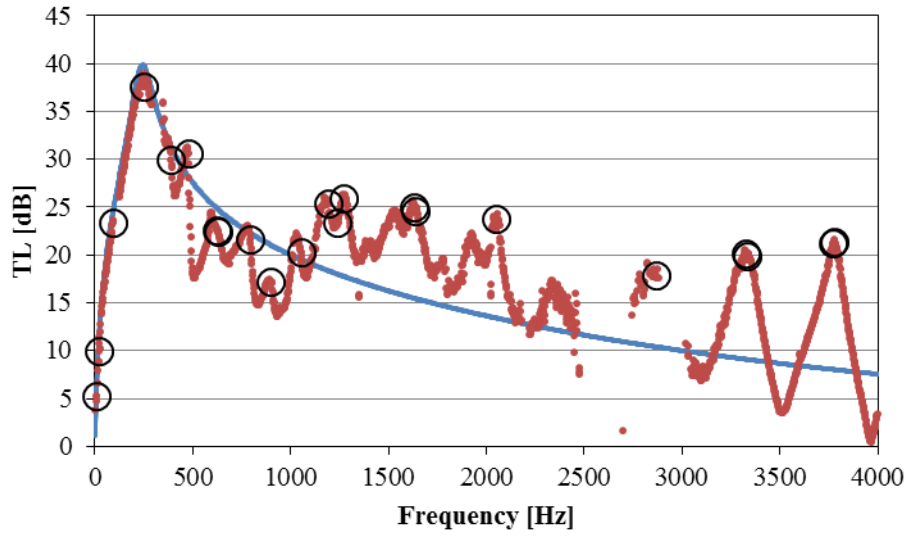


Figure 7-14: Measured transmission loss of tuning coil with GR9-625 at 2.1 MPa and 22.5 C, — Helmholtz resonator model, • experiment, ○ frequencies of possible artifacts.

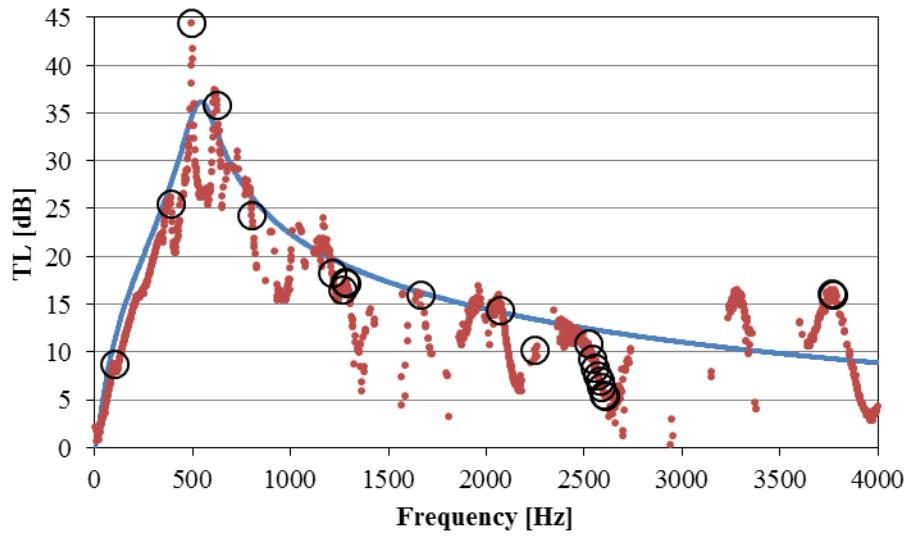


Figure 7-15: Measured transmission loss of tuning coil with GR9-625 at 4.8 MPa and 22.8 C, — Helmholtz resonator model, • experiment, ○ frequencies of possible artifacts.

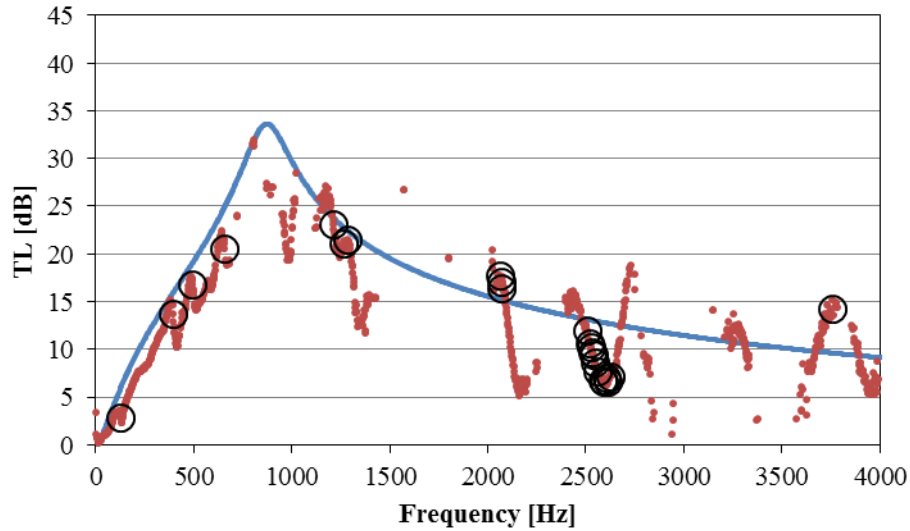


Figure 7-16: Measured transmission loss of tuning coil with GR9-625 at 6.9 MPa and 23.1 C, — Helmholtz resonator model, ● experiment, ○ frequencies of possible artifacts.

#### 7.4 Comparison to Commercial Devices

It is of interest to compare the performance of the prototype tuning coil, in the style of a concentric quarter-wave resonator, to the traditional and commercially-available type of tuning coil, which is a metal coil inserted in a hydraulic hose connected at one end. Of the papers that have studied these devices in the past, only a thesis by Way [80] has shown the experimental transmission loss of such a device, while others focus on the impedance parameters individually. It has been claimed in the literature that the viscous effects of leakage through the tuner have a strong effect on the performance, and likely outweigh resonance effects related to quarter-wave behavior [27].

A tuning coil and a hose, of identical dimensions and made of identical material but with no tuner, were acquired and tested in a modified version of the hydraulic test rig. Each device is 470 mm long and is made of hose with a 9.5 mm inner diameter. The tuner within the tuning coil is the coiled-metal type. The upper pressure and flow limits of the tuning coil were too low for the existing test rig to produce significant enough fluid-borne

noise to measure the performance of the device with sufficient coherence. Figure 7-17 shows a schematic of the modified rig, where ball valves have been installed between the needle valves at either end of the rig and a block with a piezoelectric stack has been installed immediately upstream of the test rig. A thin metal diaphragm keeps oil out of the housing that contains the stack, but under pressure remains in contact with the stack to maximize force transmission between the stack and fluid. The piezoelectric stack is connected to a power supply and a signal generator, and is driven by a sine sweep. The termination silencer, which is a commercially-available bladder-style hydraulic noise suppressor, is used to pressurize the rig in the following manner: the pump is turned on with the ball valves open, and the valve to the bladder in the silencer is opened; the hydrostatic pressure is turned up to 3.4 MPa, which is the current pressure limit of the piezoelectric stack and diaphragm configuration, at which point the bladder in the silencer is compressed against the inner wall of its shell; the valve to the bladder is closed, the pump is turned off, and the ball valves are closed; the valve to the bladder is then connected to a nitrogen tank, which is opened until the system pressure (measured at the static pressure sensors at either end of the component under test) reaches the desired value. Once the test rig is pressurized, the piezoelectric stack is excited with a sine sweep and transfer functions are captured as usual.

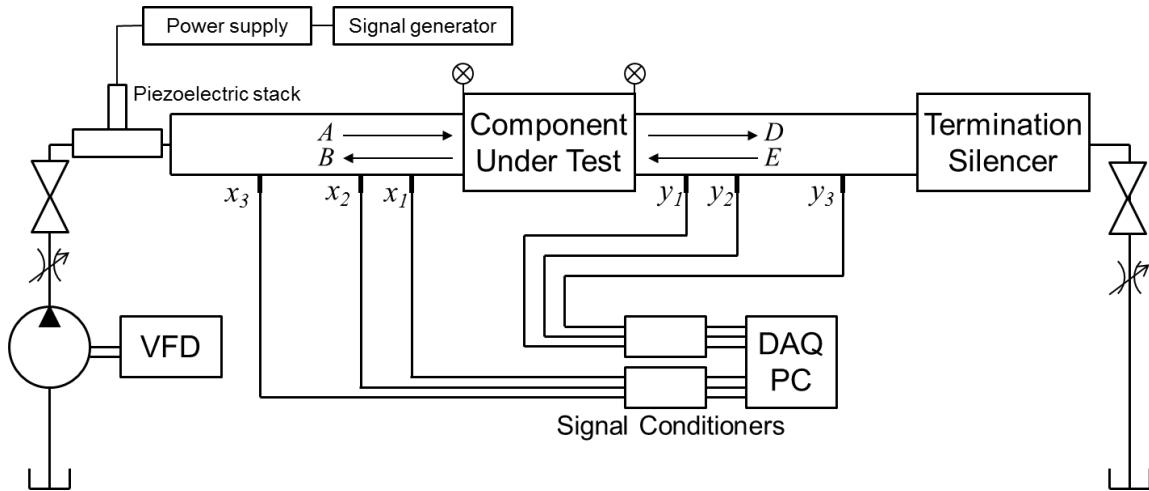


**Figure 7-17: Schematic of modified test rig using a piezoelectric stack to excite the system.**

The experimental results for the hose with no tuner are shown in Figure 7-18 for pressures of 1.4, 2.1 and 3.4 MPa. The diameter of the hose is quite small at 9.5 mm. The hose is both narrow diameter and was tested with oil at room temperature, so the fluid viscosity is relatively high and thus acoustic damping in the hose is expected to be significant. The static pressure loss in these devices is significant as well: testing with the pump at a flow rate of 14 L/min resulted in 0.5 MPa in static pressure loss across the device. The transmission loss increases steadily with frequency with an observable resonant peak at 550 Hz. The hose does show a slight pressure-stiffening behavior over this narrow range of pressures, which is consistent with it having an elastomeric liner. Likewise, the transmission loss of the hose containing a tuner is shown in Figure 7-19, and the performance of the hose with tuner to the hose at 3.4 MPa is shown in Figure 7-20. The hose with a tuner shows improved low-frequency *TL* compared to the hose and there is some resonant behavior observed: for instance, there are peaks in the *TL* at approximately 168 Hz, 289 Hz, and 384 Hz. Generally, however, the *TL* is very broadband, with at least 20 dB of *TL* above 260 Hz. This would not be expected in classic

quarter-wave behavior, where even-numbered modes in the branch result in low  $TL$ . Thus, the quarter-wave effect is likely not dominant and the viscous effects of leakage through the tuner have a more significant contribution to the  $TL$ , validating the claims of Drew [27]. Comparing the hose with a tuner to the hose with no tuner, in Figure 7-20, shows how the low-frequency performance is improved. The largest improvement in  $TL$  is at approximately 388 Hz, where the hose with tuner outperforms the hose without a tuner by 24.4 dB. The  $TL$  of the prototype tuning coil at 4.8 MPa is also shown in Figure 7-20 for comparison, and reveals that the prototype has equal or higher peak  $TL$  and similar performance up to 500 Hz, except for the resonant peaks in the commercial device at 200 and 400 Hz. The most significant shortcoming of the prototype device is the lack of  $TL$  above 700 Hz, however, the prototype device has a full-flow diameter port, while the hose, with and without the tuner, is of much smaller diameter.

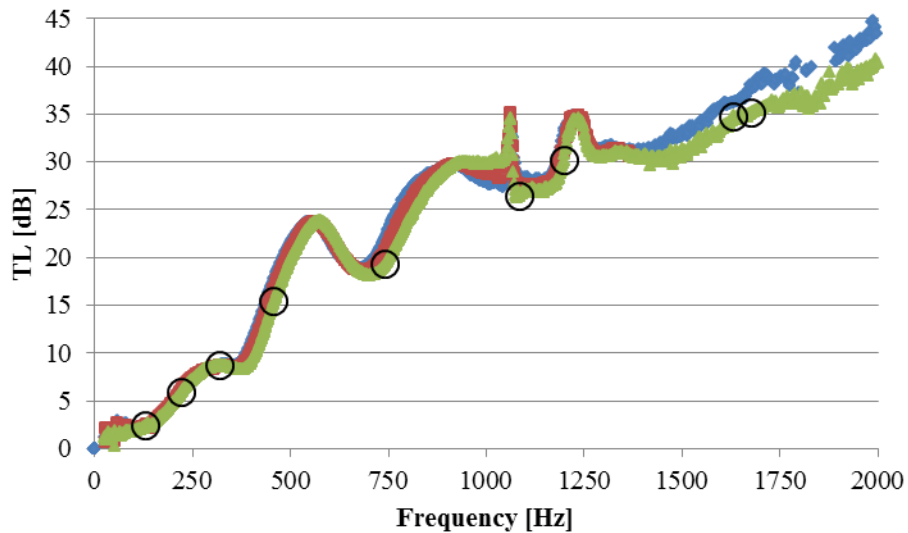


**Figure 7-18: Measured transmission loss of hydraulic hose at  $\blacklozenge$  1.4 MPa,  $\blacksquare$  2.1 MPa, and  $\blacktriangle$  3.4 MPa,  $\circ$  frequencies of possible artifacts.**

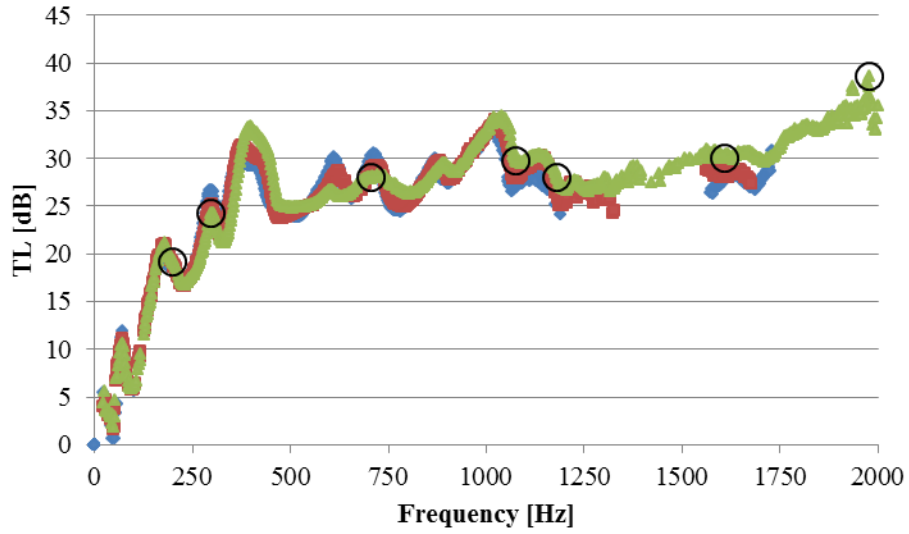


Figure 7-19: Measured transmission loss of commercially-available tuning coil at  $\blacklozenge$  1.4 MPa,  $\blacksquare$  2.1 MPa, and  $\blacktriangle$  3.4 MPa,  $\circ$  frequencies of possible artifacts.

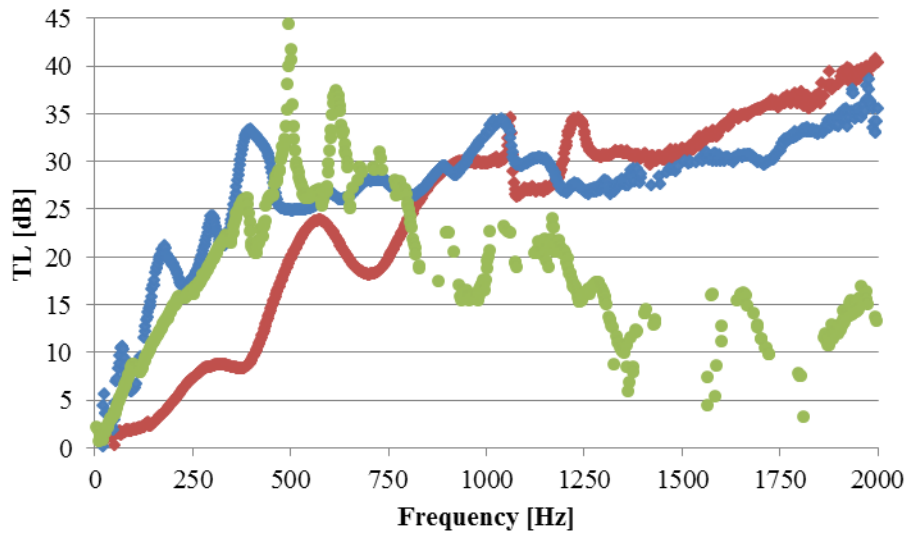


Figure 7-20: Measured transmission loss at 3.4 MPa of  $\blacklozenge$  tuning coil,  $\blacksquare$  hydraulic hose,  $\bullet$  prototype tuning coil.

## CHAPTER 8

### CONCLUSIONS AND FUTURE WORK

This section summarizes the findings of this research and presents a path for future work in this vein of study. In terms of findings, the material property study of the syntactic foam compared to neat urethane liner materials is discussed, as is the change in these properties as functions of temperature and pressure. The equations derived for the compliance of cavities and waveguides are discussed, as is the development of theoretical models for the tuning coil and Herschel-Quincke tube. The conclusions from the experimental evaluation of tuning coils, both the prototype and a commercially-available device are also presented. For future work, this section discusses both developmental issues and research questions. Developmentally, questions related to the manufacturability and durability of syntactic foam are posed. In terms of future research topics, questions regarding material properties and other embodiments of this material in hydraulic systems are discussed.

#### 8.1 Conclusions

This work has sought to characterize the performance of a syntactic foam lining in the context of traditional noise control components for hydraulic systems. It has been demonstrated that syntactic foam has a bulk modulus of up to four orders of magnitude less than neat urethane at 2.1 MPa: this leads to an increased compliance of two orders of magnitude, and yields the same physical effect of a pressurized bladder. This approach has the advantage of eliminating the maintenance requirements of a bladder by using a solid, compliant material. This results in a reduction in the volume of a Helmholtz

resonator by two orders of magnitude for the same resonance frequency. The bulk modulus for six different liner materials at three temperatures and eight pressures has been calculated using the transmission loss of a Helmholtz resonator coupled with a lumped-element model. In several ways, the liners behave as expected: they stiffen with increasing temperature and pressure consistent with the composition of the material post buckling of the material's integral microspheres. It has been found that the behavior of the material post-buckling is dominated by the physics of the buckled microspheres, essentially gas pockets, and is not consistent with the properties of the elastomer at atmospheric pressure. Instead of temperature-softening, the material is temperature-stiffening. A second-generation syntactic foam liner was developed that showed both deformation at a higher pressure and a delayed pressure-stiffening behavior at 33 C with respect to the first-generation syntactic foam with the same host material.

A number of equations have been derived, based on thick shell theory, which estimate the compliance of cavities and waveguides using different geometric configurations of a cylindrical liner. A liner that is unconstrained within a device has the highest compliance as it remains in a hydrostatic stress state: when the liner is constrained or bonded to the inside of a shell or outside of an annulus, the stress state is no longer hydrostatic and the compliance of the liner decreases. The equations derived are used in the theoretical models to calculate and predict the effect of the syntactic foam liner on classical noise control devices.

Theoretical models for a tuning coil and Herschel-Quincke tube have been constructed based on existing literature, but are modified to account for the presence of a compliant liner and use the equations derived for compliant waveguides. The compliance

of the liner has a dramatic effect on the frequency of the first resonance of the device, consistent with the reduction in the effective speed of sound in the branch determined by the compliance of the liner. The devices behave acoustically larger for the same physical size given a syntactic foam liner. Parameter studies for each device have also explored the role of the material damping in the transmission loss; increasing the  $\tan \delta$  of the liner reduces the peak  $TL$  but also raises the minimum  $TL$  past the first resonance which effectively raises the bandwidth of the device. As expected from the compliant waveguide equations derived in Chapter 4, the resonant frequency of the tuning coil or Herschel-Quincke tube is affected both by the bulk modulus and thickness of the liner. The theoretical model of a tuning coil fits the amplitude of the first resonant peak using the material properties determined in the study of Helmholtz resonators, but overestimates its compliance. Furthermore, higher-frequency behavior from the experiment does not exhibit quarter-wave behavior. However, fitting the Helmholtz resonator model to the experimental data better reflects the performance over a wide range of frequencies: this implies that the impedance of the throat of the tuning coil is too high relative to the impedance of the branch, resulting in poor coupling between higher frequencies in the main flow path and higher-order modes in the cavity. Finally, a commercially-available tuning coil was tested and compared to plain hose: the device performance was largely broad-band and dissipative and did not exhibit quarter-wave behavior. This confirmed claims from the literature regarding their performance.

It has been demonstrated that syntactic foam has very advantageous behavior regarding its use as a liner material for noise control devices for fluid power systems. It is compliant at elevated pressures relative to hydraulic fluid, thus permitting physically

smaller devices for the same performance. The material properties at elevated pressure and temperature have been calculated by solving the inverse problem using a Helmholtz resonator – these properties, when used in the theoretical model of a tuning coil match the experimental data of the prototype tuning coil closely up to the first resonance. It has been shown that syntactic foam linings can make classical noise control devices compact and effective for use in hydraulic systems.

## **8.2 Recommendations for Future Work**

This work has made inroads to the knowledge base necessary for complete investigation of syntactic foam linings for noise control devices for fluid power systems. Potential topics of future study are broken into four areas: investigation of syntactic foam material properties, manufacturing of syntactic foam, mechanical properties and the physics of microsphere collapse, and investigation of smart or active materials using syntactic foam.

### *8.2.1 Material properties*

The material properties of the constituent parts of the syntactic foam – polystyrene microspheres and a urethane host matrix – need to be understood in terms of several parameters. First, more precise laboratory experiments are necessary to determine the material properties at elevated temperatures and pressures, as well as versus frequency. While the inverse-solution used here may be sufficient for basic engineering purposes, more precise methods are needed for proper design. This work has been limited to a single elastic constant – the bulk modulus of the material – while assuming a constant Poisson's ratio at all strains in the material. This is most likely not true, but a

second elastic constant is unable to be uniquely determined by the method employed in this work and would require a different experimental arrangement to determine.

Second, the plasticization of each material by mineral oil at elevated pressures and temperatures is a concern for the practicality of the approach. Is the effect of plasticization significant, and does it enhance or diminish the performance? How does extended exposure to elevated temperatures or pressures affect this process? There is also the question of whether the mineral oil may penetrate the microsphere wall and fill the voids, rendering them incompressible.

### *8.2.2 Manufacturing and Development*

One issue encountered this work is the commercial availability of thick-walled microspheres. Most microspheres available on the market are relatively large and thin-walled with critical pressures much lower than what would be ideal from a hydraulics standpoint. Thus, some manufacturing questions arise when considering how to raise the critical pressure of available microspheres. For one, is it possible to mix unexpanded microspheres in with the hot urethane, such that they expand during mixture and curing? Knowledge of this process may be a way to get smaller, denser microspheres in the syntactic foam. Alternately, is it possible to have microspheres filled with a material other than isobutene or isopentane? For example, if they are filled with a highly compressible liquid, such as a refrigerant, they may still collapse but at a higher critical pressure.

With respect to the liners themselves, it may be of interest to develop functionally graded materials. That is, liners where the material properties change as a function of radius or length – this may be achieved by varying the volume fraction of microspheres,

the critical pressure of the microspheres, or the properties of the host material through one or more dimensions of the liner.

### 8.2.3 *Mechanical properties*

Many questions remain about the specific behavior of the microspheres in the syntactic foam as they collapse. How accurate is the critical buckling condition? Do the microspheres adhere to the urethane host, in such a way that their collapse may be affected? Is the collapse behavior hysteretic, and is the hysteresis significant enough to affect a device's liner which may be tuned close to this point? Furthermore, there are questions regarding the geometry of the liner in the cavity. Can a solid cylinder be used in the cavity instead of a hollow one, and how might this affect the acoustic radiation into the cavity from the neck?

### 8.2.4 *Smart/Active Materials*

This work has demonstrated the ability of a material's microstructure to effect large changes in compliance as a function of pressure. Given that a single material may have a single compliance-pressure curve, can this curve be modified such that the properties change for a given pressure? For example, magneto- and elasto-active or – rheological materials change properties, particularly stiffness, with exposure to an electric or magnetic field. Embedding iron particles within the material as it is cast may both increase the material losses and make it sensitive to exposed electric or magnetic fields. Thus, the cavity compliance and resonant frequency would change and could be made robust to changes in the system.

## APPENDIX A

### LINER DEFORMATION EQUATIONS

#### A.1 Liner Deformation

This derivation follows from Timoshenko's equations for a thick-shell cylinder under pressure [54]. First, a differential element drawn as an arc-shaped wedge in the plane perpendicular to the central axis of the cylinder is considered, as shown in Figure 8-1. Then, the forces are summed in the radial direction (the other two directions are trivial):

$$\sigma_r r d\varphi + \sigma_t dr d\varphi - \left( \sigma_r + \frac{d\sigma_r}{dr} dr \right) (r + dr) d\varphi = 0 \quad (\text{A.1})$$

where subscripts  $r$  and  $t$  are the radial and circumferential directions,  $\varphi$  is the angle of the differential element, and  $r d\varphi$  is the inner arc length. Equation (A.1) simplifies to

$$\sigma_t - \sigma_r - r \frac{d\sigma_r}{dr} = 0. \quad (\text{A.2})$$

Hooke's Law in three dimensions, in cylindrical coordinates, is written in terms of the stresses as

$$\sigma_r = \frac{3\beta}{1+\nu} \left[ (1-\nu) \frac{\partial u_r}{\partial r} + \nu \left( \frac{u_r}{r} + \frac{\partial u_z}{\partial z} \right) \right] \quad (\text{A.3})$$

$$\sigma_\theta = \frac{3\beta}{1+\nu} \left[ (1-\nu) \frac{u_r}{r} + \nu \left( \frac{\partial u_r}{\partial r} + \frac{\partial u_z}{\partial z} \right) \right] \quad (\text{A.4})$$

$$\sigma_z = \frac{3\beta}{1+\nu} \left[ (1-\nu) \frac{\partial u_z}{\partial z} + \nu \left( \frac{\partial u_r}{\partial r} + \frac{u_r}{r} \right) \right] \quad (\text{A.5})$$

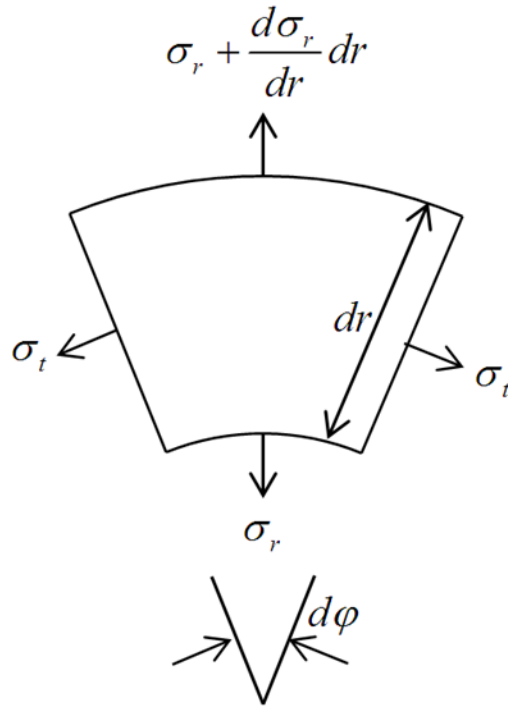


**Figure 8-1: Differential element in the cross-section of a thick shell.**

Equation (A.5) can also be written inversely as

$$\frac{\partial u_z}{\partial z} = \frac{1}{3\beta(1-2\nu)} [\sigma_z - \nu(\sigma_r + \sigma_t)]. \quad (\text{A.6})$$

Substituting Equation (A.3) and (A.4) into Equation (A.2) and cancelling terms yields the second order differential equation

$$\frac{d^2 u}{dr^2} + \frac{1}{r} \frac{du}{dr} - \frac{u}{r^2} = 0. \quad (\text{A.7})$$

The general solution to the PDE is

$$u(r) = C_1 r + \frac{C_2}{r}. \quad (\text{A.8})$$

where  $C_1$  and  $C_2$  are constants. The stresses are

$$\sigma_r = \frac{E}{1-\nu^2} \left[ C_1(1+\nu) - C_2 \frac{1-\nu}{r^2} \right] \quad (\text{A.9})$$

$$\sigma_t = \frac{E}{1-\nu^2} \left[ C_1(1+\nu) + C_2 \frac{1-\nu}{r^2} \right]. \quad (\text{A.10})$$

For the boundary conditions

$$(\sigma_r)_{r=b} = -p_o \quad (\text{A.11})$$

and

$$(\sigma_r)_{r=a} = -p_i \quad (\text{A.12})$$

corresponding to hydrostatic outer and inner pressure at the inner radius  $r = a$  and outer radius  $r = b$ , the constants of integration are

$$C_1 = \frac{(1-\nu)}{E} \frac{a^2 p_i - b^2 p_o}{b^2 - a^2} \quad (\text{A.13})$$

and

$$C_2 = \frac{(1+\nu)}{E} \frac{a^2 b^2 (p_i - p_o)}{b^2 - a^2}. \quad (\text{A.14})$$

With the boundary conditions in (A.11) and (A.12), the stresses become

$$\sigma_r = \frac{a^2 p_i - b^2 p_o}{b^2 - a^2} - \frac{a^2 b^2 (p_i - p_o)}{r^2 (b^2 - a^2)} \quad (\text{A.15})$$

and

$$\sigma_t = \frac{a^2 p_i - b^2 p_o}{b^2 - a^2} + \frac{a^2 b^2 (p_i - p_o)}{r^2 (b^2 - a^2)}. \quad (\text{A.16})$$

# APPENDIX B

## COMPUTER CODE

### B.1 Speed of Sound

```
%-----  
% User-Defined Function to Determine the speed of sound for a given  
% section of pipe  
%-----  
  
function [c] = SOS_func(omega,h01,h21,pipeprops,fluidprops,c0)  
  
% Pipe properties  
I01 = pipeprops.I01; % [m] distance between sensors 0 and 1  
I12 = pipeprops.I12; % [m] distance between sensors 1 and 2  
d = pipeprops.d; % [m] pipe inner diameter  
r0 = pipeprops.r0; % [m] pipe inner radius  
t = pipeprops.t; % [m] Wall thickness of the pipe  
Ew = pipeprops.Ew; % [Pa] Young's modulus of the steel pipe wall  
  
% Fluid properties  
visc = fluidprops.visc; % [m^2/sec] kinematic viscosity  
Df = fluidprops.Df; % [Pa] Bulk modulus of the hydraulic oil  
Rho = fluidprops.Rho; % [kg/m^3] Density of hydraulic oil  
  
% Script settings  
m = 1; % [ND] For loop index  
coher = 0.90; % [ND] value for coherence to be valid  
g = 0; % [ND] 1 = display graphics for SOS, 0 = no graphics  
  
% Determination of the velocity of the wave propagation pulsations  
% speed of sound) in a fluid enclosed by a homogeneous and straight  
% pipe using the three pressure transducer - method 1 - transducer 2  
% between 1 and 3  
% c final value speed of sound [m/s]  
% I01 distance between pressure transducers 1 and 2 [m]  
% I12 distance between pressure transducers 2 and 3 [m]  
% d inside diameter of the rigid pipe [m]  
% visc kinematic viscosity of the fluid at test conditions [m^2/s]  
% c0 initial chosen value of the speed of sound [m/2]  
% omega (2*pi*f) vector of individual freq. used in msmts [rad/sec]  
%  
% h01,h21  
% 2 dimensional matrices containing respectively, the transfer  
% functions P1/P2 and associated coherence; and P2/P1 and  
% associated coherence. that is h01(:,1) and h21(:,1) contain  
% the transfer function in complex number format and h01(:,2)  
% and h21(:,2) contain corresponding real number choerences.  
% These matrices are of the same length as the omega vector.  
%  
% coher min value for coherence for msmts to be valid (typ. .95)
```

```

% g      printing option (text and graphics on screen is g==1)

% Now must input the transfer function data in magnitude and phase form
% and convert it to complex notation to be passed to the function. Must
% do this for both workspaces imported into the m-file.

% ----- LOOKING FOR AVAILIABLE FREQUENCIES (coherence > min value)
nrc = 0; % Initialize the number of available frequencies

for nc = 1:length(omega)
    if (h01(nc,2) * h21(nc,2) >= coher*coher)
        nrc = nrc + 1;
        nv(nc) = 1; % Index the available frequencies
    else
        nv(nc) = 0; % Index the unavailable frequencies
    end
end

%-----BEGINING OF THE LOOP ALGORTIHM-----
a = omega + sqrt(2 * omega * visc) / d;
b = (4 * visc) / (d * d) + sqrt(2 * omega * visc) / d;

amjb = a - 1i*b;

I01xamjb = I01 * amjb;
I12xamjb = I12 * amjb;

ik = 1; % Initialize number of iterations of the algorithm

c = c0;
dc = 10;

while (abs(dc / c) > 0.0001)
    memc(ik) = c; % Memorize num of successive values for opt observations
    I01_ = I01xamjb / c;
    I12_ = I12xamjb / c;

    E = nv(:).*(sin(I12_).*h01(:,1)+sin(I01_).*h21(:,1)-sin(I01_+I12_));
    dEsurdc = nv(:).*amjb/(c*c).*(-I12*cos(I12_).*h01(:,1)-...
        I01*cos(I01_).*h21(:,1)+(I01+I12)*cos(I01_+I12_));

    dc = -sum(E .* conj(dEsurdc)) / sum(dEsurdc .* conj(dEsurdc));
    dc = real(dc); % real: force c to be real value
    c = abs(c + dc); % abs: force c to be positive value

%-----TEXT ON SCREEN-----
if (g == 1) && (ik == 1)
    fprintf('\nDetermination of Speed of Sound with ');
    fprintf('Coherence Imposed. %g\n', coher);
    fprintf('Number of Available Frequencies: ');
    fprintf('%g on %g maximum\n', nrc, length(omega));
    fprintf('c%g=%6.2f dc=%6.4f\n', ik, c0, dc);
else
    fprintf('c%g=%6.2f dc=%6.4f\n', ik, memc(ik), dc);
end

```

```

end

%-----WARNING MESSAGE-----
if (ik > 50)
    fprintf('Number of Iteration Values > 50\n');
    fprintf('Something is Wrong! Verify the Initial Values\n');
    return
end

ik = ik + 1;    % Increment the Number of Iterations
end

%-----CORRECTION TEST -----
%-----

% Need to see if the stiffness of the steel wall relative to the bulk
% modulus of the fluid is a small enough ratio to warrant correction of
% the bulk modulus of the fluid

Dc = Df / (1 + (d/2) / t * Df / Ew);

% Theoretical SOS:
ctheo = sqrt(Dc / Rho);

%-----GRAPHICS-----
fprintf('\nFinal Value of Speed of Sound = %6.0f m/s',real(c));
fprintf('\nTheoretical Value Speed of Sound = %6.0f m/s\n\n',...
    real(ctheo));

if (g == 1),
    np = 1:ik-1;
    plot(np, memc(np), '*w', np, memc(np));
    grid on;
    xlabel('Number of Iterations');
    ylabel('Speed of Sound [m/s]');
    title('Progression of the Algorithm');
    text(0.5, 0.5, ['Final Value = ', num2str(c)], 'sc');
end

```

## B.2 Transmission Loss

This script (or used as a function) calculates the transmission loss given transfer functions from an experiment.

```

%-----
% Program to Determine:
% - The speed of sound in hydraulic fluid
% - The reflection coefficient and apparent transmission loss (3-mic)
% - The transmission loss through transfer matrix parameters
% - May be ran either as a function or as a script
%-----

```

```

% function [header Freq phadiff Freq_TL TL] = TL_func(runname)
function [Freq_TL TL temp] = TL_func(runname,calset)

load(runname)

% clear all
% close all
% clc
%
% Uncomment the line for the directory with the files to process
% % newpath = '\2011-11-11 Data - No Lining 20C';
% % newpath = '\2011-09-17 Data - GR23-633 20C';
% % newpath = '\2011-09-20 Data - HRP(12)-545 45C';
% % newpath = '\2011-09-09 Data - GR23 461-663 45C';
% % newpath = '\2012-02-17 Data - HRP12 461-493 20C';
% % newpath = '\2012-04-06 Data - GR23 491-663 20C';
% newpath = '\2011-09-21 Data - GR23-633 HP 20C';
% % newpath = '\2012-04-06 Data - GR23 491-663 20C metal disc';
% path(path, [pwd,newpath])
%
% load run08
% calset = 2;
showplots = 0; % 1=Yes 0=No
coher = 0.95;

% PIPE PROPERTIES

I01 = 0.47; % [m] distance between sensors 0 and 1
I12 = 0.33; % [m] distance between sensors 1 and 2
I34 = 0.33; % [m] distance between sensors 3 and 4
I45 = 0.47; % [m] distance between sensors 4 and 5
d = 0.0206; % [m] pipe inner diameter
r0 = d / 2; % [m] pipe inner radius
t = 0.0087376; % [m] Wall thickness of the pipe
Ew = 210e9; % [Pa] Young's modulus of the steel pipe wall

pipepropsup=struct('I01',I01,'I12',I12,'d',d,'r0',d/2,'t',t,'Ew',Ew);
pipepropsdown=struct('I01',I34,'I12',I45,'d',d,'r0',d/2,'t',t,'Ew',Ew);

% FLUID PROPERTIES

temp_pipe = mean(TempArray0C(1:30));
temp_cavity = mean(TempArray0F(1:30));

visc = 164.52e-6*exp(-0.032*temp_pipe); % kinematic viscosity
c0 = 1400; % [m/s] initial speed of sound guess
Df = 1724e6; % [Pa] Bulk modulus of the hydraulic oil
Rho = 868; % [kg/m^3] Density of hydraulic oil

fluidprops = struct('visc',visc,'Df',Df,'Ew',Ew,'Rho',Rho);
lastrow = length(TF(:,1));

Freq = transpose(Freq);

```

```

omega = Freq(:,1)*2*pi; % [rad/sec] radial frequency interval vector

% CALIBRATE TRANSFER FUNCTIONS
[h01,h21,h31,h41,h51,h34,h54,ccup,ccacross,ccdown,cc] = ...
    CAL_func(TF,Power,coher,calset);

% COMPUTE SPEED OF SOUND
fprintf('Upstream SOS\n')
cu = SOS_func(omega,h01,h21,pipeprosup,fluidprops,c0);

fprintf('Downstream SOS\n')
cd = SOS_func(omega,h34,h54,pipepropsdown,fluidprops,c0);

% CALCULATE TRANSMISSION LOSS

% *****
%
% _____|_____|_____
% _____|_____|_____
% |         |         |         |         |         |
% 0         1         2         3         4         5
% x0        x1        x2        y0        y1        y2
%           x ----->|         |-----> y
%                   x=0       y=0
% *****

% 0.139 is the distance from the test section to the resonator neck

x2 = -0.275 - 0.139;
x1 = x2 - 0.33;
x0 = x1 - 0.47;

y0 = 0.275 + 0.139;
y1 = y0 + 0.33;
y2 = y1 + 0.47;

H01(1,1,:) = h01(:,1);
H11(1,1,1:lastrow) = 1;
H21(1,1,:) = h21(:,1);

H31(1,1,:) = h31(:,1);
H41(1,1,:) = h41(:,1);
H51(1,1,:) = h51(:,1);

zeta = 1 + sqrt(visc./(r0^2*1i*omega)) + visc./(r0^2*1i*omega);

ku(1,1,:) = (omega / cu) .* zeta;    kd(1,1,:) = (omega / cd) .* zeta;

Z0u = (Rho * cu * zeta) / (pi * r0^2);
Z0d = (Rho * cd * zeta) / (pi * r0^2);

```

```

z = zeros(1,1,lastrow);

A = [exp(-1i*ku*x2) exp(1i*ku*x2) z z;
     exp(-1i*ku*x1) exp(1i*ku*x1) z z;
     exp(-1i*ku*x0) exp(1i*ku*x0) z z;
     z z exp(-1i*kd*y0) exp(1i*kd*y0);
     z z exp(-1i*kd*y1) exp(1i*kd*y1);
     z z exp(-1i*kd*y2) exp(1i*kd*y2)];
e = [H21; H11; H01; H31; H41; H51];

xy = zeros(lastrow,4); % Rows 1:4 are waves A, B, D, and E respectively
condxy = zeros(lastrow,1);

for p = 1:lastrow
    xy(p,:) = transpose(pinv(A(:, :, p)) * e(:, :, p));
    condxy(p,:) = cond(A(:, :, p));
end

% Preallocate matrices
Freq_R = zeros(sum(ccup),1); R = Freq_R;
output_us = zeros(sum(ccup),4);

count = 1;
for ii = 1:lastrow
    if (ccup(ii) == 0);
    else
        Freq_R(count,1) = Freq(ii);
        % Silencer entrance reflection coefficient
        R(count) = xy(ii,2) / xy(ii,1);
        output_us(count,1:4) = [real(xy(ii,1)), imag(xy(ii,1)), ...
                                real(xy(ii,2)), imag(xy(ii,2))];
        count = count + 1;
    end
end

% Preallocate matrices
Freq_ds = zeros(sum(ccdown),1);
output_ds = zeros(sum(ccdown),4);

count3 = 1;
for ii = 1:lastrow
    if (ccdown(ii) == 0);
    else
        Freq_ds(count3,1) = Freq(ii);
        output_ds(count3,1:4) = [real(xy(ii,3)), imag(xy(ii,3)), ...
                                real(xy(ii,4)), imag(xy(ii,4))];
        count3 = count3 + 1;
    end
end

realR(:,1) = real(R);
imagR(:,1) = imag(R);
R2(:,1) = abs(R).^2; % Power reflection coefficient

Z = Rho*cu*((1 + R) ./ (1 - R)); % Silencer entrance impedance

```

```

% Generate the Transfer Matrix
p0 = xy(:,1) + xy(:,2); % Pressure at silencer entrance
q0 = (xy(:,1) - xy(:,2)) ./ Z0u; % Velocity at silencer entrance

pd = xy(:,3) + xy(:,4); % Pressure at silencer exit
qd = (xy(:,3) - xy(:,4)) ./ Z0d; % Velocity at silencer exit
% Velocity at silencer exit, different convention
% qd2 = (-y(:,1) + y(:,2)) ./ Z0d;

% pd = y(:,1);
% qd = y(:,1) ./ Z0d;

% Transfer matrix parameters
T11 = (pd .* qd + p0 .* q0) ./ (p0 .* qd + pd .* q0);
T12 = (p0.^2 - pd.^2) ./ (p0 .* qd + pd .* q0);
T21 = (q0.^2 - qd.^2) ./ (p0 .* qd + pd .* q0);
T22 = T11;

% T11 = (p0 .* qd + pd .* q0) ./ (pd .* qd + p0 .* q0);
% T12 = (p0 .* qd + pd .* q0) ./ (p0.^2 - pd.^2);
% T21 = (p0 .* qd + pd .* q0) ./ (q0.^2 - qd.^2);
% T22 = T11;

z11 = (pd.*qd - p0.*q0) ./ (qd.^2 - q0.^2); % = z22
z12 = (p0.*qd - pd.*q0) ./ (qd.^2 - q0.^2); % = z21

z11amp = abs(z11);
z11pha = angle(z11)*180/pi;
z12amp = abs(z12);
z12pha = angle(z12)*180/pi;

% Reflection coefficient at entrance of downstream pipe
Rd = xy(:,4) ./ xy(:,3);
% kd2 = (omega / cd) .* zeta;
% Termination silencer reflection coefficient
% Rt(:,1) = (y(:,2).*exp(-1i*kd2*Lp)) ./ (y(:,1).*exp(1i*kd2*Lp));
% Zt = Rho*cd*((1 + Rt) ./ (1 - Rt)); % Silencer entrance impedance
% Relationship btw C and D at downstream face of silencer under test
% Y(:,1) = abs(Rt .* exp(-2*1i*kd2*Lp));
% Y(:,1) = y(:,2) ./ y(:,1);

% Relative to amplitude of wave A
waveA = log10(abs(xy(:,1)) ./ abs(xy(:,1)));
waveB = log10(abs(xy(:,2)) ./ abs(xy(:,1)));
waveD = log10(abs(xy(:,3)) ./ abs(xy(:,1)));
waveE = log10(abs(xy(:,4)) ./ abs(xy(:,1)));

phaBA = angle(xy(:,2) ./ xy(:,1));
phaDC = angle(xy(:,4) ./ xy(:,3));
% diff = phaDC + phaBA;
waveratio = (xy(:,2).*xy(:,4)) ./ (xy(:,1).*xy(:,3));
phadiff = abs(angle(waveratio));

```

```

ccpha = ones(1,2560);%(phadiff < -.6) | (phadiff > .6);

Traveling_up = abs(xy(:,1) - xy(:,2).*exp(1i*phaBA));
Standing_up = abs(2*xy(:,2).*exp(1i*phaBA));

Traveling_down = abs(xy(:,3) - xy(:,4).*exp(1i*phaDC));
Standing_down = abs(2*xy(:,4).*exp(1i*phaDC));

% Preallocate matrices
Freq_TL = zeros(sum(cc),1); TL = Freq_TL; TL1 = Freq_TL; TL2 = Freq_TL;
TL3 = Freq_TL; TL4 = Freq_TL; TL_sd = Freq_TL;

count2 = 1;
for ii = 1:lastrow
    if (cc(ii) == 0) || (ccpha(ii) == 0)
    else
        Freq_TL(count2,1) = Freq(ii);

        T11(ii) = T11(ii) .* cc(ii);
        T12(ii) = T12(ii) .* cc(ii);
        T21(ii) = T21(ii) .* cc(ii);
        T22(ii) = T22(ii) .* cc(ii);

        t1 = sqrt(Z0d(ii)/Z0u(ii))*T11(ii);
        t2 = T12(ii)/sqrt(Z0u(ii)*Z0d(ii));
        t3 = sqrt(Z0u(ii)*Z0d(ii))*T21(ii);
        t4 = sqrt(Z0u(ii)/Z0d(ii))*T22(ii);

        % System-independent TL
        TL(count2,1) = 20*(log10((1/2)*abs(t1 + t2 + t3 + t4)));

        TL1(count2,1) = 20*log10((1/2)*abs(t1));
        TL2(count2,1) = 20*log10((1/2)*abs(t2));
        TL3(count2,1) = 20*log10((1/2)*abs(t3));
        TL4(count2,1) = 20*log10((1/2)*abs(t4));

        % System-dependent TL
        TL_sd(count2,1) = 20*log10((1/2)*abs(t1 + t2 + t3 + t4 + ...
            Rd(ii).*(t1 - t2 + t3 - t4)));

        count2 = count2 + 1;
    end
end

%
figure(6);subplot(3,1,1);plot(Freq_TL,TL1,Freq_TL,TL);subplot(3,1,2);...
.
%
plot(Freq_TL,TL2,Freq_TL,TL);subplot(3,1,3);plot(Freq_TL,TL3,Freq_TL,TL
)

% Transmission loss using impedance parameters
% TL_imped = 20*log10(0.5*abs(z11./z21 + z22./z21 + ...

```

```

%      (z11.*z22)./(z21.*Z0) + Z0./z21 - z12./Z0));%.* cc';

%% Typically Necessary Plot Commands

if showplots == 1;

    % Plot Power Spectra, Upstream Transfer Functions
    figure
    subplot(2,2,1)
    semilogy(Freq,Power1,Freq,Power2,Freq,Power3)
    grid on
    title('Power Vrms^2')
    legend('Power1','Power2','Power3')

    subplot(2,2,2)
    semilogy(Freq,Power4,Freq,Power5,Freq,Power6)
    grid on
    title('Power Vrms^2')
    legend('Power4','Power5','Power6')

    subplot(2,2,3)
    plot(Freq,TF(:,2),Freq,TF(:,3))
    grid on
    title('TF 0/1')
    legend('Real','Imag')

    subplot(2,2,4)
    plot(Freq,TF(:,5),Freq,TF(:,6))
    grid on
    title('TF 2/1')
    legend('Real','Imag')

    % Plot Coherence Vectors
    figure
    subplot(3,2,1)
    plot(Freq,coher1)
    grid on
    title('Coherence of TF 0/1')

    subplot(3,2,2)
    plot(Freq,coher2)
    title('Coherence of TF 2/1')
    grid on

    subplot(3,2,3)
    plot(Freq,coher3)
    title('Coherence of TF 3/1')
    grid on

    subplot(3,2,4)
    plot(Freq,coher4)
    title('Coherence of TF 4/1')
    grid on

```

```

subplot(3,2,5)
plot(Freq,coher5)
title('Coherence of TF 5/1')
grid on

subplot(3,2,6)
plot(Freq,coher6,Freq,coher7)
title('Coherence of TF 3/4, 5/4')
grid on

% Plot Reflection Coefficient
figure
plot(Freq_R,real(R),'.-',Freq_R,imag(R),'.-',Freq_R,abs(R),'.-')
grid on
xlabel('Frequency [Hz]')
title('Reflection Coefficient of Silencer Entrance')
legend('Real','Imag','Magnitude')

figure
plot(Freq_TL,TL,'.-')
grid on
xlabel('Frequency [Hz]')
ylabel('TL [dB]')
title('Transmission Loss')

figure
subplot(2,2,1)
plot(Freq,real(T11),Freq,imag(T11))
legend('Real','Imag')
title('T11')

subplot(2,2,2)
plot(Freq,real(T12),Freq,imag(T12))
legend('Real','Imag')
title('T12')

subplot(2,2,3)
plot(Freq,real(T21),Freq,imag(T21))
legend('Real','Imag')
title('T21')

subplot(2,2,4)
plot(Freq,real(T22),Freq,imag(T22))
legend('Real','Imag')
title('T22')

figure
plot(Freq,phadiff,Freq,zeros(1,length(Freq)))
end

%% Extraneous plot commands
% figure(5)

```

```

% subplot(2,2,1)
% plot(Freq,real(T11),Freq,imag(T11))
% title('T11')
% xlabel('Frequency [Hz]')
%
% subplot(2,2,2)
% plot(Freq,real(T12),Freq,imag(T12))
% title('T12')
% xlabel('Frequency [Hz]')
%
% subplot(2,2,3)
% plot(Freq,real(T21),Freq,imag(T21))
% title('T21')
% xlabel('Frequency [Hz]')
%
% subplot(2,2,4)
% plot(Freq,real(T22),Freq,imag(T22))
% title('T22')
% xlabel('Frequency [Hz]')
%
% figure(6)
% subplot(2,2,1)
% plot(Freq,real(z11),Freq,imag(z11))
% title('Z11')
% xlabel('Frequency [Hz]')
%
% subplot(2,2,2)
% plot(Freq,real(z12),Freq,imag(z12))
% title('Z12')
% xlabel('Frequency [Hz]')
%
% subplot(2,2,3)
% plot(Freq,real(z21),Freq,imag(z21))
% title('Z21')
% xlabel('Frequency [Hz]')
%
% subplot(2,2,4)
% plot(Freq,real(z22),Freq,imag(z22))
% title('Z22')
% xlabel('Frequency [Hz]')

% Clear unwanted variables

% clear coher1 coher2 coher3 coher4 coher5 coher6 coher 7
% clear Power1 Power2 Power3 Power4 Power5 Power6
% clear re1 re2 re3 re4 re5 re6 re7 im1 im2 im3 im4 im5 im6 im7
% clear Rate index loopindex

% Output Data
% output1 = [Freq2 realR imagR R2 real(ATL)];
% output3 = [real(T11) imag(T11) real(T12) imag(T12) real(T21)...
%           imag(T21) real(T22) imag(T22)];

% header = [Oil_Temp Liner_Temp];
temp = [temp_pipe temp_cavity];

```

```
% rmpath([pwd,newpath])
```

### B.3 Calibration

This function calibrates the transfer functions given the calibration data.

```
% Calibration function
```

```
function [h01,h21,h31,h41,h51,h34,h54,ccup,ccacross,ccdwn,cc] = ...  
    CAL_func(TF,Power,coher,calset)
```

```
switch calset  
    case 1  
        load calibration_final_rms  
    case 2  
        load calibration_final_rms2  
    case 3  
        load calibration_final_rms3  
end
```

```
% cal_TF (5994/5947, 5944/5947, 5966/5947, 5946/5947, 6537/5947,  
5966/5946, 6537/5946)  
% 0/1 2/1 3/1 4/1 5/1 3/4 5/4
```

```
load calibration_noise_rms  
% cal_noise_power
```

```
cal01(:,1) = cal_TF(:,2) + 1i*cal_TF(:,3);  
cal01(:,2) = cal_TF(:,4);  
cal21(:,1) = cal_TF(:,5) + 1i*cal_TF(:,6);  
cal21(:,2) = cal_TF(:,7);  
cal31(:,1) = cal_TF(:,8) + 1i*cal_TF(:,9);  
cal31(:,2) = cal_TF(:,10);  
cal41(:,1) = cal_TF(:,11) + 1i*cal_TF(:,12);  
cal41(:,2) = cal_TF(:,13);  
cal51(:,1) = cal_TF(:,14) + 1i*cal_TF(:,15);  
cal51(:,2) = cal_TF(:,16);  
cal34(:,1) = cal_TF(:,17) + 1i*cal_TF(:,18);  
cal34(:,2) = cal_TF(:,19);  
cal54(:,1) = cal_TF(:,20) + 1i*cal_TF(:,21);  
cal54(:,2) = cal_TF(:,22);
```

```
SNR_cal(:,1) = 10*log10(Power(:,1) ./ cal_noise_power(:,1));  
SNR_cal(:,2) = 10*log10(Power(:,2) ./ cal_noise_power(:,2));  
SNR_cal(:,3) = 10*log10(Power(:,3) ./ cal_noise_power(:,3));  
SNR_cal(:,4) = 10*log10(Power(:,4) ./ cal_noise_power(:,4));  
SNR_cal(:,5) = 10*log10(Power(:,5) ./ cal_noise_power(:,5));  
SNR_cal(:,6) = 10*log10(Power(:,6) ./ cal_noise_power(:,6));  
SNR_cal(:,6) = 10*log10(Power(:,7) ./ cal_noise_power(:,7));
```

```
SNR(:,1) = 10*log10(Power(:,1) ./ cal_noise_power(:,1));  
SNR(:,2) = 10*log10(Power(:,2) ./ cal_noise_power(:,2));  
SNR(:,3) = 10*log10(Power(:,3) ./ cal_noise_power(:,3));
```

```

SNR(:,4) = 10*log10(Power(:,4) ./ cal_noise_power(:,4));
SNR(:,5) = 10*log10(Power(:,5) ./ cal_noise_power(:,5));
SNR(:,6) = 10*log10(Power(:,6) ./ cal_noise_power(:,6));
SNR(:,7) = 10*log10(Power(:,7) ./ cal_noise_power(:,7));

% Assign matrices with the complex notation
h01(:,1) = TF(:,2) + 1i*TF(:,3); % 5994/5947
h01(:,2) = TF(:,4);
h21(:,1) = TF(:,5) + 1i*TF(:,6); % 5944/5947
h21(:,2) = TF(:,7);

h31(:,1) = TF(:,8) + 1i*TF(:,9);
h31(:,2) = TF(:,10);
h41(:,1) = TF(:,11) + 1i*TF(:,12);
h41(:,2) = TF(:,13);
h51(:,1) = TF(:,14) + 1i*TF(:,15);
h51(:,2) = TF(:,16);

h34(:,1) = TF(:,17) + 1i*TF(:,18);
h34(:,2) = TF(:,19);
h54(:,1) = TF(:,20) + 1i*TF(:,21);
h54(:,2) = TF(:,22);

% Calibrate
h01(:,1) = h01(:,1) ./ cal01(:,1);
h21(:,1) = h21(:,1) ./ cal21(:,1);
h31(:,1) = h31(:,1) ./ cal31(:,1);
h41(:,1) = h41(:,1) ./ cal41(:,1);
h51(:,1) = h51(:,1) ./ cal51(:,1);
h34(:,1) = h34(:,1) ./ cal34(:,1);
h54(:,1) = h54(:,1) ./ cal54(:,1);

lastrow = length(cal_TF(:,1));

for m = 1:lastrow
% Establish a matrix with the coherence info
    if (TF(m,4) < coher) || (TF(m,7) < coher) || (cal_TF(m,4) <
coher)...
        || (cal_TF(m,7) < coher)
        ccup(m,1) = 0;
    else
        ccup(m,1) = 1;
    end

    if (TF(m,10) < coher) || (TF(m,13) < coher) || (TF(m,16) < coher)
||...
        (cal_TF(m,10) < coher) || (cal_TF(m,13) < coher) ||...
        (cal_TF(m,16) < coher)
        ccacross(m,1) = 0;
    else
        ccacross(m,1) = 1;
    end

    if (TF(m,19) < coher) || (TF(m,22) < coher)
        ccdown(m,1) = 0;

```

```

else
    ccdown(m,1) = 1;
end
end
end

```

```
cc = ccup .* ccacross;
```

## B.4 Helmholtz Resonator

### B.4.1 Modeling Function

```

%%%%%%%%%%%%%%%%%%%%%%%%%%%%%%%%%%%%%%%%%%%%%%%%%%%%%%%%%%%%%%%%%%%%%%%%
% Code written to model hydraulic Helmholtz resonators
% Can be run as a function or as a script
%%%%%%%%%%%%%%%%%%%%%%%%%%%%%%%%%%%%%%%%%%%%%%%%%%%%%%%%%%%%%%%%%%%%%%%%

function [TL] = resonator_func(EI0,w)

global n Pm temp_cavity linernum ce wr nul Bf Bs Bl

% clear all
% close all
% clc
%
% % newpath = '\2011-09-15 Data - GR9 20C';
% newpath = '\2011-09-14 Data - GR9-625 20C';
% % newpath = '\2011-09-16 Data - GR23 45C';
% % newpath = '\2011-09-21 Data - GR23-633 HP 45C';
% % newpath = '\2011-09-09 Data - GR23 461-663 45C';
% % newpath = '\2011-09-19 Data - HRP(12) 45C';
% % newpath = '\2011-09-20 Data - HRP(12)-545 45C';
% % newpath = '\2012-02-17 Data - HRP(12) 461-493 45C';
% path(path,[pwd,newpath])
%
% % % Liner_Order =
% % linernum = 1; nul = 0.4995;% - GR9
% linernum = 2; nul = 0.45;% - GR9-625
% % linernum = 3; nul = 0.4995;% - GR23
% % linernum = 4; nul = 0.45;% - GR23-633
% % linernum = 5; nul = 0.4995;% - HRP(12)
% % linernum = 6; nul = 0.45;% - HRP(12)-545
% % linernum = 7; nul = 0.45;% - GR23 461-663
% % linernum = 8; nul = 0.45;% - HRP(12) 461-493
%
% n = 8;
%
% if n < 10
%     runnum = strcat('run0',num2str(n));
% else
%     runnum = strcat('run',num2str(n));
% end
%
% calset = 2;
% [Freq_TL, TL_exp(:,n), temp] = TL_func(runnum,calset);
% Freq = Freq_TL;

```

```

% temp_cavity(n) = temp(1); % [C]
% temp_pipe(n) = temp(2); % [C]
%
% rowmin = 1;%6; % Rows corresponding to frequencies of interest
% rowmax = 284;
% w = Freq*2*pi; % [rad/sec]
% w = w(rowmin:rowmax);
% Freq = w/2/pi;
% Pm = [300:100:1000 1500:500:3000]*6894.76; % [Pa]
%
% % Liner Young's modulus
% % E10 = [2e9 1e8]; % [Pa]
% [Elr,Eli] = interp(temp_cavity(n),n,linernum);
% % Eli = 0.6*Elr;

load Liner_Volume_Resonator.mat

% SHELL
Lr = 97.28 /1000; % [m] Inside length of shell
% r3 = 13.30 /1000; % [m] Inner radius of liner
r50 = 31.75 /1000; % [m] Inner radius of shell
r60 = 44.45 /1000; % [m] Outer diameter of cavity wall
Es = 210e9; % [Pa] Young's modulus of cavity wall (steel)
nus = 0.3; % [ND] Poisson's ratio of cavity wall (steel)

% Calculate r5 and r6 as functions of pressure
r5 = r50 + (Pm(n)*r50/Es)*((r60^2 + r50^2)/(r60^2 - r50^2) + nus);
r6 = r60 + (2*Pm(n)*r50^2*r60)/(Es*(r60^2 - r50^2));

Vc = Lr*pi*r5^2; % [m^3] Volume of cavity

% LINER
% E1 = Elr + li*Eli; % [Pa] Given bulk modulus estimate
E1 = E10(1) + li*E10(2);
Vl = Liner_Volume(n+3,linernum+2); % [m^3]
% ml = Liner_Mass(linernum)/1000; % [kg] Mass of liner

% FLUID
% Total volume of fluid
Vf = Vc - Vl;

% AIR
% ma = 1e-7; % kg
K = 1.4; % Specific heat ratio for air
% Ko = T_liner(n) + 273.15; % Temperature of air in Kelvin
% R = 287.04; % [J/kg*K] Specific gas constant for dry air
% Va = ma*R*Ko/Pm(n); % [m^3] Volume of air
% Ba = K*Pm(n); % [Pa] Bulk modulus of air
X0 = 0.00; % e.g.: .001 = 0.1%, .01 = 1%, .1 = 10%
P0 = 0.1e6; % [Pa] Atmospheric pressure
rhoa0 = 1.2; % [kg/m^3] Density of air at standard conditions
Va0 = Vf*X0; % [m^3] Volume of air at standard conditions
Va = Va0*(Pm(n)/P0)^(-1/K); % [m^3] Volume of air at pressure/temp
if Va ~=0
    rhoa = rhoa0*Va0/Va; % [kg/m^3] Density of air

```

```

elseif Va == 0
    rhoa = 0;
end

ma = rhoa*Va;

% OIL
visc_cavity = 178.4176*exp(-0.0344*temp_cavity(n)); % [cSt]
visc_cavity_si = visc_cavity*10^-6; % [Pa-s]
B0t = 10^(0.3766*(log10(visc_cavity))^(0.3307) - 0.2766); % [GPa]
At = -0.01382*temp_cavity(n) + 5.851; % [GPa/GPa]
Bpt = (B0t + At*(Pm(n)/1e9))*1e9; % [Pa]

Bf = (1 - X0 + X0.*(P0/Pm(n)).^(1/K))./...
    ((X0/(K*Pm(n)))*(P0/Pm(n))^(1/K) + (1 - X0)/Bpt);

rhoo = 915; % [kg/m^3] Density of hydraulic fluid
Vo = Vf - Va; % [m^3] Volume of oil
mo = Vo*rhoo; % [kg] Mass of oil
rhof = (mo + ma)/Vf; % [kg/m^3] Density of fluid
c = sqrt(Bf/rhof); % [m/s] Speed of sound in rigid pipe

% TEST PIPE
d = 0.0206; % [m] Diameter of pipe
rp = d/2; % [m] Radius of pipe
Sp = pi*rp^2; % [m^2] Area of pipe

% NECK
rn = 2.97 /1000; % [m] Radius of resonator neck
Ln = 37.34 /1000; % [m] Length of resonator neck
Sn = pi*rn^2; % [m^2] Area of resonator neck
Lneff = Ln + 1.7*rn; % [m] Effective length of neck
m = rhoo*Sn*Lneff; % [kg] Mass of fluid in neck

% The mass is fixed regardless of fr
L = m/Sn^2;

% Compute mechanical compliance of shell [Pa]
Bs = 1/((2/Es)*((r6^2 + r5^2)/(r6^2 - r5^2) + nus)); % [Pa]

% Compute compliance of cavity with compliant liner [Pa]
Bl = 1/((Vl*(3-4*nul))/(El*(Vc-Vl)));

% Net compliance of cavity (springs in series) C=V/B
C = Vf*(1/Bf + 1/Bl + 1/Bs);

ce = sqrt(Vf/(rhof*C)); % [m/s] Effective speed of sound in cavity
k = w/c; % [1/m] Wavenumber in fluid in neck
ke = w/ce; % [1/m] Effective wavenumber in cavity

% Calculate damping terms
% zeta is complex wavenumber in fluid in neck
zeta = k.*(1+sqrt(visc_cavity_si./(rn^2*li*w))+...
    visc_cavity_si./(rn^2*li*w));

```

```

% damping is the loss factor of the complex wavenumber of fluid in neck
alphaw = abs(imag(zeta) ./ real(zeta));

Rw = 2*m*w.*alphaw; % Viscous resistance
Rr = (rhoo*ce*ke.^2*Sn^2)/(2*pi); % Radiation resistance

% Calculate impedance of resonator
Rh = (Rw+Rr)/Sn^2;
Xh = w*L - 1./(w*C);
Zh = Rh + 1i*Xh;

[~, minind1] = min(abs(imag(Zh)));
wr = w(minind1);

% Calculate T-matrix terms
T11 = 1; T12 = 0; T21 = 1./Zh; T22 = 1;

% Impedance of connecting pipe
Z0 = (rhoo*c) / Sp;

% Calculate the transmission loss
TL = 20*log10(0.5*abs(T11 + T12/Z0 + Z0*T21 + T22));

% figure(n)
% plot(Freq,TL,Freq,TL_exp(rowmin:rowmax,n),'o')
% xlabel('Frequency [Hz]')
% ylabel('Transmission Loss [Hz]')
% legend('Model','Experiment')
%
% rmpath([pwd,newpath])

```

#### ***B.4.2 Least-Squares Code***

```

% Script to perform nonlinear least squares on Helmholtz Resonator
% model to find the complex bulk modulus of the liner

clear all
close all
clc

% newpath = '\2011-09-15 Data - GR9 45C';
% newpath = '\2011-09-14 Data - GR9-625 45C';
% newpath = '\2011-09-16 Data - GR23 20C';
% newpath = '\2011-09-21 Data - GR23-633 HP 20C';
% newpath = '\2011-09-09 Data - GR23 461-663 20C';
newpath = '\2011-09-19 Data - HRP(12) 20C';
% newpath = '\2011-09-20 Data - HRP(12)-545 20C';
% newpath = '\2012-02-17 Data - HRP12 461-493 20C';

path(path, [pwd,newpath])

global n Pm temp_cavity linernum ce wr nul Bf Bs Bl

```

```

calset = 2;

% % Liner_Order =
% linerenum = 1; nul = 0.4995;% - GR9
% linerenum = 2; nul = 0.45;% - GR9-625
% linerenum = 3; nul = 0.4995;% - GR23
% linerenum = 4; nul = 0.45;% - GR23-633
linerenum = 5; nul = 0.4995;% - HRP(12)
% linerenum = 6; nul = 0.45;% - HRP(12)-545
% linerenum = 7; nul = 0.45;% - GR23 461-663
% linerenum = 8; nul = 0.45;% - HRP(12) 461-493

set(0, 'DefaultFigureWindowState', 'docked')

cd([pwd,newpath])
numfiles = length(dir('run*.mat')); % Number of data files
cd ..

Pm = [300:100:1000 1500:500:3000]*6894.76; % [Pa]
% Pm = [300:100:1000]*6894.76; % [Pa]

for n = 1:numfiles
    if n < 10
        runnum = strcat('run0',num2str(n));
    else
        runnum = strcat('run',num2str(n));
    end

    if n < 8
        E10 = [1e10 0.5e10]; % Bulk modulus of liner initial guess [Pa]
    else
        E10 = [1e10 0.5e10]; % Bulk modulus of liner initial guess [Pa]
    end

    % Call the TL function to get the experimental data
    [Freq_exp, TL_exp(:,n), temp] = TL_func(runnum,calset);

    temp_cavity(n,1) = temp(1); % [C] Oil Temperature
    temp_pipe(n,1) = temp(2); % [C] Outside of liner temperature

    Linertemp = mean(temp_cavity);

    rowmin = 6; % Rows corresponding to frequencies of interest
    rowmax = 284;

    w = Freq_exp*2*pi; % [rad/sec]
    w_fit = w(rowmin:rowmax);

    % Run optimization function to find values of the bulk modulus that
    % will best fit the model to the experiment
    optns = optimset('TolFun',1e-9);
    [young(n,1:2), resnorm, residual, exitflag, output, lambda, jacobian]=...
        lsqcurvefit(@resonator_func,E10,w_fit,...

```

```

    TL_exp(rowmin:rowmax,n), [.01 .01], [1e15 1e15], optns);

    bulk(n,1) = real((young(n,1) + 1i*young(n,2))/(3*(1-2*nul)));
    bulk(n,2) = imag((young(n,1) + 1i*young(n,2))/(3*(1-2*nul)));

    TL_model(:,n) = resonator_func(young(n,1:2),w);

    % Calculate the peak value of TL, and the location of this value
    [peak_TL(n,1), index] = max(TL_model(:,n));

    % Calculate the frequency at which the TL peaks
    peak_Freq(n,1) = Freq_exp(index);

    % Calculate the locations of the bandwidth points
    [~, minind1] = min(abs(TL_model(1:index,n) + 3 - peak_TL(n,1)));
    [~, minind2] = min(abs(TL_model(index:length(TL_model(:,n)),n) ...
        + 3 - peak_TL(n,1)));
    minind2 = minind2 + length(TL_model(1:index));

    % Calculate the bandwidth from those frequency locations
    Bandwidth(n,1) = Freq_exp(minind2) - Freq_exp(minind1);

    % Calculate the quality factor
    Q_Factor(n,1) = peak_Freq(n,1) / Bandwidth(n,1);

    % Save the effective speed of sound
    c_eff(n,1) = real(ce);

    % Save the resonance frequency
    fr(n,1) = transpose(wr/2/pi);

    Bf_(n,1:2) = [real(Bf) imag(Bf)];
    Bs_(n,1:2) = [real(Bs) imag(Bs)];
    Bl_(n,1:2) = [real(Bl) imag(Bl)];

    % Plot each data set and its model fit
    figure(n)
    plot(w/2/pi, TL_model(:,n), Freq_exp(rowmin:rowmax), ...
        TL_exp(rowmin:rowmax,n), 'o')
    xlabel('Frequency [Hz]')
    ylabel('Transmission Loss [Hz]')
    legend('Model', 'Experiment')
    axis([0 ceil(Freq_exp(rowmax)) 0 16])
end

% Create a matrix to output the data to Excel
dataoutput = [temp_pipe temp_cavity fr peak_Freq peak_TL Bandwidth...
    Q_Factor c_eff bulk(:,1)/1e9 bulk(:,2)/1e9 bulk(:,2)./bulk(:,1)];

% Plot the bulk modulus and tan delta
figure
plotyy(Pm(1:numfiles), bulk(:,1), Pm(1:numfiles), ...
    atan(bulk(:,2)./bulk(:,1)))

```

```
xlabel('Static Pressure [Pa]')
ylabel('Storage Modulus [Pa]')

rmpath([pwd,newpath])
```

## B.5 Tuning coil

The code use to model the tuning coil is given in the following section. The code calls the function that calculates transmission loss (shown in Section B.2) for the purpose of comparing the model to experimental data.

### B.5.1 Modeling Function

```
%-----
% Code written to model hydraulic tuning coils. This code is written
% such that it can be run as a script or called as a function
%-----

% function [TL_model] = tuningcoil_func(vars,w)
%
% global n Pm T_oil nul

clear all
close all
clc

% newpath = '\2012-04-20 Data - GR9-625 New Termination';
% newpath = '\2012-09-22 Data - Empty Blocked-In';
newpath = '\2012-10-12 Data - GR23 461-663 Pump';
% newpath = '\2012-10-12 Data - GR9-625 Pump';
path(path,[pwd,newpath])

% % Liner_Order =
% linerum = 1; nul = 0.4995;% - GR9
% linerum = 2; nul = 0.45;% - GR9-625
% linerum = 3; nul = 0.4995;% - GR23
% linerum = 4; nul = 0.45;% - GR23-633
% linerum = 5; nul = 0.4995;% - HRP(12)
% linerum = 6; nul = 0.45;% - HRP(12)-545
linerum = 7; nul = 0.45;% - GR23 461-663
% linerum = 8; nul = 0.45;% - HRP(12) 461-493

n = 8;

if n < 10
    runname = strcat('run0',num2str(n));
else
    runname = strcat('run',num2str(n));
end
```

```

calset = 3;
% Calculate transmission loss of experimental data for comparison
[Freq_TL, TL_exp, temp(n,:), phadiff] = TL_func(runname,calset);
Freq = Freq_TL; % [Hz]
temp_cavity(n) = temp(n,2); % [C]
temp_pipe(n) = temp(n,1); % [C]
Pm = [300:100:1000 1500:500:3000]*6894.76; % [Pa]

[ELr,Eli] = interp(temp_cavity(n),n,linernum);
EL = ELr + li*Eli;

w = Freq*2*pi; % [rad/sec]
s = li*w; % [rad/sec]

% Port 1 is input from pipe
% Port 2 is output from tuner into junction
% Port 3 is base of annulus
% Port 4 is output of annulus at junction

% Transfer matrix [P4 Q4]' = [T34]*[P3 Q3]'

load Liner_Volume_Resonator.mat

% SHELL
Es = 210e9; % [Pa] Young's modulus of shell (steel)
nus = 0.3; % [ND] Poisson's ratio of shell (steel)
Ls = 104.14 /1000; %[m] Length of annulus
L = Liner_L(n+3,linernum+2) /1000; % [m] Length of annulus
rp = 10.30 /1000; % [m] Inner radius of connecting pipe
Sp = pi*rp^2; % [m^2] Area of pipe
r1 = 9.33 /1000; % [m] Inner radius of annulus
r2 = 10.62 /1000; % [m] Outer radius of annulus
r3 = Liner_r3(n+3,linernum+2)/1000; % [m] Inner radius of liner
r4 = Liner_r4(n+3,linernum+2)/1000; % [m] Outer radius of liner
r50 = 31.75 /1000; % [m] Inner radius of shell
r60 = 44.45 /1000; % [m] Outer radius of shell

% Calculate r5 and r6 at elevated pressure
r5 = r50 + (Pm(n)*r50/Es)*((r60^2 + r50^2)/(r60^2 - r50^2) + nus);
r6 = r60 + (2*Pm(n)*r50^2*r60)/(Es*(r60^2 - r50^2));

Vs = Ls*pi*(r5^2 - r2^2); % [m^3] Volume inside shell

% LINER
% E1 = B10(1) + li*B10(2); % [Pa] Given bulk modulus estimate
Vl = Liner_Volume(n+3,linernum+2); % [m^3]
ml = Liner_Mass(linernum)/1000; % [kg] Mass of liner
if Vl == 0
    rhol = 0;
else
    rhol = ml/Vl; % [kg/m^3] Density of liner
end

% FLUID

```

```

% Total volume of fluid
Vf = Vs - Vl;

% AIR
% ma = 1e-7; % kg
K = 1.4; % Specific heat ratio for air
% Ko = T_liner(n) + 273.15; % Temperature of air in Kelvin
% R = 287.04; % [J/kg*K] Specific gas constant for dry air
% Va = ma*R*Ko/Pm(n); % [m^3] Volume of air
% Ba = K*Pm(n); % [Pa] Bulk modulus of air
X0 = 0;
P0 = 0.1e6; % [Pa] Atmospheric pressure
rhoa0 = 1.2; % [kg/m^3] Density of air at standard conditions
Va0 = Vf*X0; % [m^3] Volume of air at standard conditions
Va = Va0*(Pm(n)/P0)^(-1/K); % [m^3] Volume of air at pressure/temp
if Va ~=0
    rhoa = rhoa0*Va0/Va; % [kg/m^3] Density of air
elseif Va == 0
    rhoa = 0;
end

ma = rhoa*Va;

% OIL IN WAVEGUIDE
visc_cavity = 178.4176*exp(-0.0344*temp_cavity(n)); % [cSt]
visc_cavity_si = visc_cavity*10^-6; % [Pa-s]

B0t_w = 10^(0.3766*(log10(visc_cavity))^0.3307 - 0.2766); % [GPa]
At_w = -0.01382*temp_cavity(n) + 5.851; % [GPa/GPa]
Bpt_w = (B0t_w + At_w*(Pm(n)/1e9))*1e9; % [Pa]

Bf_w = (1 - X0 + X0.*(P0/Pm(n)).^(1/K))./...
    ((X0/(K*Pm(n)))*(P0/Pm(n)).^(1/K) + (1 - X0)/Bpt_w);

% OIL IN PIPE
visc_pipe = 178.4176*exp(-0.0344*temp_pipe(n)); % [cSt]
visc_pipe_si = visc_pipe*10^-6; % [Pa-s]
B0t_p = 10^(0.3766*(log10(visc_cavity))^0.3307 - 0.2766); % [GPa]
At_p = -0.01382*temp_cavity(n) + 5.851; % [GPa/GPa]
Bpt_p = (B0t_p + At_p*(Pm(n)/1e9))*1e9; % [Pa]

Bf_p = (1 - X0 + X0.*(P0/Pm(n)).^(1/K))./...
    ((X0/(K*Pm(n)))*(P0/Pm(n)).^(1/K) + (1 - X0)/Bpt_p);

rhoo = 915; % [kg/m^3] Density of hydraulic fluid

% Stiffness of outer flow path of annular cylinder in a rigid shell
Bc = inv((2*r4^2*(1-nul))/(EL(n)*(r5^2-r4^2)));

% Calculate the effective bulk modulus of the fluid in the waveguide
Be = inv(1/Bf_w + 1/Bc);

c1 = sqrt(Bf_p/rhoo); % [m/s] Speed of sound within annulus
cu = c1; cd = c1; % [m/s] Speed of sound in connecting pipes

```

```

c2 = sqrt(Be/rhoo); % [m/s] Speed of sound in waveguide

% Loss factor for acoustic propagation in pipe
arg = li*r1*sqrt(s/visc_pipe_si);
alpha = (1 - 2*besselj(1,arg)./(arg.*besselj(0,arg))).^(-0.5); % [ND]
% alpha = 1 + sqrt(visc_pipe_si ./ (s*r1^2)) + visc_pipe_si ./(s*r1^2);

% Loss factor for acoustic propagation in waveguide
x = sqrt(s*r5^2/visc_cavity_si);
m = r4/r5; % [ND]

% Method of Washio and Konishi for attenuation in annular pipe
G = 1 + 1./((1-m)*x) + 3./(2*(1-m)^2*x.^2) - ...
    (1-22*m+m^2)./(8*m*(1-m)^3*x.^3);

gamma1 = s.*alpha/c1; % [1/m] Wavenumber in pipe
gamma2 = s.*G/c2; % [1/m] Wavenumber in oil (annulus)

Zc1 = rhoo*c1*alpha; % [] Specific impedance of oil in pipe
Zc2 = rhoo*c2*G; % [] Specific impedance of oil in annulus

Z0u(:,1) = (rhoo*cu*alpha)/(pi*rp^2); % [] Specific impedance of pipe
Z0d(:,1) = (rhoo*cd*alpha)/(pi*rp^2); % [] Specific impedance of pipe

T12_11(1,1,:) = cosh(gamma1*L);
T12_12(1,1,:) = Zc1.*sinh(gamma1*L)/(pi*r1^2);
T12_21(1,1,:) = pi*r1^2*sinh(gamma1*L)./Zc1;
T12_22(1,1,:) = cosh(gamma1*L);

T12 = [T12_11 T12_12; T12_21 T12_22];

T34_11(1,1,1:length(w)) = 1;
T34_12(1,1,1:length(w)) = 0;
T34_21(1,1,:) = pi*(r5^2-r4^2)*tanh(gamma2*L)./Zc2;
T34_22(1,1,1:length(w)) = 1;

T34 = [T34_11 T34_12; T34_21 T34_22];

% Preallocate matrix
T15 = zeros(2,2,length(Freq));

for p = 1:length(w)
    T15(:, :, p) = T34(:, :, p) * T12(:, :, p);
end

t1 = sqrt(Z0d./Z0u).*squeeze(T15(1,1,:));
t2 = squeeze(T15(1,2,:))./sqrt(Z0u.*Z0d);
t3 = sqrt(Z0u.*Z0d).*squeeze(T15(2,1,:));
t4 = sqrt(Z0u./Z0d).*squeeze(T15(2,2,:));

% System-independent TL
TL_model(:,1) = 20*log10((1/2)*abs(t1 + t2 + t3 + t4));

```

```

% plot(f,TL_model,'-')
% xlabel('Frequency [Hz]')
% ylabel('Transmission Loss [dB]')
% legend('Model')
% titlestring = strcat('Liner outer radius ',num2str(r4*1000),' mm');
% title(titlestring)
% xlim([0 5000])
% hold on

figure
subplot(2,2,1)
plot(Freq,real(t1),Freq,imag(t1))
subplot(2,2,2)
plot(Freq,real(t2),Freq,imag(t2))
subplot(2,2,3)
plot(Freq,real(t3),Freq,imag(t3))
subplot(2,2,4)
plot(Freq,real(t4),Freq,imag(t4))

figure
subplot(2,1,1)
plot(Freq,TL_model,'-',Freq_TL,TL_exp,'.')
xlabel('Frequency [Hz]')
ylabel('Transmission Loss [dB]')
legend('Model','Experiment')

subplot(2,1,2)
plot(Freq,phadiff)
xlabel('Frequency [Hz]')
ylabel('Phase condition')

rmpath([pwd,newpath])

```

### B.5.2 Modulus Interpolation

The output of the material property investigation is stored in a 4-D matrix named “Liner\_Properties.” This script interpolates between values in this matrix.

```

function [ELr, ELi] = interp(temp_cavity,n,linernum)

load Liner_Properties

ELr1 = E_L(n,1,linernum,1);
ELr2 = E_L(n,1,linernum,2);

ELi1 = E_L(n,2,linernum,1);
ELi2 = E_L(n,2,linernum,2);

TLc1 = T_L(n,2,linernum,1);
TLc2 = T_L(n,2,linernum,2);

ELr = ELr1 + (ELr2-ELr1)*(temp_cavity - TLc1)/(TLc2 - TLc1);

```

```
ELi = ELi1 + (ELi2-ELi1)*(temp_cavity - TLc1)/(TLc2 - TLc1);

end
```

## B.6 Herschel-Quincke Tube

For the Herschel-Quincke tube, its performance was studied theoretically – the code used to model the device is given in the section following.

### B.6.1 Modeling Code

```
% Model the Herschel-Quincke tube per the method in Hastings and Chen
% including a function to determine the waveguide compliance due to the
% presence of a compliant, lossy liner.
%%%%%%%%%%%%%%%%%%%%%%%%%%%%%%%%%%%%%%%%%%%%%%%%%%%%%%%%%%%%%%%%%%%%%%%%

% function [TL_model] = hq_function(vars,w)
%
% global n Pm T_oil nul

clear all
close all
clc

% % Liner_Order =
% linerum = 1; nul = 0.4995;% - GR9
% linerum = 2; nul = 0.45;% - GR9-625
% linerum = 3; nul = 0.4995;% - GR23
% linerum = 4; nul = 0.45;% - GR23-633
% linerum = 5; nul = 0.4995;% - HRP(12)
% linerum = 6; nul = 0.45;% - HRP(12)-545
linerum = 7; nul = 0.45;% - GR23 461-663
% linerum = 8; nul = 0.45;% - HRP(12) 461-493

n = 1;
t = 1;

temp_cavity = 25; % [C]
temp_pipe = 45; % [C]

load Liner_Volume_Resonator
load Liner_Properties

El = E_L(:,1,linerum,t) + 0.4*li*E_L(:,1,linerum,t);
Bl = El/(3*(1-2*nul));

Pm = [300:100:1000 1500:500:3000]*6894.76; % [Pa]

Ns = 5120; % Number of samples
Fs = 10800; % [Hz] Sampling rate
f = (Fs/Ns):(Fs/Ns):(Fs/2);
```

```

w = f*2*pi;
s = li*w;

% Port 1 is input from pipe
% Port 2 is output from tuner into junction
% Port 3 is base of annulus
% Port 4 is output of annulus at junction

% SHELL
Es = 210e9; % [Pa] Young's modulus of shell (steel)
nus = 0.3; % [ND] Poisson's ratio of shell (steel)
Ls = 104.1 /1000; % [m] Internal length of shell
L = Liner_L(n+3,linernum+2)/1000; % [m] Length of pipe/annulus
rp = 10.30 /1000; % [m] Inner radius of connecting pipe
r1 = 9.33 /1000; % [m] Inner radius of annulus
r2 = 10.60 /1000; % [m] Outer radius of annulus
r3 = Liner_r3(n+3,linernum+2)/1000; % [m] Inner radius of liner
r4 = Liner_r4(n+3,linernum+2)/1000; % [m] Outer radius of liner
r50 = 31.75 /1000; % [m] Inner radius of shell
r60 = 44.45 /1000; % [m] Outer radius of shell

% Calculate r5 and r6 at elevated pressure
r5 = r50 + (Pm(n)*r50/Es)*((r60^2 + r50^2)/(r60^2 - r50^2) + nus);
r6 = r60 + (2*Pm(n)*r50^2*r60)/(Es*(r60^2 - r50^2));

Vs = Ls*pi*(r5^2 - r2^2); % [m^3]

% LINER
Vl = Liner_Volume(n+3,linernum+2); % [m^3]
ml = Liner_Mass(linernum)/1000; % [kg] Mass of liner
if Vl == 0
    rho1 = 0;
else
    rho1 = ml/Vl; % [kg/m^3] Density of liner
end

% FLUID
% Total volume of fluid
Vf = Vs - Vl;

% AIR
% ma = 1e-7; % kg
K = 1.4; % Specific heat ratio for air
% Ko = T_liner(n) + 273.15; % Temperature of air in Kelvin
% R = 287.04; % [J/kg*K] Specific gas constant for dry air
% Va = ma*R*Ko/Pm(n); % [m^3] Volume of air
% Ba = K*Pm(n); % [Pa] Bulk modulus of air
X0 = 0;
P0 = 0.1e6; % [Pa] Atmospheric pressure
rhoa0 = 1.2; % [kg/m^3] Density of air at standard conditions
Va0 = Vf*X0; % [m^3] Volume of air at standard conditions
Va = Va0*(Pm(n)/P0)^(-1/K); % [m^3] Volume of air at pressure/temp
if Va ~=0
    rhoa = rhoa0*Va0/Va; % [kg/m^3] Density of air
elseif Va == 0

```

```

    rhoa = 0;
end

ma = rhoa*Va;

% OIL IN WAVEGUIDE
visc_cavity = 178.4176*exp(-0.0344*temp_cavity); % [cSt]
visc_cavity_si = visc_cavity*10^-6; % [Pa-s]

B0t_w = 10^(0.3766*(log10(visc_cavity))^(0.3307) - 0.2766); % [GPa]
At_w = -0.01382*temp_cavity + 5.851; % [GPa/GPa]
Bpt_w = (B0t_w + At_w*(Pm(n)/1e9))*1e9; % [Pa]

Bf_w = (1 - X0 + X0.*(P0/Pm(n)).^(1/K))./...
        ((X0/(K*Pm(n)))*(P0/Pm(n))^(1/K) + (1 - X0)/Bpt_w);

% OIL IN PIPE
visc_pipe = 178.4176*exp(-0.0344*temp_pipe); % [cSt]
visc_pipe_si = visc_pipe*10^-6; % [Pa-s]
B0t_p = 10^(0.3766*(log10(visc_cavity))^(0.3307) - 0.2766); % [GPa]
At_p = -0.01382*temp_cavity + 5.851; % [GPa/GPa]
Bpt_p = (B0t_p + At_p*(Pm(n)/1e9))*1e9; % [Pa]

Bf_p = (1 - X0 + X0.*(P0/Pm(n)).^(1/K))./...
        ((X0/(K*Pm(n)))*(P0/Pm(n))^(1/K) + (1 - X0)/Bpt_p);

rhoo = 915; % [kg/m^3] Density of hydraulic fluid

% Stiffness of outer flow path of annular cylinder in a rigid shell
Bc = inv(2*r4^2*(1-nul)./(E1(n)*(r5^2-r4^2)));

% Calculate the effective bulk modulus of the fluid in the waveguide
Be = inv(1/Bf_w + 1/Bc);

c1 = sqrt(Bf_p/rhoo); % [m/s] Speed of sound within annulus
cu = c1; cd = c1; % [m/s] Speed of sound in connecting pipes
c2 = sqrt(Be/rhoo); % [m/s] Speed of sound in waveguide

% Loss factor for acoustic propagation in pipe
arg = li*r1*sqrt(s/visc_pipe_si);
alpha = (1 - 2*besselj(1,arg)./(arg.*besselj(0,arg))).^(-0.5);

% Loss factor for acoustic propagation in waveguide
x = sqrt(r5^2*s/visc_cavity_si);
m = r4/r5;

% Method of Washio and Konishi for attenuation in annular pipe
G = 1 + 1./((1-m)*x) + 3./(2*(1-m)^2*x.^2) - ...
    (1-22*m+m^2)./(8*m*(1-m)^3*x.^3);

gamma1 = s.*alpha/c1; % [1/m] Wavenumber in pipe
gamma2 = s.*G/c2; % [1/m] Wavenumber in oil (annulus)

```

```

Zc1 = rhoo*c1*alpha; % [Pa-s/m^3] Impedance of oil in pipe
Zc2 = rhoo*c2*G; % [Pa-s/m^3] Impedance of oil in annulus

Z0u(:,1) = (rhoo*cu*alpha)/(pi*rp^2); % [Pa-s/m^3] Impedance of pipe
Z0d(:,1) = (rhoo*cd*alpha)/(pi*rp^2); % [Pa-s/m^3] Impedance of pipe

a11 = cosh(gamma1*L);
a12 = -Zc1.*sinh(gamma1*L)/(pi*r1^2);
a21 = -pi*r1^2*sinh(gamma1*L)./Zc1;
a22 = a11;

b11 = cosh(gamma2*L);
b12 = -Zc2.*sinh(gamma2*L)/(pi*(r5^2-r4^2));
b21 = -pi*(r5^2-r4^2)*sinh(gamma2*L)./Zc2;
b22 = b11;

% Exactly from Hastings & Chen
T16_11 = a11.*b12 + a12.*b11;
T16_12 = a12.*b12;
T16_21 = (a21 + b21).*(a12 + b12) + (b22 - a22).*(a11 - b11);
T16_22 = a22.*b12 + a12.*b22;
Pre = 1./(a12+b12);

% Preallocate matrix
T16 = zeros(2,2,length(f));

for p = 1:length(f)
    T16(:, :, p) = inv(Pre(p).*[T16_11(p) T16_12(p); T16_21(p)
T16_22(p)]);
end

t1 = sqrt(Z0d./Z0u).*squeeze(T16(1,1,:));
t2 = squeeze(T16(1,2,:))./sqrt(Z0u.*Z0d);
t3 = sqrt(Z0u.*Z0d).*squeeze(T16(2,1,:));
t4 = sqrt(Z0u./Z0d).*squeeze(T16(2,2,:));

TL_model(:,1) = 20*log10((1/2)*abs(t1 + t2 + t3 + t4));

plot(f,TL_model,'-')
xlabel('Frequency [Hz]')
ylabel('Transmission Loss [dB]')
grid on

% plot(f,TL_model,'-',f_exp,TL_exp,'o')
% xlabel('Frequency [Hz]')
% ylabel('Transmission Loss [dB]')
% legend('Model','Experiment')
% titlestring = strcat('Liner inner radius ',num2str(r2*1000),' mm');
% title(titlestring)

```

## REFERENCES

- [1] N.E. Earnhart, K.A. Marek, and K.A. Cunefare, *Evaluation of hydraulic silencers*, in *NoiseCON 2010*. 2010: Baltimore, MD.
- [2] D.N. Johnston, D.K. Longmore, and J.E. Drew, *A technique for the measurement of the transfer matrix characteristics of two-port hydraulic components*. Fluid Power Systems and Technology, 1994. **1**: p. 25-33.
- [3] K.K. Lau, D.N. Johnston, and K.A. Edge. *Fluid borne noise characteristics of hydraulic filters and silencers* in *Innovations in Fluid Power, 7th Bath International Fluid Power Workshop*. 1994. University of Bath, UK: Research Studies Press Ltd.
- [4] H. Helmholtz, *Theory of Air Oscillations in Tubes with Open Ends*. Journal für die Reine und angewandte Mathematik, 1860. **57**: p. 1-72.
- [5] E. Kojima and K.A. Edge. *Experimental determination of hydraulic silencer transfer matrices and assessment of the method for use as a standard test procedure* in *Innovations in Fluid Power, 7th Bath International Fluid Power Workshop*. 1994: Research Studies Press Ltd.
- [6] K.K. Lau, D.N. Johnston, and K.A. Edge, *Fluid borne noise characteristics of hydraulic filters and silencers*, in *Innovations in Fluid Power: 7th Bath International Fluid Power Workshop*. 1994: Bath, U.K. p. 242-260.
- [7] E. Kojima and T. Ichiyangi, *Development research of new types of multiple volume resonators*, in *Bath Workshop on Power Transmission and Motion Control*, C.R. Burrows and K.A. Edge, Editors. 1998, Professional Engineering Publishing Ltd.: Bath, U.K. p. 193-206.
- [8] M. Ijas and T. Virvalo, *Experimental validation of pulsation dampers and their simplified theory*, in *Bath Workshop on Power Transmission and Motion Control*, C.R. Burrows and K.A. Edge, Editors. 2000, Professional Engineering Publishing, Ltd.: Bath, U.K. p. 227-240.
- [9] G.E.M. Vael, I. López, and P.A.J. Achten, *Reducing flow pulsation with the floating cup pump - theoretical analysis*, in *Power Transmission and Motion Control*, C.R. Burrows, D.N. Johnston, and K.A. Edge, Editors. 2004, Professional Engineering Publishing, Ltd.: Bath, U.K. p. 123-141.
- [10] N. Bügener, S. Helduser, and J. Weber. *Numerical analysis of a measure to improve the suction performance of hydrostatic pumps* in *6th FPNI-PhD Symposium*. 2010. West Lafayette, IN.
- [11] L. Kela, *Resonant frequency of an adjustable Helmholtz resonator in a hydraulic system*. Archives of Applied Mechanics, 2008. **79**: p. 11.
- [12] L. Kela, *Adaptive Helmholtz Resonator in a Hydraulic System*. World Academy of Science, Engineering and Technology, 2010. **68**: p. 1180-1187.
- [13] L. Kela and P. Vähöja, *Control of an Adjustable Helmholtz Resonator in a Low-Pressure Hydraulic System*. International Journal of Fluid Power, 2009. **10**(3): p. 10.

- [14] D.M. Photiadis, *The effect of wall elasticity on the properties of a Helmholtz resonator*. Journal of the Acoustical Society of America, 1991. **90**(2): p. 1188-1190.
- [15] R.S. Woollett, *Underwater Helmholtz Resonator Transducers: General Design Principle*. 1977, Naval Underwater Systems Center.
- [16] G.A. Brigham, *On the theory of stress-constrained optimum compliant tubes and uniform tube arrays*. Journal of the Acoustical Society of America, 1981. **69**(6): p. 1545-1556.
- [17] G.A. Brigham, *Erratum: "On the theory of stress-constrained optimum compliant tubes and uniform tube arrays"*. Journal of the Acoustical Society of America, 1982. **71**(3): p. 757-757.
- [18] T.A. Henriquez and A.M. Young, *The Helmholtz resonator as a high-power deep-submergence source for frequencies below 500 Hz*. Journal of the Acoustical Society of America, 1980. **67**(5): p. 1555-1558.
- [19] A. Selamet, et al., *Helmholtz resonator lined with absorbing material*. Journal of the Acoustical Society of America, 2005. **117**(2): p. 725-733.
- [20] A.D. Pierce, *Acoustics: An Introduction to Its Physical Properties and Applications*. 1989, Melville, NY: Acoustical Society of America.
- [21] G. Yu, L. Cheng, and D. Li, *A three-dimensional model for T-shaped acoustic resonators with sound absorption materials*. Journal of the Acoustical Society of America, 2011. **129**(5): p. 3000-3010.
- [22] F.E. Ehlers, *Method for Measuring Bulk Modulus of a Liquid Using a Helmholtz Resonator*. Journal of the Acoustical Society of America, 1960. **32**(5): p. 538-546.
- [23] E. Kojima and T. Ichiyanagi, *Research on pulsation attenuation characteristics of silencers in practical fluid power systems*. International Journal of Fluid Power, 2000. **1**(2): p. 29-38.
- [24] G.T. Klees. *Attenuating Device*. USPTO Pat. No. 3,323,305 (1967).
- [25] R. Strunk. *Silencer for Hydraulic Piston Pump Pressure Pulsations in International Off-Highway & Powerplant Congress & Exposition, September 1991*. 1991. Milwaukee, WI.
- [26] M.C. Hastings and C.-C. Chen. *Analysis of Tuning Cables for Reduction of Fluidborne Noise in Automotive Power Steering Hydraulic Lines in Proceedings of the 1993 Noise and Vibration Conference*. 1993: SAE International.
- [27] J.E. Drew, D.K. Longmore, and D.N. Johnston, *Theoretical analysis of pressure and flow ripple in flexible hoses containing tuners*. Proceedings of the Institution of Mechanical Engineers, 1998. **212**(1): p. 405-422.
- [28] J.M. Dodson, D.R. Dowling, and K. Grosh, *Experimental investigation of quarter wavelength silencers in large-scale hydraulic systems*. Noise Control Engineering Journal, 1998. **46**(1): p. 15-22.
- [29] M.L. Munjal and P.T. Thawani, *Acoustic analysis and design of compliant cable-hose systems*. Noise Control Engineering Journal, 1997. **45**(6): p. 235-242.
- [30] A. Knapp. *Device for dampening vibration and noise in hydraulic installations*. USPTO Pat. No. (1997).
- [31] J.F.W. Herschel, *On the absorption of Light by Coloured Media, viewed in connexion with the Undulatory Theory*, in *Philosophical Magazine and Journal of Science*. 1833. p. 401-412.

- [32] G.W. Stewart, *The theory of the Herschel-Quincke tube*. Physical Review, 1928. **31**: p. 696-698.
- [33] A. Selamet, N.S. Dickey, and J.M. Novak, *The Herschel-Quincke tube: A theoretical, computational, and experimental investigation*. Journal of the Acoustical Society of America, 1994. **96**(5): p. 3177-3185.
- [34] A. Selamet and V. Easwaran, *Modified Herschel-Quincke tube: Attenuation and resonance for n-duct configuration*. Journal of the Acoustical Society of America, 1997. **102**(1): p. 164-169.
- [35] B. Poirier, et al., *Bicylindrical model of Herschel-Quincke tube-duct system: Theory and comparison with experiment and finite element method*. Journal of the Acoustical Society of America, 2009. **126**(3): p. 1151-1162.
- [36] C.-C. Chen and M.C. Hastings. *Half-wavelength tuning cables for passive noise control in automotive power steering systems in International Mechanical Engineering Congress and Exposition*. 1994. Chicago, IL: ASME Design Engineering Division.
- [37] G.T. Klees. *Attenuating Device*. Pat. No. 3,323,305 (1967).
- [38] J.A. Burton. *Pulsation Dampener*. USPTO Pat. No. 4,299,253 (1981).
- [39] M. Giordano. *Muffler for Internal Combustion Engines*. USPTO Pat. No. 3,174,583 (1965).
- [40] K.U. Ingard and W.P. Patrick. *Lined-Duct Acoustic Filter*. USPTO Pat. No. 4,346,781 (1982).
- [41] M.L. Munjal and P.T. Thawani, *Acoustic performance of hoses—A parametric study*. Noise Control Engineering Journal, 1996. **44**(6): p. 274-280.
- [42] T. Sajo, *Antireflective materials at ultrasound frequencies*. Journal of the Acoustical Society of America, 1986. **79**(1): p. 18-25.
- [43] V.F. Humphrey, et al., *Acoustic characterization of panel materials under simulated ocean conditions using a parametric array source*. Journal of the Acoustical Society of America, 2008. **124**(2): p. 803-814.
- [44] R.D. Corsaro, J.D. Klunder, and J. Jarzynski, *Filled rubber materials system: application to echo absorption in waterfilled tanks*. Journal of the Acoustical Society of America, 1980. **68**(2): p. 655-664.
- [45] R.D. Corsaro and J.D. Klunder, *A Filled Silicone Rubber Materials System with Selectable Acoustic Properties for Molding and Coating Applications at Ultrasonic Frequencies*. 1979, Naval Research Laboratory.
- [46] D.H. Trivett, H. Pincon, and P.H. Rogers, *Investigation of a three-phase medium with a negative parameter of nonlinearity*. Journal of the Acoustical Society of America, 2006. **199**(6).
- [47] A. Blanchet and G. Chatel. *Prediction Method of Pump Noise Transmitted by Piping Fixation Devices in Inter-Noise 95*. 1995. Newport Beach, CA, USA.
- [48] W.C. Young and R.G. Budynas, *Roark's Formulas for Stress and Strain*. 7th ed. 2002: McGraw-Hill.
- [49] AkzoNobel, *Compression of Expancel DE mpg*.
- [50] G.W. Jones, *Static Elastic Properties of Composite Materials Containing Microspheres*, in *Jesus College*. 2007, University of Oxford.
- [51] J.H. Wheeler and J.P. Frenzoz. *Fluid Noise Muffler and Method of Manufacture*. USPTO Pat. No. 5,426,270 (1995).

- [52] J. DiRe. *Hydraulic pump with foamed elastomeric member in outlet chamber to reduce liquid-borne noise*. USPTO Pat. No. 5,180,298 (1993).
- [53] R.C. Hansen. *Fluidborne Noise Attenuator*. USPTO Pat. No. 4314621 (1982).
- [54] S. Timoshenko, *Strength of Materials Part II: Advanced Theory and Problems*. 2nd ed. 1940: D. Van Nostrand Company, Inc.
- [55] N.D. Manring, *Hydraulic Control Systems*. 2005: Wiley. 464.
- [56] D.J. Korteweg, *On the velocity of propagating sound in elastic tubes*. *Annalen der Physik*, 1878. **174**: p. 525-542.
- [57] H. Lamb, *Velocity of sound in a tube, as affected by the elasticity of the walls*. *Memoirs and Proceedings - Manchester Literary and Philosophical Society*, 1898. **42**: p. 1-16.
- [58] L.G. Pooler, *The Velocity of Propagation of Longitudinal Waves in Liquids at Audio-Frequencies*. *Physical Review*, 1930. **35**(7): p. 832-847.
- [59] M.C. Junger and D. Feit, *Sound, Structures, and Their Interaction*. 1993: Acoustical Society of America.
- [60] J. Yu and E. Kojima, *Wave propagation in fluids contained in finite-length anisotropic viscoelastic pipes*. *Journal of the Acoustical Society of America*, 1998. **104**(5): p. 3227-3235.
- [61] H.S. Song, E.E. Klaus, and J.L. Duda, *Prediction of bulk moduli for mineral oil based lubricants, polymer solutions, and several classes of synthetic fluids*. *Journal of Tribology*, 1991. **113**: p. 675-680.
- [62] R. Haas, A. Tairysh, and B. Manhartgruber. *Adiabatic and isothermal fluid bulk modulus – common theories and model verification in 7th FPNI PhD Symposium on Fluid Power*. 2012. Reggio Emilia, Italy.
- [63] H. Gholizadeh, R. Burton, and G. Schoenau, *Fluid bulk modulus: comparison of low pressure models*. *International Journal of Fluid Power*, 2012. **13**(1): p. 7-16.
- [64] M.J.R. Bardeleben and D.S. Weaver. *Estimation of the acoustic scattering matrix for a centrifugal pump in ASME international mechanical engineering congress and exposition*. 2002. New Orleans, LA, USA: ASME AMD.
- [65] H. Gholizadeh, et al. *Experimental investigation of measuring fluid bulk modulus in low pressure regions in 7th FPNI PhD Symposium on Fluid Power*. 2012. Reggio Emilia, Italy.
- [66] AkzoNobel. 2003. p. 2-3.
- [67] B.H. Song and J.S. Bolton, *A transfer-matrix approach for estimating the characteristic impedance and wave numbers of limp and rigid porous materials*. *Journal of the Acoustical Society of America*, 2000. **107**(3): p. 1131-1152.
- [68] A. Stirnemann, et al., *Experimental Determination of the Dynamic Transfer Matrix for a Pump*. *Journal of Fluids Engineering*, 1987. **109**: p. 218-225.
- [69] W.T. Chu, *Impedance Tube Measurements - A Comparative Study of Current Practices*. *Noise Control Engineering Journal*, 1991. **37**(1): p. 37-44.
- [70] T. Fujimori, S. Sato, and H. Miura, *Automated measurement system of complex sound pressure reflection coefficients*, in *Inter-Noise*. 1984: Honolulu, Hawaii. p. 1009-1014.
- [71] S.-H. Jang and J.-G. Ih, *On the multiple microphone method for measuring in-duct acoustic properties in the presence of mean flow*. *Journal of the Acoustical Society of America*, 1997. **103**(3): p. 1520-1526.

- [72] ISO-15086-1, *Hydraulic fluid power - Determination of fluid-borne noise characteristics of components and systems*, in *Introduction*. 2001, International Standards Organization: Geneva, Switzerland.
- [73] ISO-15086-2, *Hydraulic fluid power - Determination of fluid-borne noise characteristics of components and systems*, in *Measurement of speed of sound in a fluid in a pipe*. 2000, International Standards Organization: Geneva, Switzerland.
- [74] ISO-15086-3, *Hydraulic fluid power - Determination of the fluid-borne noise characteristics of components and systems*, in *Measurement of hydraulic impedance*. 2008, International Standards Organization: Geneva, Switzerland.
- [75] R.L. Panton and J.M. Miller, *Resonant frequencies of cylindrical Helmholtz resonators*. Journal of the Acoustical Society of America, 1975. **57**: p. 1533-1535.
- [76] L.E. Kinsler, et al., *Fundamentals of Acoustics*. 4th ed. 1999: John Wiley & Sons, Inc.
- [77] J.A. Sauer, *Deformation, Yield, and Fracture of Polymers at High Pressure*. Polymer Engineering & Science, 1977. **17**(3): p. 150-164.
- [78] A.F. D'Souza and R. Oldenburger, *Dynamic Response of Fluid Lines*. Journal of Basic Engineering, 1964. **86**: p. 589-598.
- [79] S. Washio and T. Konishi, *Research on Wave Phenomena in Hydraulic Lines (11th Report, Harmonic Waves in Coaxial Double Pipes)*. Bulletin of JSME, 1985. **28**(241): p. 1409-1415.
- [80] T.M. Way, *The use of hoses and hose inserts to reduce pressure ripple in hydraulic circuits*. 2004, University of Bath.

## **VITA**

### **NICHOLAS E. EARNHART**

EARNHART was born in Hilton, New York. He graduated from Hilton High School in 2002, and received a B.S. in Mechanical Engineering from Purdue University, West Lafayette, Indiana in 2007. Mr. Earnhart completed the Co-Op Program at Purdue University, working five semesters at GE Motors & Controls in Fort Wayne, Indiana. After completing his B.S., he interned at Rolls Royce North America in Indianapolis, Indiana, before enrolling as a Ph.D. student at the Georgia Institute of Technology. He earned his M.S. in Mechanical Engineering from the Georgia Institute of Technology, Atlanta, Georgia in 2009. Outside of his work, he enjoys playing basketball and spending time with his wife, Maria and their terrier, Henry.